MOVPE Growth of AlN and AlGaN/AlN Quantum Wells and their Optical Polarization Properties

Ryan Ganipan Banal

MARCH 2009

Contents

Abstract

The study of nitride semiconductor materials (AlN, GaN and InN) has gained research momentum after breakthroughs in light-emitting diodes (LEDs) and laser diodes (LDs) based on III-V nitrides. As a result, this technology will play an increasingly important role in the lighting technology and will become the dominant light sources in the future, positioning itself to replace fluorescent lamps and incandescent bulbs. The characteristics of nitride materials that are lacking in conventional light sources are being compact, has long-lifetime, high-luminescence efficiency, and quick response time. The research in nitride semiconductors have always been focused on the visible region or using GaN and InN. The research became even more attractive especially when several growth-related issues have been addressed. Since then, the growth technology has advanced and high-efficiency LEDs and LDs in the visible region has become available.

Unlike GaN and InN in the visible region, research on AlN into the ultraviolet (UV) region came in much later. The strong interest in the study of this material was fueled by its several important applications. UV emitters are considered as the next-generation data storage, which have the capability to store more data (high-density) than that emitting in the blue region. It is also aimed for water purification where biological organisms have never developed a tolerance at wavelengths below 290 nm (UVC), as well as for air disinfection. When realized, the purification of water will have an enormous impact especially in areas where there is a scarcity of clean water supply. UV emitters also do not require any complicated attachments thus it can be used with ease and simplicity. For medical application, UV emitters also have the potential to treat skin diseases. UV emitters based on LEDs and LDs are rugged and safe, in contrast to the existing UV sources (mercury, xenon, and deuterium lamps) where larger operating voltage is required and the danger it poses to the environment.

The applications of UV emitters are indeed enormous. But just like the case of InGaN during its early development stage, realizing the full potential

of AlGaN to tune the emission wavelength is also hindered by the inferior quality of the epilayer. So far, the recorded highest external quantum efficiency has only achieved a dismal 0.2% - much lower than that recorded in blue LED, which was about 75%. Therefore the improvement of its quality is of utmost importance and intensive research effort is necessary if it is to catch up with InGaN. Just as its potential applications are waiting to be realized, enormous efforts are also needed to achieve the pervasive high-quality AlN.

Among the interesting properties of AlN is related to optical polarization properties, where the crystal-field split energy is negative compared to the positive value in GaN. Because of this, the emission polarization is different between these materials. This optical polarization property in AlN has not been studied fully. More interestingly, the combination of AlN and GaN is expected to have a component of AlN-like and GaN-like properties. Thus, delineation between these two properties must be understood well.

Obtaining high-efficiency AlGaN-based UV-emitters is perceived difficult to achieve. Though the first step, which is by improving the AlN has shown some remarkable progress in the past, moving on to the fabrication of the active layer has proven even more difficult. Aside from the knowledge of the fundamental optical properties of AlN and GaN, the optical properties of the Al-rich ternary AlGaN alloy formed from these binary alloys are still unexplored. With the aim of 100% emission efficiency, the fundamental properties of these materials must be understood well. Finding for an appropriate method in fabricating both AlN and AlGaN/AlN quantum wells (QWs) is hoped to pave the way for a better understanding of the structural and the optical properties of AlN and AlGaN/AlN QWs structure.

Finding the solution for these issues might not be too big a task. Some hints or even answers can be found from GaN. Taking on the challenge, in this thesis, one of the main purposes of this study is to fabricate AlGaN/AlN QWs emitting at deep-UV (DUV) spectral region ($\lambda < 290$ nm). To achieve this, a new method based on MOVPE is introduced and called modified MEE - hybridized from MEE and the conventional simultaneous source-supply method, such that the latter is inserted in-between the former. Then this method is adopted for the fabrication of AlGaN/AlN QWs. The systematic study of the structural and optical properties both for AlN and AlGaN/AlN is performed.

Indeed, a systematic approach is needed to address the issue of low-quality AlN and AlGaN epilayers. Focusing on AlN, the new developed method is

used and characterized in terms of the initial nucleation stages where the propagation of dislocation starts, and the diffusion mechanism of Al adatom. Several structural characterizations were performed as well as photoluminescence (PL) studies for probing the optical properties. This is explained in Chapters 2 and 3.

After the growth of AlN epilayer, studies on the fabrication of AlGaN/AlN QWs were then performed. The issue of poor quality is addressed by utilizing modified MEE method, which was developed for AlN epilayer. Indeed the quality has been successfully enhanced as confirmed by the observation of intense PL emitted from the QW layers. This promising results could pave the way for the study of AlGaN/AlN QWs. Issues on AlGaN/AlN QWs fabrication and optimization is found in Chapter 4.

Towards its application in the DUV emission, the optical polarization characterization in AlGaN/AlN was performed. It showed that an intense surface emission can be achieved at wavelength as short as $\sim$220 nm, due to quantum confinement and strain effect. The mechanism of optical polarization anisotropy is explained in detail in Chapter 5. Thus, improvement on the quality of AlN and AlGaN/AlN epilayer is the pandora's box for the better understanding of their optical properties.

Chapter 1

Introduction

1.1 Research Background

1.1.1 III-V Nitrides

Since the invention of the incandescent bulb by Thomas Edison in 1879, there has been a continuous motivation to come up with less expensive, more reliable, and brighter lighting sources. Until today, widely-used light sources are still based on filament and fluorescent lamps for interior illumination, sodium-discharge lamps for street lighting, and neon signs for outdoor advertisements.

The most recent revolutionary lighting advancement was made possible thanks to the light-emitting diode (LED) based on III-V compound semiconductor materials, as shown in Figure 1.1. Initially demonstrated in 1962, the LED [1] and the laser diode (LD) [2, 3] were then used in such diverse applications as optical-fiber communication networks, instrument-panel indicators, CD optical-storage technology, laser printers, and automobile tail lights. Originally for red LEDs, other LEDs having yellow, orange, and amber colors with high-emission efficiencies superior to incandescent lamps became commercially available by the early 1990's [4]. Still with the goal of achieving 100% emission efficiency, research has never been more challenging as devices have started to be grown on unconventional surface planes to overcome the drawbacks (e.g., QCSE) observed in conventional c-planes. With the improvement on growth technologies, LEDs and LDs are expected to infiltrate the full-color outdoor display, traffic signal, and automotive interior and exterior lighting markets

However, while the technological growth of red and yellow LEDs were very rapid in the past decades, the push to extend the emission into the short

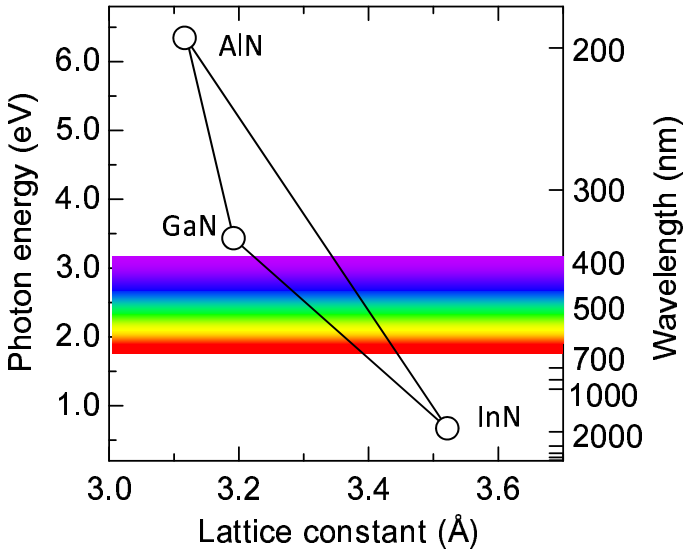

Figure 1.1: The lattice constants (a_0) of binary III-V semiconductors compounds plotted against their corresponding bandgap energy and wavelength at room temperature.

wavelength region of the visible spectrum (from green to ultraviolet) has proven very challenging. Although successful attempts to make LEDs and LDs with SiC and II-VI materials (e.g., ZnSe) have been made, the practical applications of such devices were diminished by its low efficiency and the short device lifetimes in the II-VI materials due to the relative ease of defect formation. This has opened the door to look for other materials. And true enough, it brought considerable interest for the III-V nitride materials with the wurtzite crystal structure (GaN, AlN, InN, and their alloys), as shown in Figure 1.1. Since the electronic band structure for each of the nitride materials possesses a direct transition with a band gap energy ranging from 0.7 eV [5] for InN, to 3.4 eV for GaN, to 6.1 eV for AlN at room temperature as well as a fairly high thermal conductivity, the (AlIn)GaN system has been explored in the areas of high-power and high-temperature electronic devices and short-wavelength (visible and ultraviolet) optoelectronic devices [6].

The effort to produce and characterize the nitrides materials began more than 30 years ago at several research facilities, such as AT&T Bell Laboratories, IBM Thomas J. Watson Research Center, and RCA. These research facilities were actively pursuing the research due to the potential for producing surface acoustic wave devices, blue lasers, and LEDs. However, most of these programs were eventually canceled due to the inability to solve several key technological problems that hampered the development. The problem

at that time was the unavailability of suitable bulk-crystal technology for producing GaN substrates. As the case today, epitaxy was done on highly lattice- and thermal-expansion-mismatched substrates such as silicon, gallium arsenide, and sapphire. Therefore the resulting heteroepitaxial films were highly-defected with 10^{10} dislocations/cm^2, and highly conducting as a result of defects and impurities [7]. The films also exhibited poor surface morphology because of the non-optimized growth parameters used.

It was not until the mid-1980's that these problems started to be overcome, due in large part to the efforts of Isamu Akasaki at Nagoya and Meijo Universities and a group led by Shuji Nakamura at Nichia Chemical Company. The use of thin, low-temperature AlN [8] and, later, GaN [9] buffer layers facilitated the growth of high-quality GaN films which were free of cracks on sapphire substrates by metalorganic capor phase epitaxy (MOVPE). Along with this, remarkable improvements in the electrical and optical properties were demonstrated. Another monumental breakthrough was the first successful production of p-type GaN by low-energy electron-beam irradiation (LEEBI) of magnesium-doped GaN, which in the as-grown state exhibits high resistivity [10], resulting in the first demonstration of GaN electroluminescent device based on a p-n junction. Subsequently, it was shown that magnesium-doped GaN could also be made conductive by thermal annealing in a N_2 ambient at a temperature of about 600 °C [11]. These developments, along with the fact that light-generation processes in the nitride material seem unaffected by the high dislocation density commonly found in the epitaxial films, have allowed the demonstration and commercialization of high-brightness blue and green double heterostructure [12] and single quantum well (SQW) [13] LEDs in the past few years as well as the demonstration of the first violet (∼420 nm) room-temperature, continuous-wave (CW) LD in 1996 [14].

1.1.2 Towards Ultraviolet Emitters and Applications

Since the first successful fabrication of high-efficiency light-emitters in the visible range and due to its matured technology, the research trend is now shifting towards lower emission wavelengths or into ultraviolet (UV) region (Figure 1.2). Apart from the conventional polar plane, research in the visible region using InGaN-based devices are the ones leading the fabrication using non-polar planes where its merit is the elimination of quantum-confined stark effect (QCSE) in QWs fabricated using conventional polar plane [15].

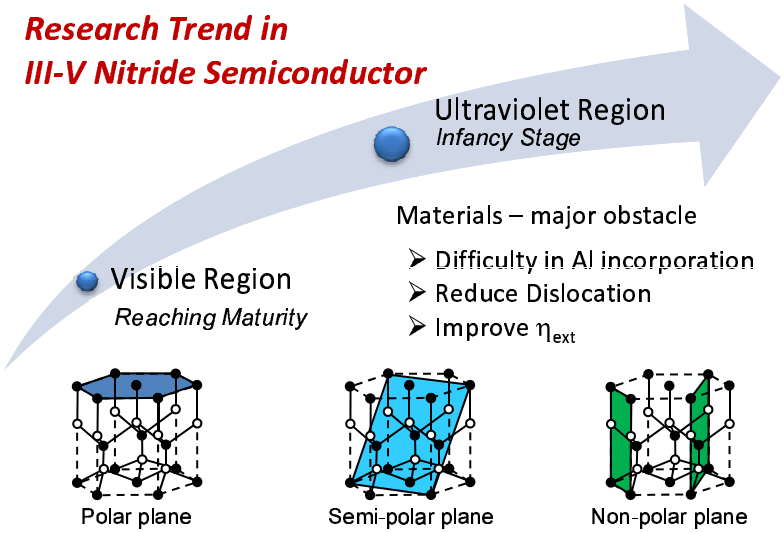

Figure 1.2: Current research trend in the study of III-V nitrides. While the visible region has improved by leaps and bounds in terms of epitaxy and efficiency, the ultraviolet region has just started attract interests. As shown, the foremost concern to obtain high-efficiency UV devices is to improve the material.

AlN is the most suitable material among the III-Nitride materials in realizing its applications in the ultraviolet region. In the UV region, the candidate active layer materials are AlN and GaN and their alloys. AlN is a choice template layer for AlGaN/AlN quantum well active layer structures because of its smaller in-plane lattice parameter a_0 relative to AlGaN, and because it is transparent to up to $\lambda > 200$ nm. However, moving into shorter wavelengths requires increasing Al incorporation into the matrix material. Due to the small lattice constant of AlN, it produces tensile stress leading to cracking in the AlGaN layer. Since it was only recently that Al(Ga)N was given attention to, there are interesting properties for this material awaiting to be uncovered.

The electromagnetic spectrum is divided into regions based on the wavelength of radiation. For UV region, it is defined as the wavelength range from 10 nm to 400 nm. The ultraviolet region is further sub-classified into four regions, as shown below. The existing UV emitters use mostly a mixture

Classification of Ultraviolet (UV)	Emission Wavelength (nm)
Vacuum UV	10-200
UV-C (Short wave)	200 - 290
UV-B (Medium wave)	290 - 320
UV-A (Long wave)	320 - 400

of gases to emit a monochromatic light (gas lasers), metal-vapor discharge (metal-vapor laser) as the gain medium, or gas-discharge as another light source. These include ArF excimer gas lasers (emission wavelength, $\lambda = 193$ nm), Hg vapor discharge lamps, D_2, Xe, KrCl, and XeCl lamps. However, gas mixtures and vapor discharge sources are harmful to the human health and the environment, aside from the low gas lifetime. Because of these undesirable components of conventional UV emitters, solid-state light-emitting diodes and laser diodes are the promising replacements because they are safe, compact, maintenance-free, and have long-lifetime with high-emission efficiency.

Though in its early stage, the research into UV emission range is fueled by their potential applications in air- and water-purifications, germicidal and biological instrumentation systems, and in future technology. Among them include: white light semiconductor emitter, which can be done by employing phosphors, high-density optical recording and DUV DVD. For areas where access to clean water is scarce, DUV can be used for treating the water at a large-scale without the need for a sophisticated or bulky accessories to set-up the DUV emitters. For medical use, light-sources in the DUV range are also being used to treat skin diseases.

1.2 Challenges and Current Status of AlN

1.2.1 History of AlN

Table 1.1 enumerates the important achievements in the study of AlN with the exception of the milestone achievement led by Dr. Nakamura at Nichia Chemicals in their study of blue LEDs [18], and the Migration Enhanced Epitaxy of GaAs [16] which paved the way for alternating supply of precursors in growth. Most of these achievements are related to improving the quality of the epilayer where some groups have introduced auxiliary steps to improve its quality. For example, a two-step approach - by initially growing a low-temperature buffer layer and then growing the epilayer at a higher temperature was able to significantly improve the quality of the epilayer [8]. Then other methods were also developed and were based on the alternating supply of precursors [17, 19, 20, 24], which was first employed for GaAs [16]. Continuous improvements in AlN are still going on. In fact growth at much higher temperature has already been explored [23]. On the other hand, a remarkable feat was achieved when an AlN p-i-n junction LED was demon-

strated to emit at 210 nm [21].

Table 1.1: Significant Achievements in AlN Research

Year	Key Achievements	Group
1986	Low-temperature AlN buffer layer	[8]
1986	GaAs/AlGaAs Migration Enhanced Epitaxy	[16]
1993	Pulsed Atomic-layer epitaxy for AlN and AlGaN	[17]
1993	High-Brightness InGaN/AlGaN DH Blue LED	[18]
1999	AlN and AlGaN QWs Alternate Source-Feeding Epitaxy	[19]
2003	Flow-Rate Modulation Epitaxy of AlN and AlGaN	[20]
2006	210 nm AlN LED (η_{ext}=10^{-6} %)	[21]
2006	RT Stimulated Emission at 214 nm	[22]
2006	High-Temperature Growth (>1300 °C)	[23]
2008	227 nm AlGaN LED by Multi-buffer layer (η_{ext}=0.2 %)	[24]

1.2.2 Current Status of AlN

The absence of defect-free bulk substrates has led to the growth of AlN on foreign substrates such as sapphire and SiC [25–27]. It is well known that this heteroepitaxial growth generates high-density threading dislocations, which consequently affect the radiative property the subsequent device [28]. Although recently an emission at 210 nm under current injection has been demonstrated, the external quantum efficiency remains extremely low (10^{-6} %) due to the high dislocation density which originates from the heteroepitaxial growth of AlN epilayer and SiC [21]. An AlN layer with a smooth surface and a low defect density is a pre-requisite to realize high-efficiency devices.

To obtain high-quality AlN, several growth methods were proposed. Although high-temperature growth above 1300 °C has been demonstrated to considerably improve film quality, [23, 29] issues such as impurity doping may pose problems. Another option is an alternating supply of group III and V source precursors, which enables growth at 1200 °C [19, 20, 30–35]. Migration-enhanced epitaxy (MEE) has realized high-quality AlN by enhancing Al adatom migration and consequent lateral growth [33, 35]. The full-width at half-maximum (FWHM) of a (0002) x-ray diffraction (XRD) ω-scan can be as narrow as 50 arcsec [33]. A modified MEE, which is characterized by a combination of simultaneous source supply and conventional MEE, has also been proposed [31, 34]. In addition to source flow sequences, the nucleation layer appears to be a key factor for obtaining high-quality epilayers; in fact, low-temperature (LT) [33, 35] and high-temperature [31, 34] AlN have been

employed, although some research groups did not use either of these [27, 29]. Such a fragmentary understanding of the AlN growth is, we believe, largely due to the lack of investigations on the initial stages of growth.

1.3 Status of AlGaN/AlN Quantum Wells

By sandwiching a thin layer of one semiconductor between two layers of another semiconductor with greater band gap, it is possible to create a discontinuity in the conduction and valence band edges. Whereas in the bulk material the electrons and holes are free to move in three dimension, in this structure called quantum well (QW) structure, electrons and holes are confined in one dimension and they are free to move only in two dimension (two degrees of freedom). The confinement of electrons and holes respectively in the conduction and valence band by the potential barriers at each side due to the discontinuity quantizes the states along the direction of confinement. Therefore this enhances the recombination of the carriers thereby the emission efficiency.

The ultimate goal for improving the quality of AlN is for it as to serve as template for fabricating the active AlGaN/AlN quantum well layer. When AlN has a reduced defect density, the generation of defects from AlN into the active layer is also reduced. Thus the non-radiative recombination centers (NCR's) which are the culprit in achieving high-efficiency UV emitters are also suppressed .

However, the fabrication of high-Al content $Al_xGa_{1-x}N$/AlN QWs has been found difficult with increasing Al incorporation. AlGaN-based multiple QWs achieving the highest external quantum efficiency of (η_{ext}) of 0.2 % [24] so far has already been demonstrated. Yet, this recorded efficiency is still very low compared to that obtained in InGaN QWs. Moreover, an In-free UV laser diode emitting at 342.3 nm was demonstrated recently. This device uses MQWs of $Al_{0.04}Ga_{0.96}N$ surrounded by $Al_{0.14}Ga_{0.86}N$ barrier layers [36]. Although the wavelength is only a small step lower from the previous record of 343 nm [43], this hails as a milestone toward making shorter-wavelength devices.

1.3.1 Unique Property in AlN and AlGaN

An interesting optical property is expected for AlN and AlGaN. This is because of the fact that its optical properties are directly related to their valence

band structure where it is split both by the spin-orbit interaction (δ_{so}) and by the non-cubic crystal-field (Δ_{cr}) splitting energy [37–41] near the Γ point in the Brillouin zone, leading to the three states from the top are: Γ_7, Γ_9 and Γ_7. On the other hand, because of the positive Δ_{cr} in GaN, the valence band order from the top is: Γ_9, Γ_7, and Γ_7. Because of this, the transition between the lowest conduction band and top-most valence band is different between AlN and GaN where in AlN, the Γ_7 is the crystal-field split off hole and (CH) governed by the $p_z$like state, and the Γ_9 in GaN is the heavy hole (HH) band governed by p_x-and p_y-like states. This optical selection rule influences the optical properties of AlGaN alloy, where the emission from high-Al content $Al_xGa_{1-x}N$ is expected to be polarized along the c-axis ($\boldsymbol{E} \parallel$ c) while the low-Al content $Al_xGa_{1-x}N$ is expected to be polarized perpendicular to the c-axis ($\boldsymbol{E} \perp$ c). This optical polarization anisotropy in $Al_xGa_{1-x}N$ is has been demonstrated in thick $Al_xGa_{1-x}N$ layers, where the emission polarization switch from ($\boldsymbol{E} \perp$ c) to ($\boldsymbol{E} \parallel$ c) at $x = 0.25$ [42].

The result of this observation implies that a weak surface emission can be obtained from c-oriented Al-rich $Al_xGa_{1-x}N$. This is a draw-back for DUV surface-emitting devices such as LED. In order to observe intense surface emission in Al-rich $Al_xGa_{1-x}N$, fabrication along non-polar planes are strongly considered. However, this is hampered y the growth technology along this planes which is still in infancy. One of the aims of this study is to study the optical polarization properties in AlGaN/AlN QWs. To do this, the QWs will be grown on sapphire substrates.

1.4 Research Purpose/Motivation

The main purpose of this study is to fabricate an AlGaN/AlN QWs emitting at DUV spectal range. To achieve this, first, the quality of the AlN template must be improved first. This is done by using modified MEE - which is hybridized from MEE and the conventional simultaneous source-supply such that the latter is inserted in-between the former. Then this method is adopted for the fabrication of AlGaN/AlN QWs. The systematic study of the structural and optical properties both for AlN and AlGaN/AlN will be performed.

Obtaining high-efficiency AlGaN-based UV-emitters has been perceived difficult to achieve. Though the first step which is by improving the AlN has shown some remarkable progress, moving on to the fabrication of the active layer proved more difficult. Aside from the knowledge of the fundamental

optical properties of AlN and GaN, the optical properties of the ternary AlGaN alloy formed from these binary alloys are still completely unexplored. With the aim of 100 % emission efficiency, the fundamental properties of these materials must be understood in detail. The introduction of a new method in fabricating both AlN and AlGaN/AlN QWs is hoped pave the way for a better understanding of the structural and the optical properties of AlN and AlGaN/AlN QWs structure.

1.5 Thesis Outline

In this thesis, the structural and optical characterizations of AlN and AlGaN/AlN QWs are presented. The contents are systematically divided into five chapters, as explained below.

Chapter 1 gives the history of III-V nitride semiconductor research from its humble beginning to its remarkable achievements throughout the years. Then a short overview is given on the current research trend in III-V nitride materials which is the visible region. As trend of the the future which is the ultraviolet region, the current status on AlN - being the widely-researched III-V semiconductor material, is presented. In this chapter also, the interesting optical property of AlN is briefly discussed. Towards the end of this chapter, the purpose and motivation of this study are presented.

Chapter 2 focuses on the fabrication of high-quality AlN epilayer. This is done by comparing the structural quality of AlN grown by conventional simultaneous method and MEE. Judging from the compromising structural qualities of AlN, a hybridized method based from the former two m are introduced and used to fabricate AlN. As it turned out to have better structural quality, the reason for such is investigated and the clue is found through their initial nucleation stages. Thus, the initial stages of the three methods are compared. Discussions on this matter is throughly presented.

Chapter 3 elaborates on the optimization of growth parameters to obtain high-quality AlN by modified MEE. These growth parameters are growth temperature and the ratio of the source precursors. Then several analysis are performed to assess the epilayer quality such as AFM, x-ray measurements, an chemical etching. The optical properties are also evaluated by photoluminescence (PL) measurements.

After confirming the quality of the AlN epilayer, fabrication of a quantum well structure is performed and elucidated in Chapter 4. For this fabrication, the modified MEE method is used. By changing the growth temperature for

QW fabrication the Al incorporation is varied such that Al composition $x > 0.69$ is obtained (Al-rich $Al_xGa_{1-x}N$/AlN QWs). The successful fabrication of QW layers are confirmed by XRD measurements - estimating the Al composition and well dimensions then confirmed further by x-ray rocking curve simulation. At the end of this chapter various optical characterizations are performed and are listed down in this chapter.

To examine the unique optical properties in AlGaN, In chapter 5, the optical polarization anisotropy of AlN and Al-rich $Al_xGa_{1-x}N$/AlN are performed by PL. By this study an interesting results on the polarization property is discovered. This is related to the enhancement of the surface emission of c-oriented Al-rich $Al_xGa_{1-x}N$/AlN QW devices. A simple model is presented and it agreed very well with the calculation after considering the in-plane compressive strain and quantum confinement due to narrow wells and/or internal electric fields.

References

[1] J. Black, H. Lockwood, and S. Mayburg, "Recombination Radiation in GaAs," *J. Appl. Phys.*, **34**, 178, (1962).

[2] N. Holonyak, Jr., and S. F. Bevacqua, "Coherent (Visible) Light Emission from $Ga(As_{1-x}P_x)$ Junctions," *Appl. Phys. Lett.*, **1**, 82, (1962).

[3] R. D. Dupuis, "An Introduction to the Development of the Semiconductor Laser," *IEEE J. Quant. Electr.*, **QE-23**, 651, (1987).

[4] M.G. Craford, "LEDs Challenge the Incandescents," *IEEE Circuits and Dev.*, **8**, 25,(1992).

[5] M. Feneberg, J. Daubler, K. Thonke, and R. Sauer, "Mahan Excitons in Degenerate Wurtzite InN: Photoluminescence Spectroscopy and Reflectivity Measurements," *Phys. Rev. B,* **77**, 245207, (2008).

[6] S. Strite and H. Morkoć, "GaN, AlN, and InN: A Review," *J. Vac. Sci. Technol.*, **B10**, 1237, (1992).

[7] R. A. Metzger, "Turning Blue to Green," *Comp. Semicond.*, **1**, 26, (1995).

[8] H. Amano, N. Sawaki, I. Akasaki, and Y. Toyoda, "Metalorganic Vapor Phase Epitaxial Growth of a High Quality GaN Film Using an AlN Buffer Layer," *Appl. Phys. Lett.*, **48**, 353, (1986).

[9] S. Nakamura, "GaN Growth Using GaN Buffer Layer," *Jpn. J. Appl. Phys.*, **30**, L1705, (1991).

[10] H. Amano, N. Sawaki, and I. Akasaki, "P-type Conduction in Mg-Doped GaN Treated with Low-Energy Electron Beam Irradiation (LEEBI)," *Jpn. J. Appl. Phys.*, **28**, L2112, (1989).

[11] S. Nakamura, T. Mukai, M. Senoh and N. Iwasa , "Thermal Annealing Effects on P-Type Mg-Doped GaN Films," *Jpn. J. Appl. Phys.*, **31**, L139, (1992).

[12] S. Nakamura, T. Mukai, and M. Senoh, "Candela-Class High-Brightness InGaN/AlGaN Double-Heterostructure Blue-Light-Emitting-Diodes," *Appl. Phys. Lett.*, **64**, 1687, (1994).

[13] S. Nakamura, M. Senoh, N. Iwasa, and S. Nagahama, "High-Brightness InGaN Blue, Green and Yellow Light-Emitting Diodes with Quantum Well Structures," *Jpn. J. Appl. Phys.*, **34**, L797, (1995).

[14] S. Nakamura, M. Senoh, S. Nagahama, N. Iwasa, T. Yamada, T. Matsushita, Y. Sugimoto, and H. Kiyoku, "Room-Temperature Continuous-Wave Operation of InGaN Multi-Quantum-Well Structure Laser Diodes," *Appl. Phys. Lett.*, **69**, 4056, (1996).

[15] P. Waltereit, O. Brandt, A. Trampert, H. T. Grahn, J. Menniger, M. Ramsteiner, M. Reiche, K. H. Ploog, "Nitride Semiconductors Free of Electrostatic Fields for Efficient White Light-Emitting Diodes," *Nature*, **406**, 865, (2000).

[16] Y. Horikoshi, M. Kawashima, and H. Yamaguchi, "Low-Temperature Growth of GaAs and AlAs-GaAs Quantum-Well Layers by Modified Molecular Beam Epitaxy," *Jpn. J. Appl. Phys., Part 2,* **25**, L868, (1986).

[17] M. A. Khan, J. N. Kuznia, D. T. Olson, T. George, and W. T. Pike, "GaN/AlN Digital Alloy Short-period Superlattices by Switched Atomic Layer Metalorganic Chemical Vapor Deposition," *Appl. Phys. Lett.*, **63**, 3470, (1993).

[18] S. Nakamura, M. Senoh, and T. Mukai, "P-GaN/N-InGaN/N-GaN Double-Heterostructure Blue-Light-Emitting Diodes," *Jpn. J. Appl. Phys., Part 2*, **32**, L8, (1986).

[19] M. Kurimoto, T. Nakada, Y. Ishihara, M. Shibata, T. Honda, and H. Kawanishi, "Tensile Strain Introduced in AlN Layer Grown by Metal-Organic Vapor-Phase Epitaxy on (0001) 6H-SiC with (GaN/AlN) Buffer," *Jpn. J. Appl. Phys.,* **38**, L551, (1999).

[20] M. Hiroki and N. Kobayashi, "Flat Surfaces and Interfaces in AlN/GaN Heterostructures and Superlattices Grown by Flow-Rate Modulation Epitaxy," *Jpn. J. Appl. Phys.*, **42**, 2305, (2003).

[21] M. Taniyasu, M. Kasu, and T. Makimoto, "An Aluminium Nitride Light-Emitting Diode with a Wavelength of 210 Nanometres," *Nature*, **441**, 325, (2006).

[22] M. Shatalov, M. Gaevski, V. Adivarahan, and M. A. Khan, "Room-Temperature Stimulated Emission from AlN at 214 nm," *Jpn. J. Appl. Phys.*, **45**, L1286, (2006).

[23] M. Imura, K. Nakano, T. Kitano, N. Fujimoto, N. Okada, K. Balakrishnan, M. Iwaya, S. Kamiyama, H. Amano, I. Akasaki, K. Shimono, T. Noro, T. Takagi, and A. Bandoh, "Microstructure of Thick AlN grown on Sapphire by High-Temperature MOVPE," *Phys. Stat. Sol. (a)*, **203**, 1626, (2006).

[24] Hideki Hirayama, Norimichi Noguchi, Tohru Yatabe, and Norihiko Kamata, "227 nm AlGaN Light-Emitting Diode with 0.15 mW Output Power Realized using a Thin Quantum Well and AlN Buffer with Reduced Threading Dislocation Density," *Appl. Phys. Express,* **1**, 051101, (2008).

[25] N. Onojima, J. Suda, and H. Matsunami, "High-Quality AlN by Initial Layer-by-Layer Growth on Surface-Controlled 4H-SiC(0001) Substrate," *Jpn. J. Appl. Phys., Part 2,* **42**, L445, (2003).

[26] Q. Paduano and D. Weyburne, "Two-step Process for the Metalorganic Chemical Vapor Deposition Growth of High Quality AlN Films on Sapphire," *Jpn. J. Appl. Phys.* **42**, 1590, (2003).

[27] T. Shibata, K. Asai, S, Sumiya, M. Mouri, M. Tanaka, O. Oda, H. Katsukawa, H. Miyake, and K. Hiramatsu, "High-quality

AlN Epitaxial Films on (0001)-faced Sapphire and 6H-SiC Substrate," *Phys. Stat. Sol. (c),* **0**, 2023, (2003).

[28] J.F. Kaeding, Y. Wu, T. Fujii, R. Sharma, P.T. Fini, J.S. Speck, and S. Nakamura, "Growth and Laser-Assisted Liftoff of Low Dislocation Density AlN thin films for Deep-UV Light-Emitting Diodes," *J. Cryst. Growth,* **272**, 257, (2004).

[29] K. Balakrishnan, A. Bandoh, M. Iwaya, S. Kamiyama, H. Amano, and I. Akasaki, "Influence of High Temperature in the Growth of Low Dislocation Content AlN Bridge Layers on Patterned 6H-SiC Substrates by Metalorganic Vapor Phase Epitaxy," *Jpn. J. Appl. Phys.,* **46**, L307, (2007).

[30] V. Adivarahan, W. H. Sun, A. Chitnis, M. SHatalov, S. Wu, H. P. Maruska, and M. A. Khan, "250 nm AlGaN Light-Emitting Diodes," *Appl. Phys. Lett.,* **85**, 2175, (2004).

[31] M. Takeuchi, H. Shimizu, R. Kajitani, K. Kawasaki, Y. Kumagai, A. Koukitu, and Y. Aoyagi, "Improvement of Crystalline Quality of N-polar AlN Layers on c-plane Sapphire by Low-pressure Flow-modulated MOCVD," *J. Cryst. Growth,* **298**, 336, (2007).

[32] H. Hirayama, T. Yatabe, N. Noguchi, T. Ohashi, and N. Kamata, "231 - nm AlGaN Deep-Ultraviolet Light-Emitting Diodes Fabricated on AlN Multilayer Buffers Grown by Ammonia Pulse-Flow Method on Sapphire," *Appl. Phys. Lett.,* **91**, 071901, (2007).

[33] J. P. Zhang, M. A. Khan, W. H. Sun, H. M. Wang, C. Q. Chen, Q. Fareed, E. Kuokstis, and J. W. Yang, "Pulsed Atomic-Layer Epitaxy of Ultrahigh-Quality $Al_xGa_{1-x}N$ Structures for Deep Ultraviolet Emissions below 230 nm," *Appl. Phys. Lett.,* **81**, 4392, (2002).

[34] M. Takeuchi, S. Ooishi, T. Ohtsuka, T. Maegawa, T. Koyama, S. F. Chichibu, and Y. Aogi, "Improvement of Al-Polar AlN Layer Quality by Three-Stage Flow-Modulation Metalorganic Chemical Vapor Deposition," *Appl. Phys. Express,* **1**, 021102, (2008).

[35] J. P. Zhang, H. M. Wang, W. H. Sun, V. Adivarahan, S. Wu, A. Chitnis, C. Q. Chen, M. Shatalov, E. Kuokstis, J. W. Yang and M. A. Khan, "High-Quality AlGaN Layers over Pulsed Atomic-Layer Epitaxy (PALE) Grown AlN Templates for Deep Ultraviolet Light-Emitting Diodes," *J. Elec. Materials,* **32**, 364, (2003).

[36] H. Harumasa, Y. Yamashita, M. Kuwabara and H. Khan, "A 342-nm Ultraviolet AlGaN Multiple-Quantum Well Laser Diode," *Nature Photonics,* **2**, 551, (2008).

[37] M. Suzuki and T. Uenoyama, "First-Principles Calculations of Effective-Mass Parameters of AlN and GaN," *Phys. Rev. B,* **52**, 8132, (1995).

[38] S. H. Wei and A. Zunger, "Valence Band Splittings and Band Offsets of AlN, GaN, and InN," *Appl. Phys. Lett.,* **69**, 2719, (1996).

[39] J. Li, K.B . Nam, M. L. Nakarmi, J. Y. Lin, H. X. Jiang, P. Carrier, and S. H. Wei, "Band Structure and Fundamental Optical Transitions in Wurtize AlN," *Appl. Phys. Lett.,* **83**, 5163, (2003).

[40] E. Silveira, J.A. Freitas Jr., O.J. Glembocki, G.A. Slack, and L. J. Schowalter, "Excitonic Structure of Bulk AlN from Optical Reflectivity and Cathodoluminescence Measurements," *Phys. Rev. B,* **71**, 041201, (2005).

[41] Y. Taniyasu, M. Kasu, and T. Makimoto, "Radiation and Polarization Properties of Free-Exciton Emission from AlN (0001) Surface," *Appl. Phys. Lett.,* **90**, 261911, (2007).

[42] K. B. Nam, J. Li, L. Nakarmi, J. Y. Lin, and H. X. Jiang, "Unique Optical Properties of AlGaN Alloys and Related Ultraviolet Emitters," *Appl. Phys. Lett.,* **84**, 5264, (2004).

[43] J. Edmond, A. Abare, M. Bergman, J. Bharathan, K. Lee Bunker, D. Emerson, K. Haberern, J. Ibbetson, M. Leung, P. Russel, and D. Slater, "High Efficiency GaN-based LEDs and Lasers on SiC," *J. Cryst. Growth,* **272**, 242, (2004).

Chapter 2

Effect of Growth Methods on the Crystalline Quality of AlN

This chapter discusses the growth of AlN on sapphire substrates by different methods - all based on metalorganic vapor phase epitaxy (MOVPE). Firstly, a brief background about MOVPE growth method will be discussed. Secondly, the growth of AlN by conventional simultaneous source-supply method and its modification by alternating the trimethylaluminium (TMA) and NH_3 precursors, a method which is called Migration Enhanced Epitaxy (MEE), will be presented. Lastly, judging the structural qualities of the epilayer obtained from these conventional and MEE methods, a new growth method will be proposed and the differences in their structural quality will be correlated to their initial growth stages.

2.1 Metalorganic Vapor Phase Epitaxy

2.1.1 Introduction

In this study, the AlN epilayers were grown by metalorganic vapor-phase epitaxy (MOVPE) method. MOVPE is a chemical vapor deposition process used for growing epitaxial layers from the surface reaction of or source gases and NH_3. For the case of Al(Ga)N growth, trimethylaluminum [$(CH_3)_3$Al: TMA] and trimethylgallium [$(CH_3)_3$Ga: TMG] are used as metalorganic sources. For the growth of AlN, TMA is carried by H_2 gas into the reactor and made to react with NH_3. This simple reaction can be expressed as

$$Al(CH_3)_{3_{(vap)}} + NH_{3(gas)} \rightarrow AlN_{(s)} + 3CH_4 \uparrow . \qquad (2.1)$$

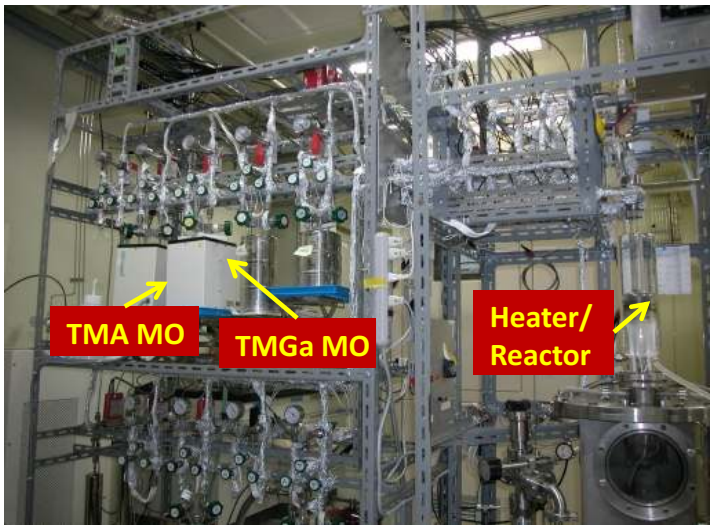

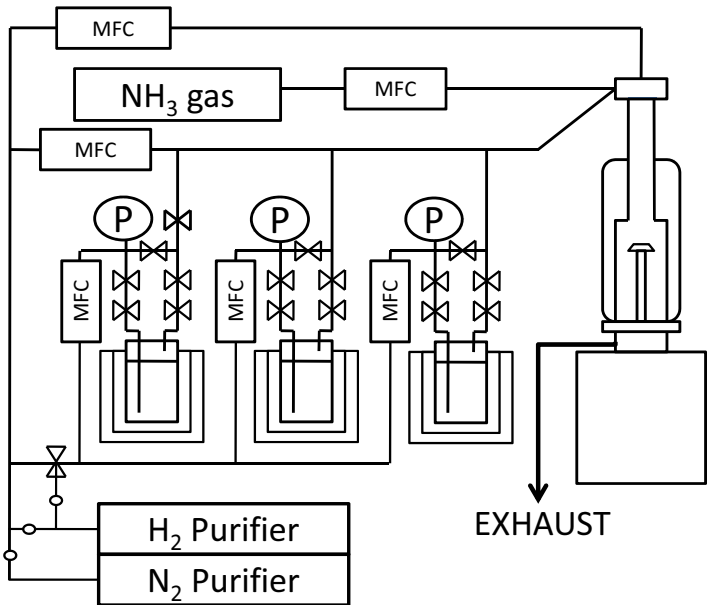

Figure 2.1: (a) Image of Metalorganic Vapor Phase Epitaxy (MOVPE) growth machine used in this study to grow AlN (and AlGaN/AlN) epilayers and, (b) the schematic of MOVPE machine.

The advantage of MOVPE over other techniques is the suitability for large-scale production and its versatility where virtually all III-V and II-VI semiconductor compounds and alloys can be produced [1]. Figure 2.1 shows the schematic of MOVPE used in this study. The metalorganic precursors are kept in a bubbler where the bubbling temperature is controlled. The H_2 gas carries the vapor into the reactor. In a separate line NH_3 gas is introduced. The separate flow of these sources into the reactor is to minimize gas-phase pre-reaction of precursors. To prevent desorption from the wall of the reactor, a cold-wall type reactor is used. The reactor is made of quartz and the design is such that a hollow between the outer and inner reactor walls is for the purpose cooling water circulation. Also, the reactor is a vertical type where all the sources are positioned to enter from the top of the reactor. The exhaust gases (H_2, N_2, and MO by-products) are treated accordingly in a scrubber before they are released into the atmosphere.

2.1.2 Modification of MOVPE Operation

The MOVPE used in this study has the capability to be controlled semi-automatically. When one wishes to modify or employ a new growth method by alternating the sources, it can be done with ease. A computer terminal can be connected to the circuit board in the MOVPE where the operation of each precursor valve can be controlled by a computer program. For the case of AlN and AlGaN growth, TMA line, TMGa line and NH_3 line can be controlled according to what is specified in the program. This in turn allows for the modification of supply sequence of each TMA, TMG and NH_3 precursors. In this study, the continuous source-supply of precursors normally employed in conventional MOVPE is modified by alternating the introduction of source-precursors into the reactor.

The computer program is created from *Labview* of *National Instruments* [2]. The program is designed in such a way that the sequential supply precursor (e.g., which goes first into the reactor) can be controlled. Then the duration time of each precursors is also controlled independent from one another. Since the "triggering"of each valve takes time, it is made sure that the duration time for each valve is above this minimum response time of 0.5 s. For AlN growth, there are four independent valves that must be controlled. These are: TMA Run valve, TMA vent valve, NH_3 run valve, and NH_3 vent valve. For the "run" valve, the corresponding precursor goes into the reactor while for the "vent" valve, it does not go into the reactor but into the "vent"

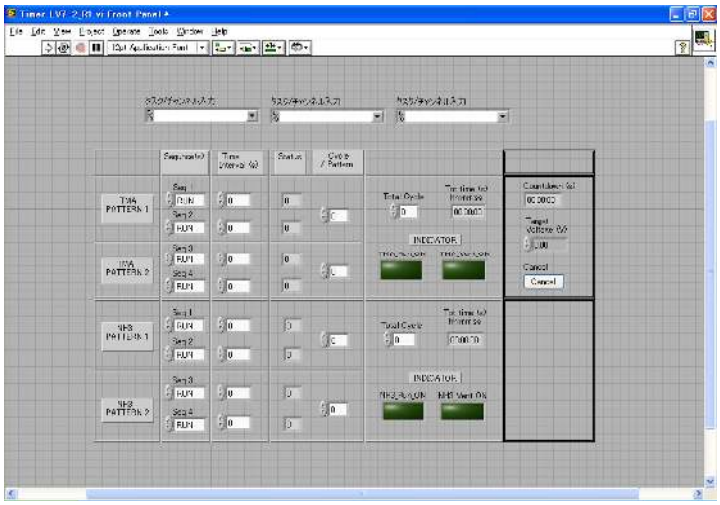

Figure 2.2: The *Labview* program for controlling independently the individual tasking of TMA and NH_3 precursor valves.

line. A simple program made using *Labview* is shown in Figure 2.2.

2.2 Metalorganic Vapor Phase Epitaxy of AlN

In this section, the growth of AlN by MOVPE will be discussed. As mentioned, the conventional simultaneous source-supply method will be used at first, then because of the compromising structural quality of AlN, migration enhanced epitaxy (MEE) technique will be introduced. However, the quality of the epilayer by MEE is still inferior and at this time, new method will be developed.

2.2.1 Simultaneous and Migration Enhanced Epitaxy of AlN

The simultaneous supply method is, as the name suggests, the continuous supply of precursors (e.g., TMA and NH_3) without interruption until the desired thickness of the epilayer is achieved. This method is exhaustively used even beyond MOVPE (i.e., MBE and HVPE) being simple and does not require any special accessory to carry out the task. This method is schematically shown in Figure 2.3.

For the improvement of AlN, this conventional technique was used to grow AlN epilayers at growth temperatures above 1400 °C [3]. At these high temperatures, a relatively thick AlN of up to 10 μm was grown with an atomically-smooth surface. However, the crystalline quality as measured by the ω-scan (XRC) full-width at half-maximum (FWHM) of symmetric (0002) plane was 446 arcsec, which is longer compared to those grown at lower temperatures by using the same method [4–8]. Also, problem with doping could be a problem when fabricating an active layer such as AlGaN/AlN quantum wells where the efficiency of Ga incorporation in the well layer becomes drastically reduced. Moreover, because high-temperature growth is employed, the reactor must be re-configured to withstand such high temperatures.

For the case of alternating supply method, specifically, for AlN, NH_3 is supplied first for a certain time then followed by TMA. It is emphasized that there is no overlap between each precursor thus this method can also be classified as perfectly alternating. An example of a perfect alternating supply method is MEE. This method was first proposed for low-temperature growth of GaAs and AlAs-GaAs quantum well structures [9]. The idea of alternating supply of precursor emerged because of the large difference of the migration of Ga even at low temperature regime, guaranteeing the high-quality epitax-

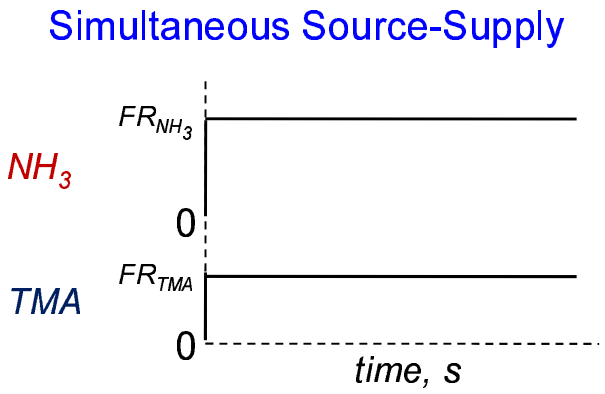

Figure 2.3: The conventional simultaneous source-supply of TMA and NH_3 precursors used to grow AlN. The characteristic of this method is, the simultaneous supply of precursor until the desired thickness is achieved.

ial growth. It was in the year 1992 that the this method was first applied for AlN [10] at low-pressure (76 Torr). Because of this, the quality of the epilayer was improved. Moreover, the growth was also performed at a temperature as low as 750 °C but the optimum temperature was 1040 °C. Then this method was used for the fabrication an atomically-smooth GaN-AlN short-period superlattice (SL) structure [11]. By employing this method, it further supported its effectiveness to improve the overall structural and optical properties of AlN.

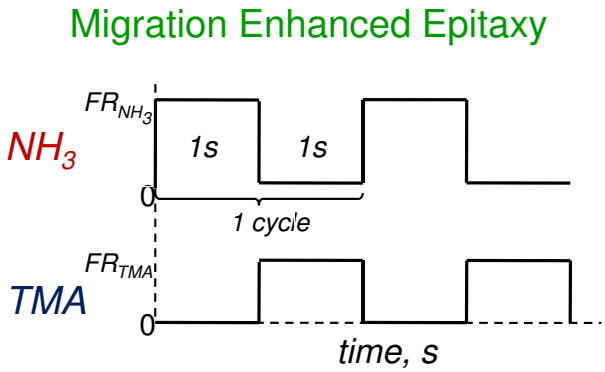

Figure 2.4: Alternating supply sequence of TMA and NH_3 in MEE. This method was first applied in GaAs and AlAs-GaAs system then eventually adapted for AlN growth.

2.2.2 New Approach for the improvement of AlN

It has been reported that the benefit of the separate supply of precursors is to take advantage of rapid migration of Ga [9] thus allowing the growth to be performed even at low temperatures. On the other hand, based on the results by Khan et. al [12], a smoother surface obtained was attributed to the enhanced surface migration (λ) of Al adatoms. Moreover, they also reported a reduction of pre-reaction between TMA a NH_3 and an increase of growth rates. However, no qualitative evidences supporting those observations above were presented thus leaving a room for clarifying this important issue.

The need for migration enhancement of adatoms in III-V nitrides is due to their differences in cohesive energies. Their respective cohesive energies per bond are 2.88 eV (63.5 kcal/mol), 2.20 eV (48.5 kcal/mol) and 1.93 eV (42.5 kcal/mol) for AlN, GaN and InN, respectively [14]. Among these nitrides, AlN has the highest cohesive energy therefore Al adatoms easily react with nitrogen. Because of this, the migration length is expected to be much lower for AlN than the other two materials. This smaller migration length results in rough surface morphology which compromises the device performance and crystalline quality.

To enhance the surface diffusion of Al adatoms, an effective way is to increase the growth temperature of AlN. It is known that diffusion is an activated process and generally follows an Arrhenius-like behavior:

$$D(\lambda, T) = D_0 \exp\left(-\frac{E_a}{kT}\right), \tag{2.2}$$

where $D(\lambda, T)$ is the diffusion coefficient; E_a is the activation energy barrier ; T is the absolute temperature and D_0 is the pre-exponential diffusivity constant. From this diffusion coefficient $D(\lambda, T)$, the average migration length λ of adatom can be determined by

$$\lambda = \sqrt{Dt}. \tag{2.3}$$

Growth of AlN epilayer was performed at high-temperatures between 1300 °C and 1600 °C on sapphire substrates [3]. It was reported that a successful achievement of high-quality and thick (>10 nm) AlN. However, when the growth temperature was more than 1450 °C, the morphology deteriorated. Thus, the optimized temperature was chosen to be 1400 °C. However, another problem could arise during doping process where such high vapor pressure may limit the incorporation of Ga species into the quantum well structure. Moreover, the present designs of most common reactor are not ready for such

high temperature growth. This may pose as a big issue when growing AlN at such high temperature.

Owing to these problems, the alternating supply of precursors could be the better alternative wherein growth at such high temperature can be prevented. This method adopted for AlN growth is called MEE [15]. Though no experimental evidence to support the enhanced migration, it was speculated that this method enhances the diffusion length of Al adatoms. Furthermore, in their technique, the Al diffusion is enhanced by pulse supply of NH_3 in two ways. Firstly, the lower NH_3 to TMA (V/III) ratio enhances the Al diffusion and secondly, by continuous supply of TMA during the off period of NH_3, the surface is saturated with Al thus further decreasing the Al entrapment on the surface [16]. In addition, because of the alternating nature of precursor supply, the gas-phase pre-reaction is also minimized.

2.3 Structural quality of AlN by Simultaneous and MEE

The quality of AlN is verified by growing the epilayer by MEE and simultaneous methods. Figure 2.5 shows the temperature profile used to grow AlN epilayer. One growth cycle of MEE is composed of 1 s supply of NH_3 followed by 1 s supply of TMA. This is repeated cyclically until ∼600-nm-thick epilayer is achieved. As observed, no buffer layer was applied in this study and the reason will be explained in Chapter 3. Expectedly, an optimized growth condition was used as tabulated in Table 2.1. All throughout, the total pressure was kept at 76 Torr. After placing the sample above the susceptor, the temperature was ramped up to 1225 °C where annealing was performed under the stream of H_2 gas for 10 minutes. After thermal annealing, the temperature was brought down to 1200 °C. After temperature has stabilized, the growth of AlN followed, where the flowrates of TMA and NH_3 precursors used are shown in the inset of Figure 2.5.

The grown AlN epilayer has a thickness of ∼600 nm and their surface morphologies were compared. The atomic force microscopy (AFM) (5 μm x 5 μm) images of their corresponding surfaces are shown in Fig 2.6. For AlN grown by simultaneous method, an incomplete island coalescence is observed, as demonstrated by large pits (∼10-50 nm). Also, the observation by Nomarski microscopy showed that the Al particles were deposited on the surface, as depicted by arrows in the figure. On the other hand, pits were

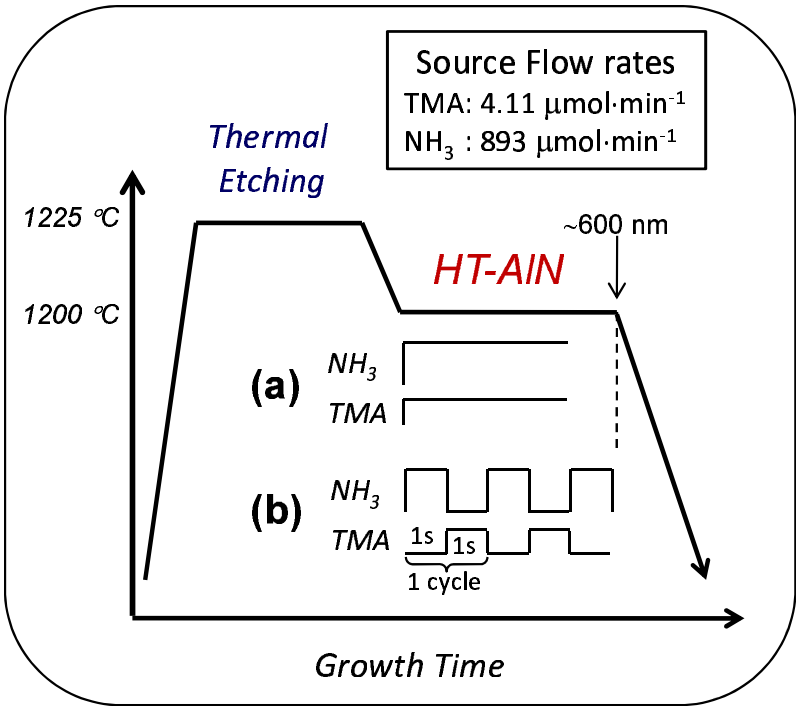

Figure 2.5: Temperature profile of growth of AlN by (a) simultaneous source-supply and, (b) MEE.

also observed in MEE but they are comparatively smaller than those found in simultaneous supply. These pits were also observed in ∼300-nm-thick AlN using the same growth method [12]. Such occurrence of pits were attributed to the thin epilayer (∼300 nm). No Al particles were also observed in AlN grown by this method. However, despite these defects found on the surface, still, the surface roughness was atomically-flat. The surface root-mean-square (RMS) roughness 0.52 nm for AlN grown by simultaneous supply while MEE 0.35 nm for MEE-grown AlN.

These observations suggest that AlN epilayer can still be improved by di-

Table 2.1: Optimized growth condition parameters used for growing AlN epilayer by MEE and simultaneous supply.

Growth Parameters	Optimized Values
Sample	α-Al_2O_3 (4mm × 5mm)
Annealing Temperature	1220 °C
Growth Temperature	1200 °C
Total Pressure	76 Torr
TMA	4.11 μmol/min
NH_3	893 μmol/min

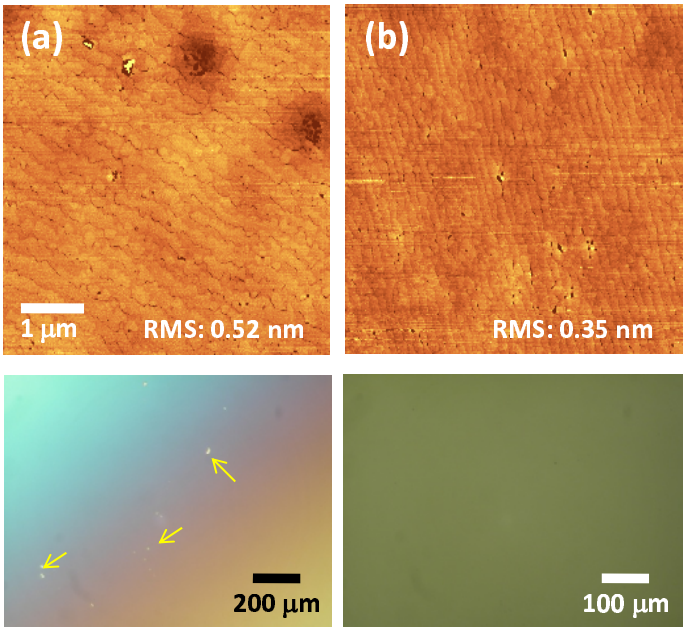

Figure 2.6: AFM surface morphology of (a) simultaneous source-supply and (b) MEE. The Simultaneous source-supply method shows Al deposits while MEE-grown AlN shows no premature deposits on the surface, as seen by optical Nomarski microscope image.

rectly eliminating the structural surface defects (e.g., pits) and the deposited Al particles. Obviously these will not be eliminated using the existing growth methods. Therefore a new growth method is being proposed.

2.4 New Method: Modified MEE

As the realization of pit- and Al-free AlN can only be realized by using a new growth method, in this section, a new growth method will be presented as well its inception. During the conceptualization of a new growth method, the idea of combining both the simultaneous supply and MEE came to light. The combination was concocted such that the simultaneous supply is inserted in-between the MEE. That is how the new came about. Since it was based from MEE, it was called as modified Migration Enhanced Epitaxy, after inserting the simultaneous supply in-between the MEE. The schematic of modified MEE is shown in Figure 2.7. For modified MEE, one growth cycle is composed of 2 s MEE (1 cycle) and 1 s of simultaneous supply, giving a 3 s per cycle.

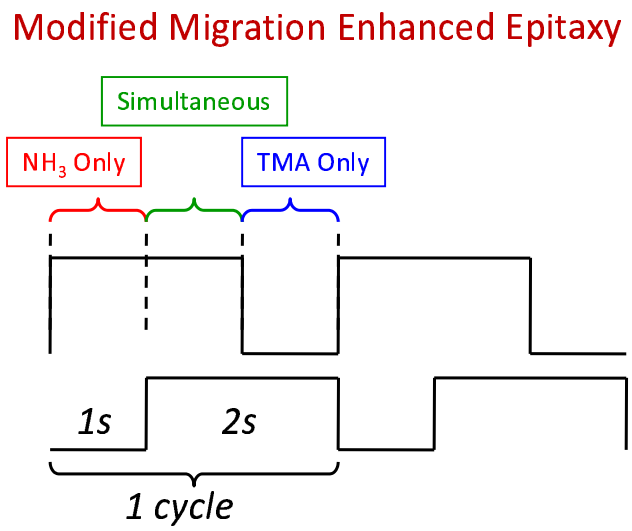

Figure 2.7: Schematic of modified MEE developed as the new growth method.

2.4.1 Comparison with Other Methods

Thus, the modified MEE was also used to grow ~600-nm-thick AlN using the same growth conditions used in simultaneous supply and MEE (2.1). First, the growth rates of each methods were determined from the thickness the epilayer. In modified MEE, 850 cycles (= 0.70 nm/cycle) were necessary to grow ~600-nm- thick AlN while 2750 cycles (= 0.22 nm/cycle)were needed for MEE, and 1200 s (= 0.5 nm/s) for simultaneous supply. Thus, in terms of monolayer (ML) growth, MEE obtains a growth of 1 monolayer per cycle (1ML/cycle), 2 monolayer per second (2 ML/s) for simultaneous supply, and 3 ML/cycle for modified MEE. The summary of the growth rates is tabulated in Table 2.2. Looking at the growth rate relationship among these three methods, we can write this expression:

$$GR_{modified\ MEE} = GR_{Simultaneous} + GR_{MEE}, \tag{2.4}$$

Table 2.2: Comparison of growth rates of simultaneous, MEE and Modified MEE.

Growth Method	Simultaneous	MEE	Modified MEE
Growth Rate	0.50 nm/s	0.22 nm/cycle	0.70 nm/cycle
Monolayer (ML)	2 ML/s	1 ML/cycle	3 ML/cycle

The side-by-side comparison by surface morphologies obtained by AFM

measurements for AlN grown by simultaneous, MEE and modified MEE are shown in Figure 2.8. Among these methods, modified MEE has achieved pit-free and fully-coalesced AlN epilayer. The differences in the terrace widths for AlN grown by different methods is due to the off-set angle of the sapphire substrate.

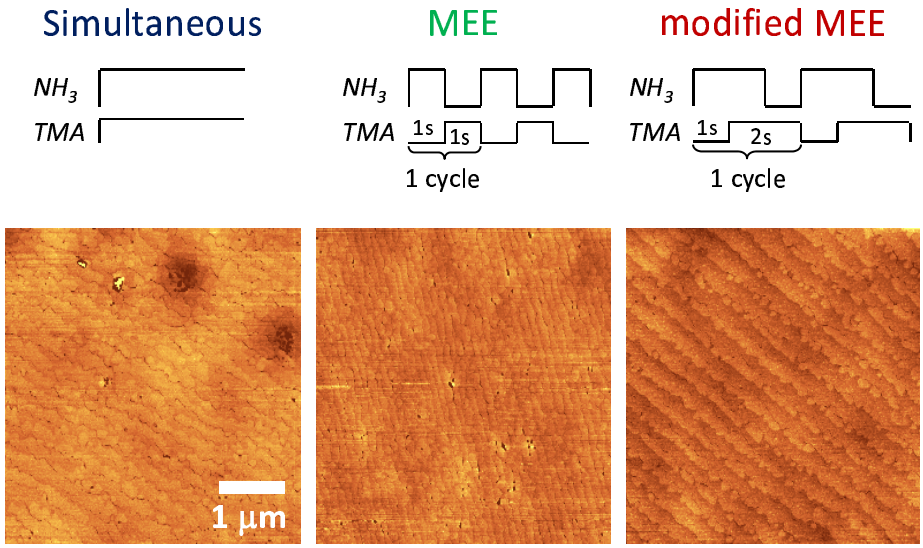

Figure 2.8: Side-by-side comparison of AFM surface morphologies of AlN grown by Simultaneous, MEE and modified MEE methods.

Their structural qualities were also compared by measuring the x-ray rocking curve (XRC) FWHMs of both symmetric (0002) and asymmetric ($10\bar{1}2$) planes. As shown in Table 2.3, surface morphology is directly-related to structural quality as AlN grown by modified MEE achieved the narrowest linewidth. The width of the rocking curve is a direct measure of the range of orientation present in the crystal [13]. A good quality crystal therefore has a small variation in crystal orientation therefore a small linewdith. This is a sufficient evidence that modified MEE can further improve the quality of AlN. However, as how it was improved is a question worthy of deep analysis. The approach to this interesting finding is to look at the initial nucleation stage. It must be recalled that no high- or low-temperature buffer layer was applied for growing the epilayer (1-step growth) thus, the initial nucleation layer could hold to discovering why such high-quality epilayer was obtained.

Table 2.3: Comparison of the structural qualities as measured by XRC measurements of AlN obtained by simultaneous, MEE and modified MEE.

Growth Method	Simultaneous	MEE	Modified MEE
(0002)	52.6 arcsec	45.1 arcsec	31.8 arcsec
$(10\bar{1}2)$	889.1 arcsec	1443.5 arcsec	244.5 arcsec

2.5 Initial Nucleation Stage

The initial nucleation stage was investigated by growing AlN epilayer with thicknesses of ∼2 and ∼14 nm, which are just after AlN nucleation, as well as thicker AlN epilayer just after the coalescence of the initial nuclei. These thicknesses were estimated from the growth rates of AlN measured from ∼50 nm to 600 nm. Since there was no variation in their growth rates, this assumption could also be reasonable even at initial stage. The AFM surface images of AlN at initial are shown in Figure 2.9.

Regardless of growth method used, the initial nuclei were three-dimensional (3-D) islands with a typical diameter of ∼20 nm. The formation of these 3-D nuclei was theoretically predicted: 3-D growth is more favorable than the two-dimensional (2-D) growth due to the chemical and strain mismatch between the sapphire substrate and AlN [17]. However, the differences at the initial nucleation stage is noticeable and each method has a distinct nucleation mode. To describe qualitatively, consider the size of the nuclei of ∼14-nm-thick epilayer. It can be observed that the size of the 3-D islands becomes larger in the order below:

$$\text{Simultaneous } (\phi{:}\sim 15 \text{ nm}) < \text{Modified MEE}(\sim 25 \text{ nm}) < \text{MEE}(\sim 50 \text{ nm}).$$

The size of the nuclei very well suggests the degree of Al migration which is in the same order: simultaneous supply < modified MEE < MEE. Considering this, let us try to compare two extreme cases, that is, MEE and the simultaneous supply methods. For MEE, as clearly observed for the ∼ 2-nm-thick AlN, initial nucleation occurs mostly along the step edges of the sapphire substrate, whereas for the simultaneous supply, random nucleation occurs both at the step-edge and onto the terrace. These distinct initial nucleation behaviors are due to differences in their migration degrees, as schematically illustrated in Figure 2.10. In MEE [Fig. 2.10(a)], migrating Al adatoms easily find sapphire step edges, which are the major nucleation sites, and are preferably adsorbed there. The sharp ridge structure indicates

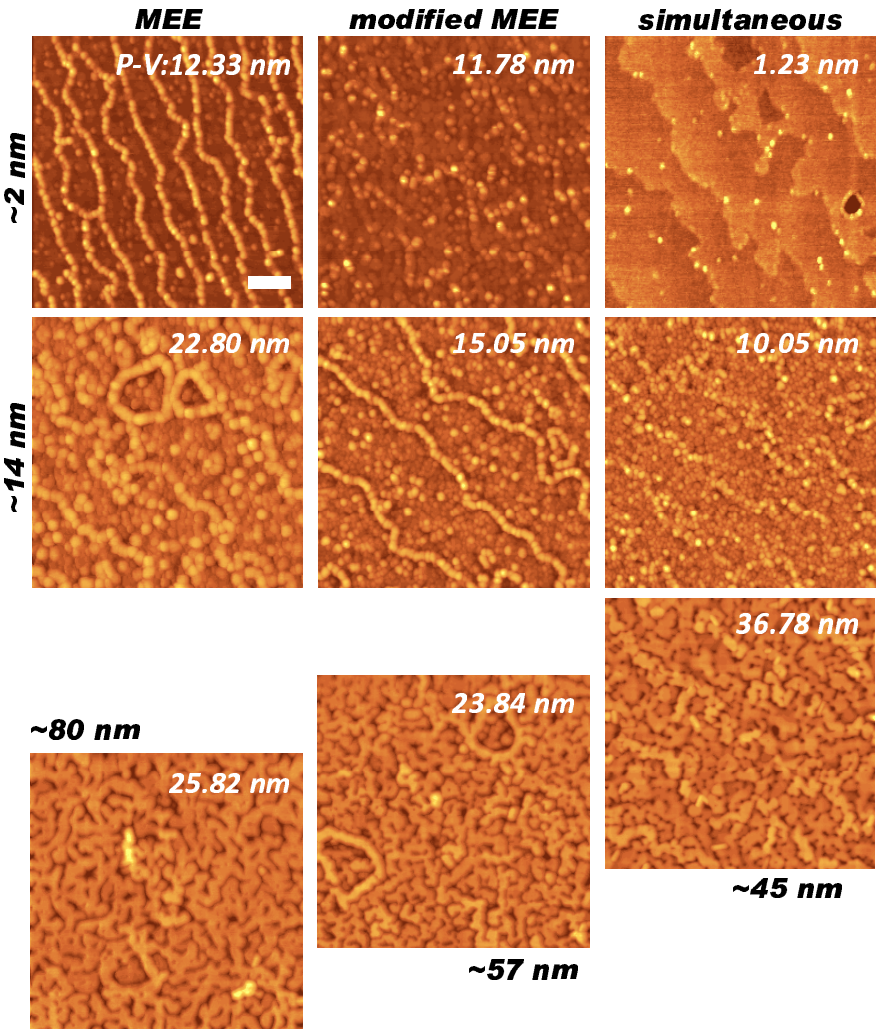

Figure 2.9: AFM images of AlN by MEE, modified MEE and simultaneous supply showing the evolution of initial nucleation. Thicknesses of ∼2 and ∼14 nm are nominal. The scale bar represents 20 nm.

preferential adsorption of migrating Al adatoms onto already-existing AlN nuclei, probably due to the chemical matching between Al adatoms and AlN. These ridges continue to grow until nucleation, which also begins at the terrace, covers the sapphire surface. As shown in Figure 2.9, the larger surface peak-to-valley values for thicker AlN are the consequence. On the contrary, random nucleation observed for the simultaneous supply method strongly suggests a negligible migration [Figure 2.10(c)]. The differences in nucleation behavior for each method as well as the formation of ridge structure is summarized in Table 2.4.

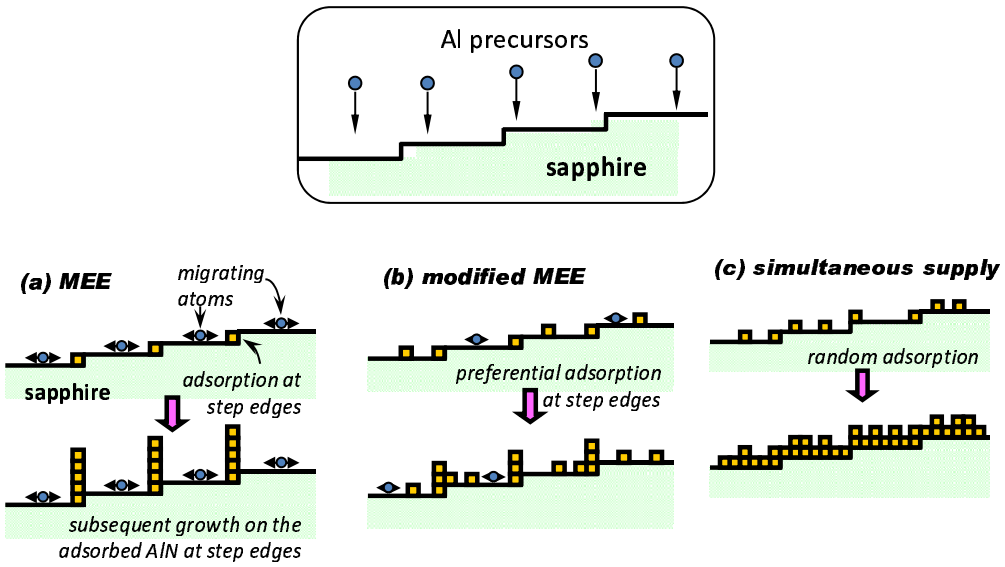

Figure 2.10: Schematic model of initial nucleation of AlN on sapphire. During initial nucleation stage, the migration degree of Al adatoms is different between each method as seen by their nucleation behavior.

Table 2.4: The differences in nucleation behavior of simultaneous, MEE and modified MEE. The distinct nucleation behavior results in differences in ridge formation.

Growth Methods	Simultaneous	MEE	Modified MEE
Nucleation	Random	Preferential	Intermediate
Ridge	Flat	High	Low

Based on the above discussion of growth rates, the nucleation behavior during modified MEE should have intermediate characteristics of MEE and simultaneous supply method. Al adatoms migrate well during the MEE-mode in modified MEE in the presence of many nuclei formed during the

simultaneous-supply mode, which is macroscopically recognized as a smaller diffusivity of Al adatoms compared to MEE. In fact, similar to MEE, ridge structures are observed, but their height is lower than those formed by MEE as demonstrated in Figure 2.9. Figure 2.10(b) schematically illustrates this nucleation model.

The ridge formation apparently roughened the surfaces, as evidenced by AFM presented in Figure 2.9. Higher ridges should require thicker films in order to recover the surface flatness. As shown in Figure 2.9, equivalent surface morphologies that show the coalescence of the initial nuclei are confirmed at 80 nm for MEE, 57 nm for modified MEE, and 45 nm for the simultaneous supply method. Further increasing the AlN thickness promoted coalescence, and eventually, as demonstrated in Figure 2.8, generated a nearly perfectly flat surface at a thickness of 600 nm using modified MEE. The presence of pits in the MEE-grown AlN suggests that it is difficult to recover the surface flatness with this thickness.

Although initial nucleation depends on the growth methods, the influence of this difference on the film quality is clarified. To gain some insight into this issue, the lattice relaxation was assessed by XRD as a variation of the in-plane lattice parameter. Figure 2.11 shows these results. A relaxed epilayer has an in-plane lattice parameter (a) of 3.114 Å. Below this value, the epilayer is strained compressively while above this value, it involves tensile. It can be observed that both MEE and modified MEE trace the same tendency where a 50-nm-thick AlN epilayer involves -0.52% compressive strain. On the other hand, -0.18% compressive strain was measured in 48-nm-thick AlN grown by the simultaneous supply method. These findings indicate a slower strain relaxation in both modified MEE and MEE while fast relaxation is observed for simultaneous supply. The relationship of lattice relaxation between each method is shown in Table 2.5 below. Thus, the initial nucleation (Figure 2.9) implies that the relatively uniform distribution of 3-D nuclei by the simultaneous supply causes homogeneous lattice relaxation, while the ridge structures formed by MEE and modified MEE cause partial relaxation, possibly at the ridges. This difference in the lattice relaxation due to the growth methods may greatly affect the propagation of dislocations.

For GaN MOVPE, LT-GaN has often been used as a nucleation layer because tiny GaN islands, which work as seeds for subsequent high-temperature growth, are formed only at low temperatures. On the contrary, for AlN, the tiny, densely packed nuclei were observed during the initial growth stage even for high-temperature growth, which is why nucleation layers are unnecessary

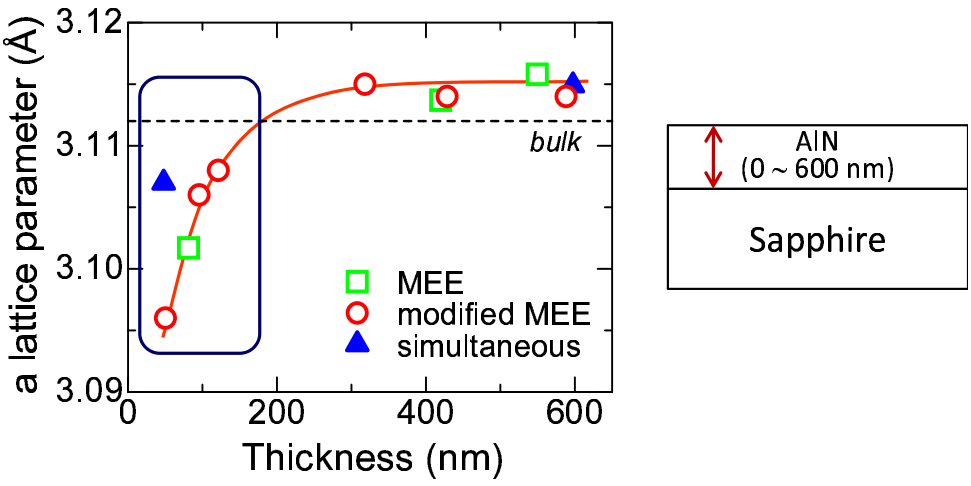

Figure 2.11: AlN a-lattice parameter as a function of film thickness obtained from MEE, modified MEE, and simultaneous supply.

Table 2.5: The differences in Relaxation of AlN epilayer during simultaneous, MEE and modified MEE.

Growth Methods	Simultaneous	MEE	Modified MEE
Lattice Relaxation	Fast	Slow	Slow

for AlN. Furthermore, it is noteworthy that because modified MEE consists of MEE and the simultaneous supply method, the appropriate flow sequence may simultaneously control initial nucleation and the lattice relaxation processes. For example, increasing the occupation of the MEE mode within one cycle of modified MEE promotes the migration of Al adatoms to form higher ridge. Hence, this ability to control the initial growth may be advantageous over other methods.

2.6 Surface Diffusion of Al Adatoms during Quasi-Homoepitaxy

In the previous section 2.5, it was found out that the Al adatom diffusion in heteroepitaxial growth (between sapphire substrate and AlN epilayer) is distinct for each growth method which brought about their differences in initial nucleation behavior. In this section, the diffusion mechanisms of Al adatoms on relatively thick AlN with thicknesses of $400 - 600$ nm is investigated. The growth can hence be regarded as quasi-homoepitaxy. The diffusion mecha-

nism is investigated using sapphire substrates having different unintentional mis-orientations. The substrate mis-orientation was measured from the terrace with different widths and a step with 1 ML height. The mis-orientation angle is calculated using the equation below:

$$\theta = \tan^{-1}\left(\frac{L}{step{-}height[1ML]}\right). \tag{2.5}$$

Figure 2.12 shows the surface morphology obtained by AFM of >600-nm-thick AlN grown by modified MEE. The mis-orientation of sapphire substrate was well-replicated in the grown AlN epilayers. Thus, for AlN epilayer with corresponding terrace width as shown in Table 2.6 below, the mis-orientation angle can be estimated. With increasing the mis-orientation angle, a clear transition of growth modes from two-dimensional (2-D) layer-by-layer growth to step-flow growth is observed. From this transition and, furthermore, from the 2-D nuclei density observed for the layer-by-layer growth, the diffusion length of Al adatoms could be evaluated.

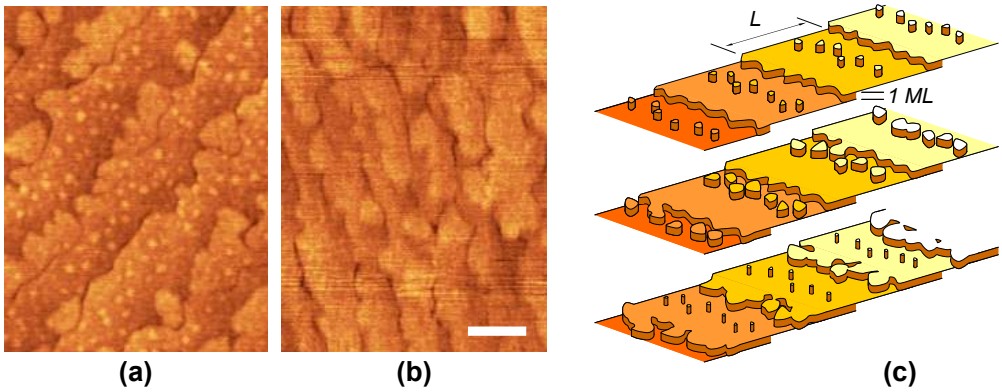

Figure 2.12: AFM images of 600-nm-thick AlN grown on sapphire with un-intentional mis-orientations of (a) ∼0.06° and (b) ∼0.15°. The scale bar represents 200 nm. (c) Schematic of the layer-by-layer growth mode deduced from (a).

Table 2.6: The un-intentional mis-orientation angles of sapphire substrates with different terrace widths.

Terrace Width, L	250 nm	100 nm
Mis-orientation angle, θ	0.06 °	0.15 °

For the substrate with wider terraces [Figure2.12(a)], small 2-D nuclei with a typical diameter of 20 nm were observed particularly around the

middle of the terraces. On the other hand, 2-D nuclei disappeared on the substrate with narrower terraces [Figure 2.12(b)]. These experimental findings are well accounted for by Al adatom diffusion; if the diffusion length, λ, is shorter than half the terrace width, $L/2$, Al adatoms migrating around the middle of the terrace cannot reach the step edges, which are the major sink for adatoms, thus forming critical nuclei on the terrace. This growth is classified as the layer-by-layer growth mode, where 2-D nuclei formed on the terrace grow laterally until they fully cover the surface. These processes are repeated, as illustrated in Figure 2.12(c) until a desired thickness of AlN is achieved.

When $\lambda > L/2$, on the other hand, 2D nuclei are not generated around the middle of the terrace because adatoms are incorporated into the film at the step edges, that is, the growth is step-flow growth. Clear transition from layer-by-layer growth to step-flow growth observed in Figures 2.12(a) and (b) suggest that λ of Al under the current condition is shorter than half the width of the wider terrace ($\sim$250/2 nm) but longer than $\sim$100/2 nm. This surface Al-diffusion mechanism is discussed in more detail below.

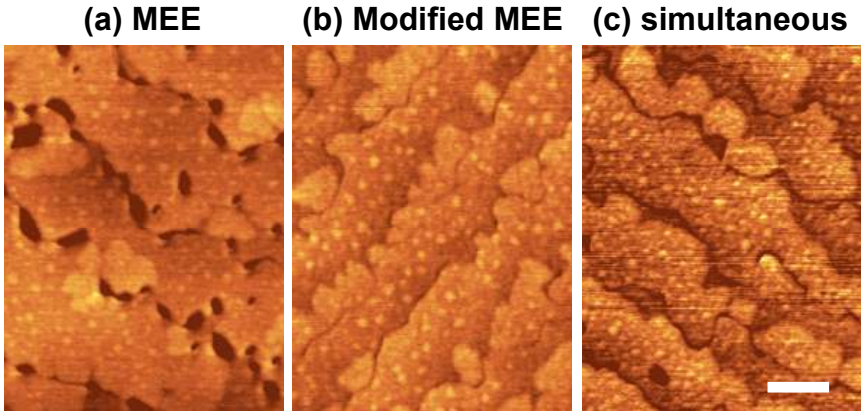

Figure 2.13: AFM images of $\sim$600-nm-thick AlN grown by (a) MEE, (b) modified MEE, and (c) simultaneous supply method. Scale bar represents 200 nm.

2.7 Dependence of Al Migration on Epitaxial Growth Mode

For the case of GaAs, migration enhancement by alternating source supply has evidently been explained [18]. Here, the Al diffusion is compared during

the growth by MEE, modified MEE, and simultaneous source-supply method. Without the inserted simultaneous supply duration in modified MEE, it could yield the MEE process, and thus the degree of migration is expected to be in the order of MEE > modified MEE > simultaneous supply method. Figure 2.13 compares the surface morphologies of AlN layers grown by those three methods on sapphire substrates with a mis-orientation of 0.06 °. The incomplete coalescence observed in MEE-grown AlN is due to the highly 3-D nucleation observed at the initial growth stage, as discussed in Section 2.5. The layer-by-layer growth on the wider-terrace substrates created 2-D nuclei having a diameter of ∼20 nm on all the samples. To quantify the 2-D nuclei found on the surface, the nuclei densities for each method were evaluated to be 1.6 $\times 10^{10}$ /cm^2 for MEE, 1.7 $\times 10^{10}$ /cm^2 for modified MEE, and 3.4 $\times 10^{10}$ /cm^2 for the simultaneous supply method. These values were quite typical when several measurements were taken at different sample area.

Because a lower nuclei density indicates higher diffusivity, those alternating supply of TMA and NH_3 methods indeed enhanced the Al adatom migration. However, no significant difference of nuclei densities was observed between MEE and modified MEE. That is, the degree of Al adatom migration during quasi-homoepitaxy is:

$$\text{Simultaneous} < \text{Modified MEE} \sim \text{MEE}$$

This finding is different from the result on the degree of migration found at the initial stage, where the migration degree was clearly in the order of MEE > modified MEE > simultaneous supply method 2.5. This suggests that the behavior of Al adatoms during (quasi) homoepitaxy is distinctly different from that during the initial nucleation stage (heteroepitaxy). A clear order of migration degree could be observed for the heteroepitaxial (that is, between sapphire and thin AlN layer) growth probably due to the strain and chemical mismatch between AlN and sapphire, while these factors are not applicable anymore during homoepitaxial growth, and hence, no significant surface migration difference was observed between MEE and modified MEE.

Because the mean distance between the nuclei should correspond to twice the diffusion length (λ), λ can be estimated from the evaluated nuclei densities. The average area occupied by a single 2-D nucleus was first obtained as the inverse of the nuclei density,

$$Area_{ave} = \frac{1}{(Nuclei\ Density)}. \tag{2.6}$$

By neglecting the contribution of the step edge, this area can be expressed as $Area_{ave} = \pi\lambda^2$. This assumption is valid when a diffusion length is much shorter than terrace width, as with the current situation. The diffusion lengths were thus estimated to be 44 nm for MEE, 42 nm for modified MEE, and 31 nm for the simultaneous supply method. Although these diffusion lengths could be an overestimations due to the above-mentioned assumption, the diffusion length of 42 nm for modified MEE appears rather reliable because of the reasonable agreement with the coarse estimation based on Figure 2.12. Thus, the nucleation density and the diffusion length is tabulated in Table 2.7.

Table 2.7: Comparison of nucleation density and diffusion length (λ) of Al nuclei during simultaneous, MEE and modified MEE.

Growth Method	MEE	Modified MEE	Simultaneous
Nucleation Density	1.6 $\times 10^{10}$ /cm^2	1.7 $\times 10^{10}$ /cm^2	3.4 $\times 10^{10}$ /cm^2
Diffusion Length,λ	44 nm	42 nm	31 nm

Particularly for the surface of AlN grown by modified MEE [Figure 2.12(a) or 2.13(b)], an area without 2D nuclei near the steps, the so-called denuded zone, can be observed. The width of the denuded zone was measured to be $\sim 50 - 100$ nm, which should equal 2λ and, actually, agrees with the above estimation. Another noteworthy finding is that the denuded zones near the ascending steps were slightly wider than those near the descending steps, which suggested that migrating adatoms are more easily adsorbed at ascending steps. In other words, a barrier for adatoms to approach ascending is lower. This is, unfortunately, not a desirable condition to preserve the 2-D growth as adatoms on existing 2-D nuclei may feel some barrier to descend from the said 2-D nuclei. Hence, the growth condition must be optimized very carefully to achieve high quality AlN layers, as will be discussed in the next chapter.

While it is true that MEE and modified MEE effectively enhanced Al adatom surface migration, for obtaining high quality AlN, we also found it necessary to control the migration degree at the initial nucleation stage in Section 2.5. Too much enhancement of migration causes highly three dimensional ridge structures preferentially located at the sapphire step-edge. This explains nano-pits observed for ~600-nm-thick AlN grown by MEE. On the other hand, the controlled migration by modified MEE during the initial nucleation suppresses this ridge structure thus obtaining a defect-free AlN.

2.8 Summary

In this chapter, simultaneous source-supply, MEE and the developed method called modified MEE were used to grow AlN epilayer. The differences in the epilayer quality was correlated to Al adatom diffusion during initial nucleation stage (heteroepitaxy) and during thick AlN (quasi-homoepitaxy), which is dependent on the underlying surface.

The Al adatom diffusion is found to be distinct during initial nucleation stage and the latter quasi-homoepitaxial growth.

- Initial Nucleation Stage: AlN on Sapphire (Heteroepitaxy)

$$\boxed{\text{Simultaneous} < \text{Modified MEE} < \text{MEE}}$$

- Thick AlN on AlN (Quasi-homoepitaxy)

$$\boxed{\text{Simultaneous} < \text{Modified MEE} \sim \text{MEE}}$$

A clear difference of Al-adatoms migration during the initial nucleation stage led differences in several mechanisms. Owing to the above-differences, among the three methods, modified MEE has obtained superior quality AlN where its growth rate can be written as:

$$\text{Growth Rate: } \text{GR}_{modified\ MEE} = \text{GR}_{Simultaneous} + \text{GR}_{MEE}.$$

References

[1] G. B. Stringfellow, *Organometallic Vapor-phase Epitaxy: Theory and Practice,* Academic Press, London, (1989).

[2] NI Labview, *National Instruments,* www.ni.com/labview.

[3] M. Imura, K. Nakano, T. Kitano, N. Fujimoto, N. Okada, K. Balakrishnan, M. Iwaya, S. Kamiyama, H. Amano, I. Akasaki, K. Shimono, T. Noro, T. Takagi, and A. Bandoh,"Microstructure of Thick AlN Grown on Sapphire by High-Temperature MOVPE," *Phys. Stat. Sol. (a)*, **203**, 1626, (2006).

[4] B. N. Pantha, R. Dahal, N. Nepal, J. Li, J. Y. Lin, H. X. Jiang, Q. S. Paduano, and D. Weyburne, "Correlation Between Optoelectronic and Structural Properties and Epilayer Thickness of AlN," *Appl. Phys. Lett.,* **90**, 241101, (2007).

[5] Y. Taniyasu, M. Kasu, and T. Makimoto, "Radiation Polarization Properties of Free-exciton Emission from AlN (0001) Surface," *Appl. Phys. Lett.,* **90**, 261911, (2007).

[6] Z. Chen, S. Newman, D. Brown, R. Chung, S. Keller, U. K. Mishra, S. P. Denbaars, and S. Nakamura, "High Quality AlN Grown on SiC by Metal Organic Chemical Vapor Deposition," *Appl. Phys. Lett.,* **93**, 191906, (2008).

[7] T. Shibata, K. Asai, S. Sumiya, M. Mouri, M. Tanaka, O. Oda, H. Katsukawa, H. Miyake, and K. Hiramatsu, "High-Quality AlN Epitaxial Films on (0001)-Faced Sapphire and 6H-SiC Substrates," *Phys. Stat. Sol. (c),* **0**, 2023, (2003).

[8] Y. A Xi, K. X. Chen, F. Mont, J. K. Kim, C. Wetzel, E. F. Schubert, W. Liu, X. Li, and J.A. Smart, "Very High Quality AlN Grown on (0001) Sapphire by Metal-organic Vapor Phase Epitaxy," *Appl. Phys. Lett.,* **89**, 103106, (2006).

[9] Y. Horikoshi, M. Kawashima, and H. Yamaguchi, "Low-Temperature Growth of GaAs and AlAs-GaAs Quantum-Well Layers by Modified Molecular Beam Epitaxy," *Jpn. J. Appl. Phys., Part 2,* **25**, L868, (1986).

[10] M. A. Khan, J. N. Kuznia, R. A. Skogman, D. T. Olson, M. Mac Millan, and W. J. Choyke, "Low Pressure Metalorganic Chemical Vapor Deposition of AIN over Sapphire Substrates," *Appl. Phys. Lett.,* **61**, 2539, (1992).

[11] M. A. Khan, J. N. Kuznia, D. T. Olson, T. George and W. T. Pike, "GaN/AlN Digital Alloy Short-period Superlattices by Switched Atomic layer Metalorganic Chemical Vapor Deposition," *Appl. Phys. Lett.*, **63**, 3470, (1993).

[12] J. P. Zhang, H. M. Wang, W. H. Sun, V. Adivarahan, S. Wu, A. Chitnis, C. Q. Chen, M. Shatalov, E. Kuokstis, J. W. Yang and M. A. Khan, "High-Quality AlGaN Layers over Pulsed Atomic-Layer Epitaxy (PALE) Grown AlN Templates for Deep Ultraviolet Light-Emitting Diodes," *J. Elec. Materials,* **32**, 364, (2003).

[13] B. D. Cullity, *Elements of X-ray Diffraction* 2nd ed., Addison-Wesley, (1978).

[14] W.A. Harris, *Electronic Structure and Properties of Solids,* Dover, NY, USA, 174-179, (1980).

[15] M. A. Khan, J. N. Kuznia, D. T. Olson, T. George and W. T. Pike, "GaN/AlN Digital Alloy Short-period Superlattices by Switched Atomic layer Metalorganic Chemical Vapor Deposition," *Appl. Phys. Lett.*, **63**, 3470, (1993).

[16] Z. Chen, R. S. Qhalid Fareed, M. Gaevski, V. Adivarahan, J. W. Yang, and Asif Khan, "Pulse Lateral Epitaxial Overgrowth of Aluminum Nitride on Sapphire Substrates," *Appl. Phys. Lett.,* **89**, 081905, (2006).

[17] R. D. Felice and J. E. Northup, "Energetics of AlN Thin Films on the Al_2O_3 (0001) Surface," *Appl. Phys. Lett.,* **73**, 936, (1998).

[18] K. Horikoshi, M. Kawashima, and H. Yamaguchi, "Migration-Enhanced Epitaxy of GaAs and AlGaAs," *Jpn. J. Appl. Phys.,* **27**, 169, (1988).

Chapter 3

Modified MEE and Characterization of AlN

In chapter 2, the growth of AlN by simultaneous source-supply, migration enhanced epitaxy and the modified MEE were presented. After analyzing each method by comparing the degree of Al adatom migration during initial stage and at thicker AlN, it was concluded the modified MEE controls the migration degree to obtain a superior AlN. In this chapter, the details growth parameters optimization such as growth temperature and flux ratio during modified MEE will be discussed. The structural and optical characterization of modified-MEE-grown AlN will be discussed towards the end of the chapter.

3.1 Modified MEE of AlN

All the AlN epilayers analyzed in the previous chapters were grown at the same growth parameters, except, of course for their growth methods. However, it was not explained how those parameters were achieved. In this section, let us examine each parameter that affects the quality of the epilayer. These are growth temperature and NH_3 flow rates. Other parameters such as total pressure and TMA flow rates, were kept the same.

The influence of these parameters are clearly observable by the changing morphology or structural quality of AlN. To maximize the optimum performance of the material, it is but necessary that it be grown on the best growth conditions.

3.1.1 Sapphire Substrate

Before performing the growth of the epilayer, the as-received sapphire substrate was treated first. Figure 3.1 shows the surface condition of the sapphire substrate before (as received, Figure 3.1a) and after gas etching at 1225 ^{o}C for 10 minutes. The as-received substrate showed scratches on the surface while after thermal etching, terraces appeared on the surface. However, the thermally-etched substrate has pits on the surface due possibly to long etching time. These pits act as nucleation sites during heteroepitaxy.

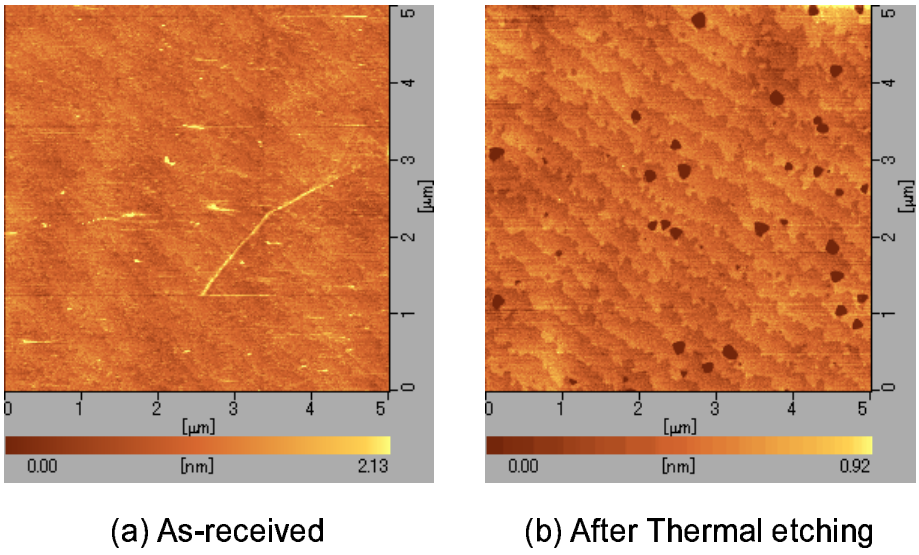

Figure 3.1: AFM image of sapphire substrate: (a) as-received and (b) after thermal etching at 1225 ^{o}C for 10 minutes.

The terrace widths and the step height of the substrate was then measured, as seen in Figure 3.2. The hexagonal sapphire has c-lattice parameter of 1.2991 nm [1], and since there are 6 ML in the unit cell, 1 ML is equivalent to 0.2165 nm/ML. The step height of etched sapphire substrate has ∼0.2143 nm, therefore it is equivalent to 1 ML. On the other hand, the width of the terrace for this substrate was ∼350 nm. As has been discussed in Section 2.6, the step height and terrace width determine the mis-orientation of the substrate.

3.1.2 Optimization of Growth Parameters

Using the same temperature profile used in Chapter 2.3, for the optimization of growth parameters, the growth temperature (T_g) and flux ratio was studied and shown in Table 3.1. The values shown in the table are the

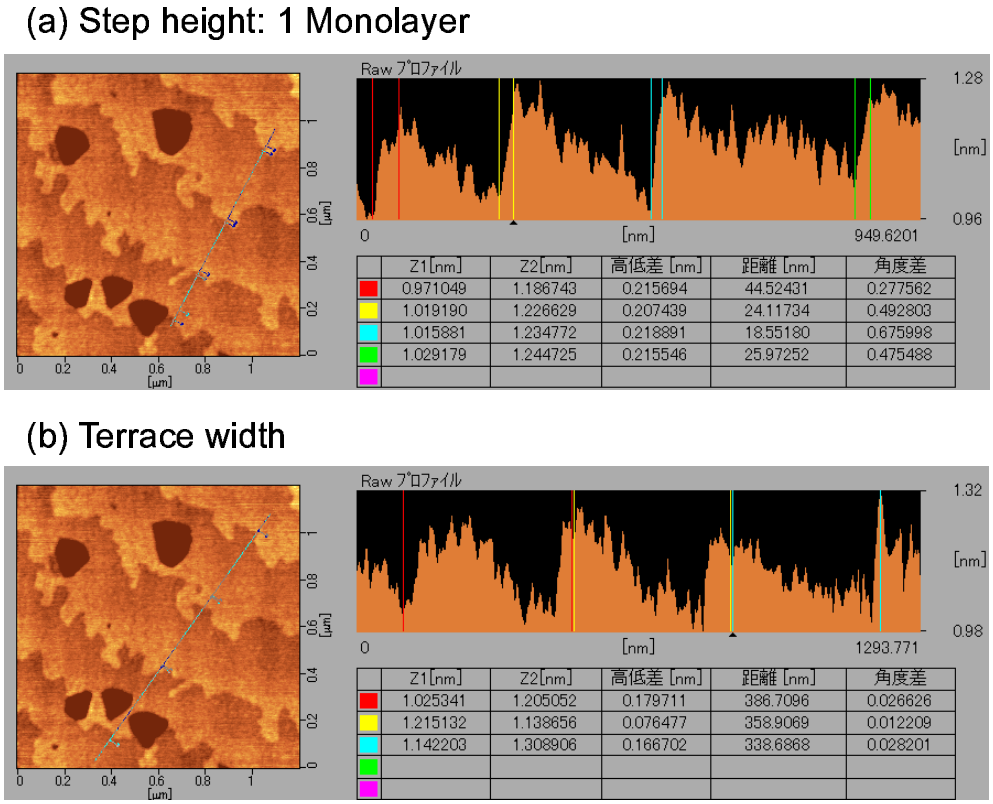

Figure 3.2: (a) The step height of the sapphire substrate is equivalent to 1 monolayer (ML). (b) The terrace on the other hand, has a nominal width of ∼350 nm.

temperature range at which the optimization was performed.

Table 3.1: Optimization of growth conditions for modified MEE of AlN.

Optimization Parameters	Optimized Values
Growth Temperature (T_g)	1190 – 1210 °C
NH_3	490 – 1161 μmol/min
(TMA)	(4.11 μmol/min)

The effect of T_g on the quality of AlN is first discussed. The V/III ratio was 174, which is the optimized value as will be described later below. Figure 3.3 shows the AFM surface morphologies. The morphology changed from rough to atomically smooth when $T_g = 1200$ °C. Further increase of T_g changes the epilayer surface to have pits. These pits are found particularly along the step edge. The surface roughness revealed root-mean-square (RMS) values of 0.16, 0.12, and ∼0.23 nm as the temperature was increased from 1190 to 1210 °C. Moreover, surface quality has been found very sensitive to

growth temperature as a slight change of 5 °C caused significant deterioration of epilayer. This is contrary to a simultaneous source-supply method, which showed no clear dependence of crystalline quality on growth temperatures [2, 3].

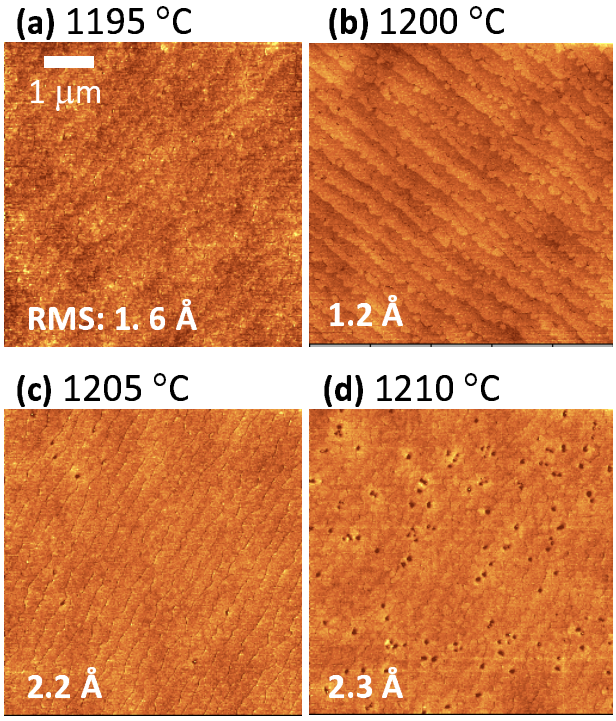

Figure 3.3: Surface AFM images of AlN grown at (a) 1195, (b) 1200 (optimal), (c) 1205, and (d) 1210 °C. The surface is rough at 1195 °C (a), atomically-flat at 1200 °C (b), and with pits above 1205 °C [(c) and (d)]. AlN epilayers were grown using V/III = 174.

It is known that the degree of Al adatom migration is enhanced by the growth temperature. When T_g is low, migration is less active thereby an increased number of nucleation sites promotes surface roughening, as evidenced by AlN grown at T_g = 1195 °C, as shown in Figure 3.3(a). On the other hand, when T_g is above the optimum, though the degree of migration is enhanced, the shorter mean residence time of Al-adatoms and its easy desorption from the surface can promote the generation of pits. This case happened when T_g > 1205 °C (Figures 3.3(c),(d)). At an optimal T_g, the sufficient adatom migration enables to achieve a smooth AlN (3.3b). It is therefore unnecessary to bring T_g of AlN near its sublimation point (2000 °C) just to enhance the migration [4], because further increase of T_g beyond 1200 °C only deteriorates the epilayer quality.

The degradation of surface quality is accompanied by deterioration

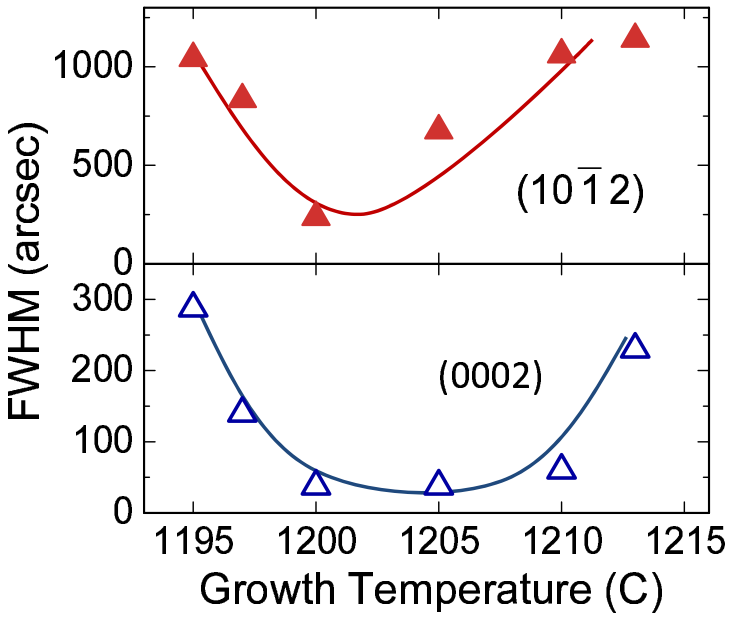

Figure 3.4: Variation of XRD FWHM of symmetric (0002) and asymmetric (10$\bar{1}$2) planes due to T_g. The structural quality is best at T_g = 1200 °C. The epilayers were grown using V/III = 174.

in structural quality as confirmed by high-resolution X-ray Diffraction (HRXRD) measurements. Figure 3.4 shows the full-width at half-maximum (FWHM) of the asymmetric (10$\bar{1}$2) and the symmetric (0002) diffraction. Especially for the asymmetric (10$\bar{1}$2) plane, the quality drastically changed from 1100 to 250 arcsec, and then to 1150 arcsec as T_g is below, at, and above 1200 °C, correspondingly. This is also true for the (0002) plane, but the epilayer quality did not deteriorate as drastically as that in asymmetric (10$\bar{1}$2) plane.

The V/III ratio was also studied by changing the amount NH_3 while keeping the TMA flow rate. Here, T_g was always at the optimized temperature of 1200 °C. It was reported that unwanted trimers and higher n-mers with increasing NH_3 leads to a decrease of growth rate [5]. Though active N species would be readily available when NH_3 flux is in excess, it is necessary to control its amount in order to achieve a flat and high-quality AlN [6], which was demonstrated by the AFM surface images shown in Figure 3.5(a). While a V/III ∼174 has realized a defect-free surface (Figure 3.5(b)), further decreasing the V/III ratio roughened the surface (Figure 3.5(a)). A similar result was also observed in [7]. The insufficient amount of NH_3 led to more available Al adatoms, which remained unreacted due to the less amount of group V sources. Conversely, a greater amount of group V tends to generate

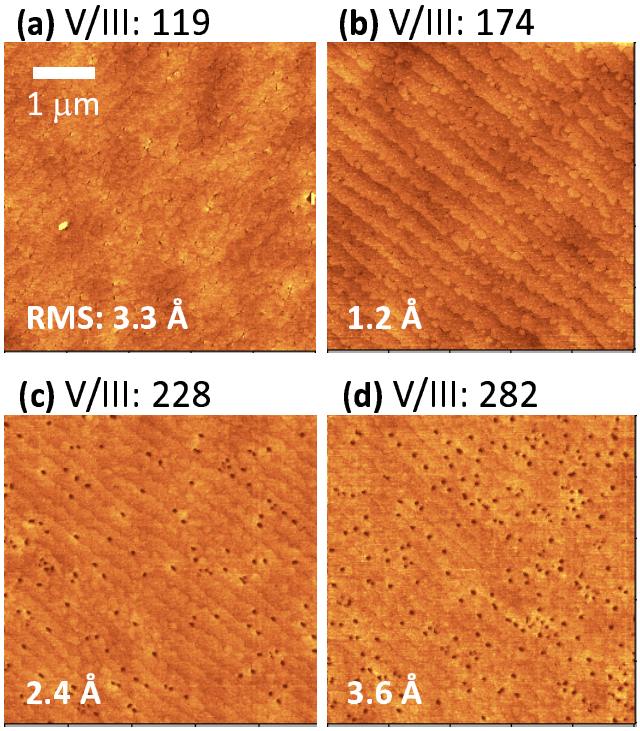

Figure 3.5: Surface AFM images of AlN grown under V/III ratios of (a) 119, (b) 174, (c) 228, and (d) 282. The rough surface with V/III = 119 (a) became atomically flat with V/III = 174 (b), but pits appeared with further increase of the V/III ratio above 228 (c and d). T_g was 1200 °C.

pits along the step-edges (Figure 3.5(c)-(d)). This deterioration in the quality of AlN was further confirmed by the results of symmetric and asymmetric HRXRD as shown in Figure 3.6.

To discuss the mechanism of the observed growth characteristics, it is interesting to compare the surface morphologies displayed in Figures 3.3 and 3.5. Thus, it is found that lower T_g and V/III roughened the surfaces while higher T_g and V/III induced pits. These observations suggest that effective V/III ratio, which is the ratio between the number of Al adatoms and N species that actually contribute to the growth, could be the critical growth parameter. That is, under lower T_g or V/III, the NH_3 decomposition is not sufficient to provide the optimal number of active N species for the AlN growth, while at higher T_g or V/III, excess N species enhance pit formation. Because T_g and V/III are thus related to each other, in order to maintain the optimal number of active N species, higher T_g must be employed when lower V/III is used, and vice versa. A simple optimization model for growing high-quality AlN considering the growth temperature and NH_3 is shown in Figure 3.7.

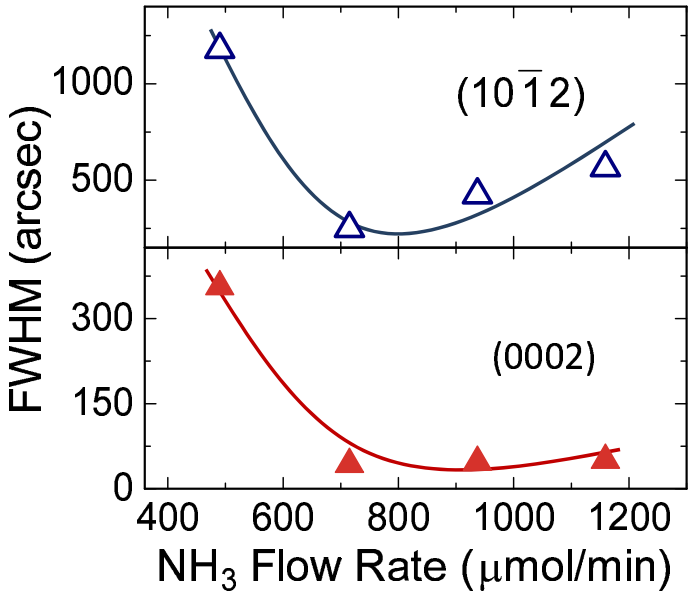

Figure 3.6: Variation of XRD FWHM of symmetric (0002) and asymmetric (10$\bar{1}$2) planes due to T_g. The structural quality is best at T_g = 1200 °C. The epilayers were grown using V/III = 174.

Based on the above observations, the growth process was finally optimized using a growth temperature of 1200 °C and V/III ratio of 174, and an atomically smooth AlN epilayer was successfully achieved as shown in Figures 3.3b or 3.5b. This epilayer has a RMS roughness of 0.12 nm (5×5 μm^2). The FWHM of their (0002) and (10$\bar{1}$2) planes ω-scans were 38.1 and 250 arcsec, respectively.

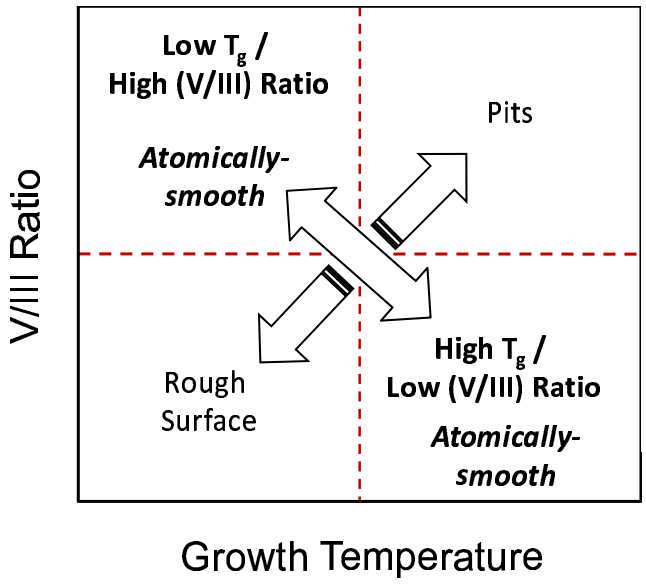

Figure 3.7: Model for Optimizing Growth parameters (T_g and V/III ratio) to obtain high-quality AlN.

3.2 Structural Evolution of AlN

Figures 3.8, 3.9, 3.10, and 3.11 show the sequential structural evolution of AlN grown as per cycle basis by modified MEE. This is in order to understand the growth mechanism especially at the early stages of growth where, as the epilayer gets thicker, dislocation is also generated.

Looking at the AlN epilayer grown for 1 cycle (= 3s), we can see that nucleation started at the step edges and at pits which was originally in the sapphire substrates. The step edge and the those pits are highly-energetic areas therefore adatoms nucleate on those sites. Then 2 cycles later, the terrace is completely covered with nuclei. We can see until 80 growth cycles that those ridges formed at the step edge grow vertically, in fact they are very distinct.

The first coalescence occurred after 81 cycles (∼57 nm), where those tall ridges start to disappear. At this stage, the surface starts to become smoother and a competition between the lateral and vertical growth exists until eventually the vertical growth becomes slower and the lateral growth is promoted. As expected, the number of pits become smaller due to the fact that islands coalesce together with those pits. Then at ∼ 400 nm, the layer-by-layer growth occurs. This mechanism is already explained in Section 2.6.

During the nucleation stage, dislocations start to appear. As dislocation

is the process of releasing the strain in the epilayer by creating dislocation, it is important that the relaxation process happen at a later stage. Among the three methods used, it was found out that the relaxation happens fastest in simultaneous method and almost the same with Modified MEE and MEE. Thus the relaxation is delayed by the alternating suppluy of precursors. Another factor why the surface of modified MEE is free of defects (thus lower dislocation density) is that the very tall ridge structure from MEE could also increase the number of dislocation density. Thus being said, the modified MEE method reduces the dislocation density by delaying the lattice relaxation and reducing the tall ridge structure formed by MEE.

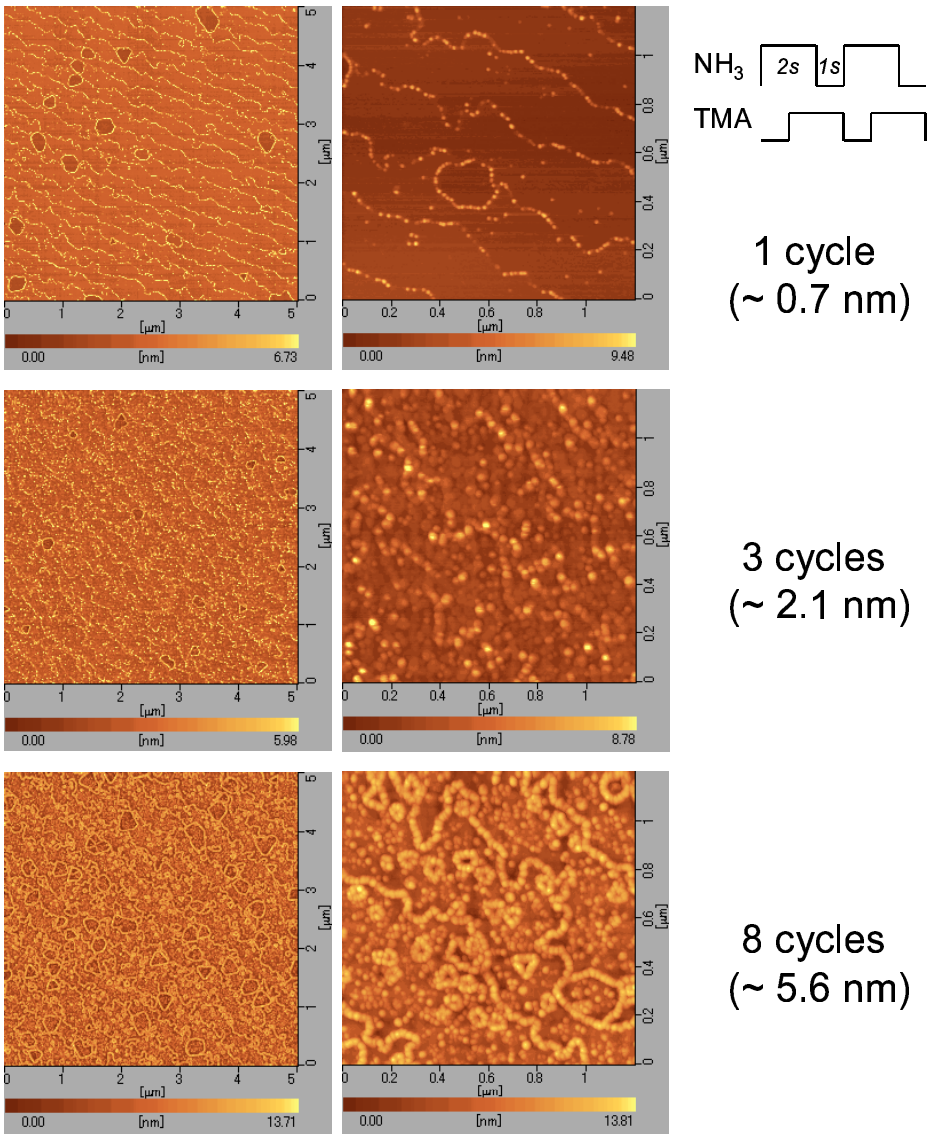

Figure 3.8: AFM images of sructural evolution of AlN fabricated by Modified MEE. AlN epilayers were grown for 1 cycle, 3 cycles and 8 cycles. Left figure scan area: 5 x 5 μm. Right: 1.2 x 1.2 μm

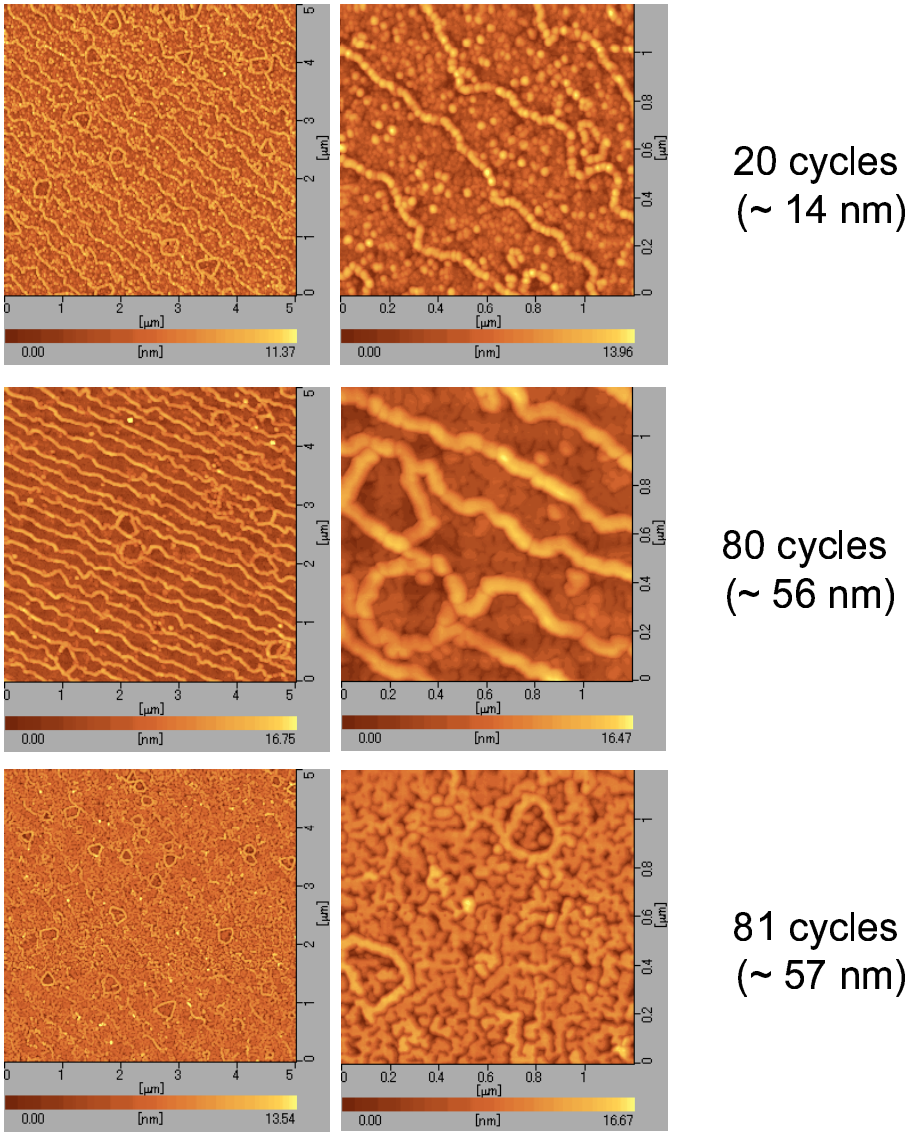

Figure 3.9: AFM images of sructural evolution of AlN fabricated by Modified MEE. AlN epilayers were grown for 20 cycles, 80 cycles and 81 cycles. Left figure scan area: 5 x 5 μm. Right: 1.2 x 1.2 μm

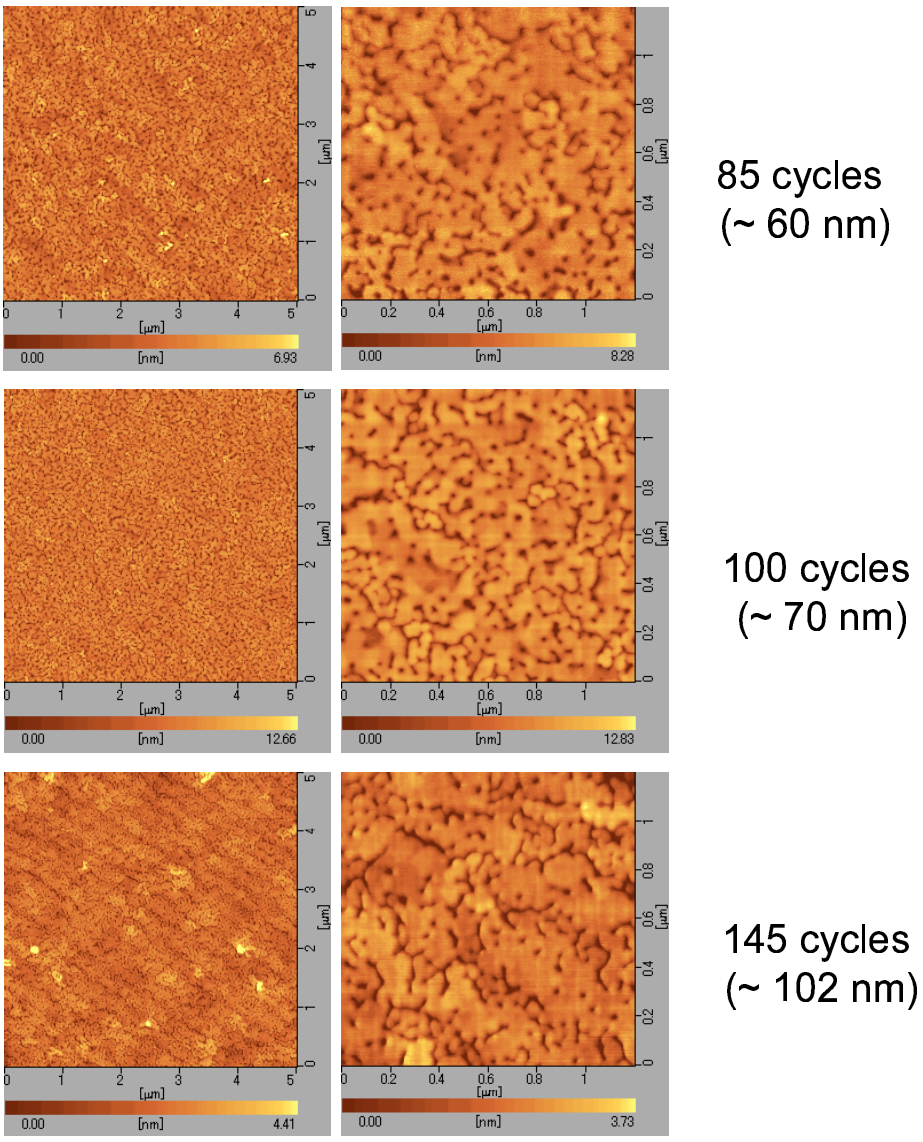

Figure 3.10: AFM images of sructural evolution of AlN fabricated by Modified MEE. AlN epilayers were grown for 85 cycle, 100 cycles and 145 cycles. Left figure scan area: 5 x 5 μm. Right: 1.2 x 1.2 μm

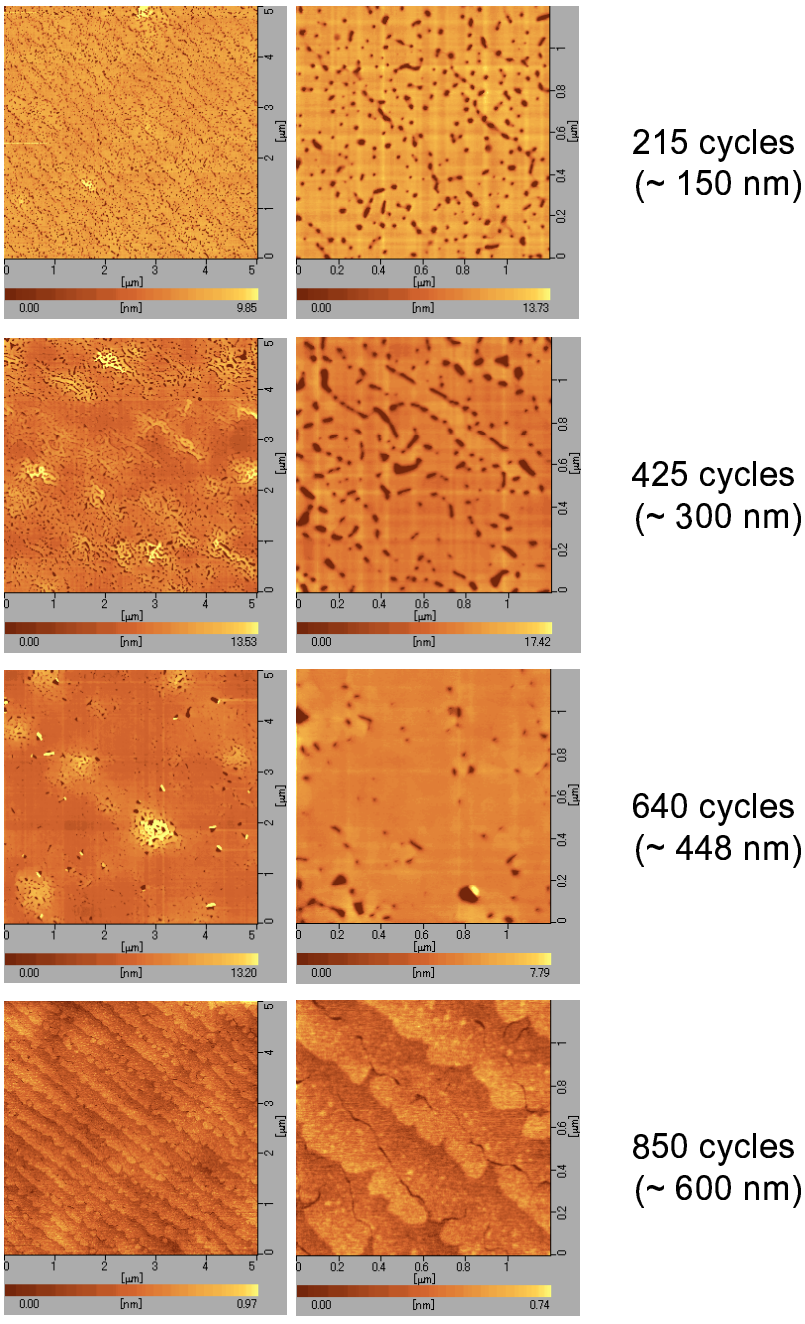

Figure 3.11: AFM images of sructural evolution of AlN fabricated by Modified MEE. AlN epilayers were grown for 215 cycle, 425 cycles and 640 cycles and 850 cycles. Left figure scan area: 5 x 5 μm. Right: 1.2 x 1.2 μm

3.3 Characterization of Modified MEE AlN

3.3.1 Structural properties

From the FWHM of the (0002) diffraction, which corresponds to the tilt component, the screw dislocation density (N_s) was estimated using the Equation 3.1:

$$N_s = \frac{FWHM_{tilt}^2}{4.35|\boldsymbol{b}_s|^2}, \tag{3.1}$$

where, $\boldsymbol{b}_s$ is the Burgers vector equal to <0001> (= 4.9792 Å) [8]. The estimated screw dislocation density is $\sim$4.0 $\times$ 10^6 cm^{-2}.

On the other hand, for the edge dislocation density, the twist component was estimated from the FWHM's of (0002) and (10$\bar{1}$2) diffractions, assuming that the x-ray diffraction profiles were approximated by Gaussian curves and that there was no interaction between tilt and twist [9–11]. Therefore, the FWHM of twist component is estimated from:

$$FWHM_{10\bar{1}2} = \sqrt{(FWHM_{tilt}\cos\chi)^2 + (FWHM_{twist}\sin\chi)^2}, \tag{3.2}$$

where the FWHM$_{tilt}$ is the FWHM of (0002), FWHM$_{10\bar{1}2}$ for (10$\bar{1}$2), and χ is the angle between the (0002) and (10$\bar{1}$2). Therefore the density of randomly distributed edge dislocations (N_e), can be estimated by:

$$N_e = \frac{FWHM_{twist}^2}{4.35|\boldsymbol{b}_a|^2}, \tag{3.3}$$

where $\boldsymbol{b}_e$ is the Burgers vector equal to <11$\bar{2}$0>/3 (= 3.114 Å). Using equation 3.3, and using FWHM$_{tilt}$ = 365 arcsec from the FWHM of (0002) and (10$\bar{1}$2) diffractions, the density of randomly distributed edge dislocations was evaluated to be 7.2 $\times$ 10^8 cm^{-2}.

3.3.2 AlN Polarity

To further investigate the dislocation density, etch pits were revealed by 20 wt% aqueous KOH solution at 70 °C for 10 min. Figure 3.12 shows the scanning electron microscopy (SEM) image of the AlN surface after etching.

Before the SEM measurement, a 1-nm-thick Au film was deposited by sputtering on the surface of etched-AlN to avoid charge-up of incident electrons. Clear hexagonal etch pits were observed, and their density was counted

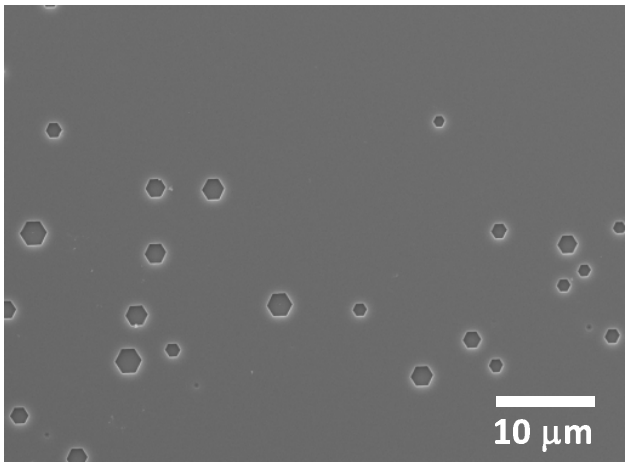

Figure 3.12: SEM image of an AlN surface after chemical etching. Clear hexagonal etch pits can be observed. The etch-pit density is estimated to be 1.0 $\times 10^6$ /cm^2.

to be 1.0 $\times 10^6$ /cm^2. This density agrees fairly well with the dislocation density derived from XRD, thus further confirming the very low dislocation density in the AlN layers.

Another important conclusion emerged from the chemical etching is the polarity of the film. The film thickness was measured before and after etching by an optical interferometer, and it was found that modified-MEE-grown AlN layers did not etched by KOH solution at all. Thus, it is concluded that the film is Al-polar [12, 13].

3.4 Optical Properties of AlN

The interaction of a semiconductor such as AlN with light is of decisive importance for photonic and optoelectronic devices. Here, the optical properties of AlN will be studied by photoluminescence spectroscopy.

3.4.1 Theory

Semiconductors emit light by spontaneous emission when electrons in excited states drop down to a lower level by radiative transitions. This radiative emission is called luminescence. Luminescence can occur by a number of mechanism, but for this case we consider only the photoluminescence - the re-emission of light after absorbing a photon of higher energy. Figure 4.3.2 shows an overview of the main processes that occur when light is emitted from a solid material. Photon is emitted when an electron in an excited

state drops into ground state. For this to be possible, an electron must be injected first which then relax to the state from where the emission occurs. This could be the bottom of the conduction band or could also be a discrete level. The photon cannot be emitted unless the lower level for the transition is empty. This empty lower level is produced by injecting holes into the ground state in a way analogous to injecting an electrons into the excited state.

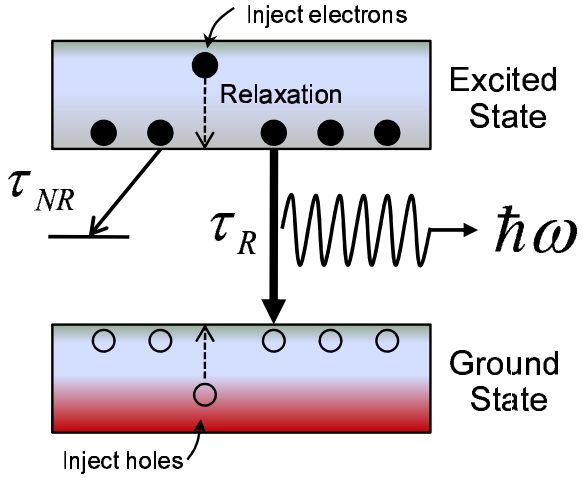

Figure 3.13: Schematic of luminescence in solid. Electrons are injected into the excited state band and relav to the lowest available level dropping to the empty levels in the ground state. These empty levels are generated by injection of holes. The radiative recombination rate is determined by the radiative lifetime τ_R and competes with non-radiative recombination with time constant τ_{NR}.

Statistical physics tells us that atoms in the excited states have a natural tendency to de-excite and lose their excess energy. Therefore the emission of a photon is a spontaneous process and the radiation of light is therefore spontaneous emission. The spontaneous emission rate for radiative transition between two levels is determined by:

$$\left(\frac{dN}{dt}\right)_{radiative} = -AN. \tag{3.4}$$

This shows that the number of photons emitted in a given time is proportional to both the Einstein A coefficient of the transition and the population in the upper level. This rate equation can be solved to give:

$$N(t) = N_o \exp(-At) = N_o \exp(-t/\tau_R). \tag{3.5}$$

The τ_R is the radiative lifetime of the transition and is equal to A^{-1}.

However, radiative emission is not only the mechanism by which the electrons in the excited state goes down to the ground state. Another possible pathway is the non-radiative relaxation. This process can be quantified an electron losing its excitation as heat by emitting phonons or it might transfer its energy to impurities or defects called "traps". The luminescent efficiency, N_R can be calculated by using the rate equation for the population of the excited state when non-radiative processes are possible:

$$\left(\frac{dN}{dt}\right)_{total} = -\frac{N}{\tau_R} - \frac{N}{\tau_{NR}} = -N\left(\frac{1}{\tau_R} + \frac{1}{\tau_{NR}}\right), \tag{3.6}$$

where τ_{NR} is the non-radiative lifetime. Thus, the luminescent efficiency, η_R can be calculated by dividing Equations (3.4) by Equation (3.6), to obtain

$$\eta_R = \frac{1}{1 + \frac{\tau_R}{\tau_{NR}}}. \tag{3.7}$$

Thus, efficient luminescent requires that the radiative lifetime must be shorter than the non-radiative lifetime. Photoluminescence studied therefore are done to extract important physical optical properties of a where in this case AlN.

3.4.2 Experimental Setup

Figure 3.14 shows the photoluminescence set-up used to study the optical properties of AlN. An ArF Excimer laser (λ = 193 nm, pulse width,τ = 4 ns, maximum pulse rate = 300 Hz, from MPB Communications, Inc.) was employed for this experiment. The resolution on the monochromator (1200 grooves/grating) is 0.1 nm (3 meV). The laser power is tuned by film polarizers and $\lambda/2$ wave plate. The sample is placed inside a cryogen-free cryostat where a minimum temperature of 8.5 K can be achieved. The laser is incident from the surface normal and the photoluminescence from the sample is collected at 60° from the surface normal. Before the PL signal goes into the monochromator (Acton Research Corporation SpectraPro300-i) through the slit (opening: 20 μm), it is collimated by one lens and then focused into the entrance slit. The CCD camera attached to this unit cooled by liquid nitrogen.

Wide-range PL spectra of AlN was first obtained both at 8.5 K and at room-temperature (P_{ex} = 360 kW/cm^2) to observe deep-level emission bands.

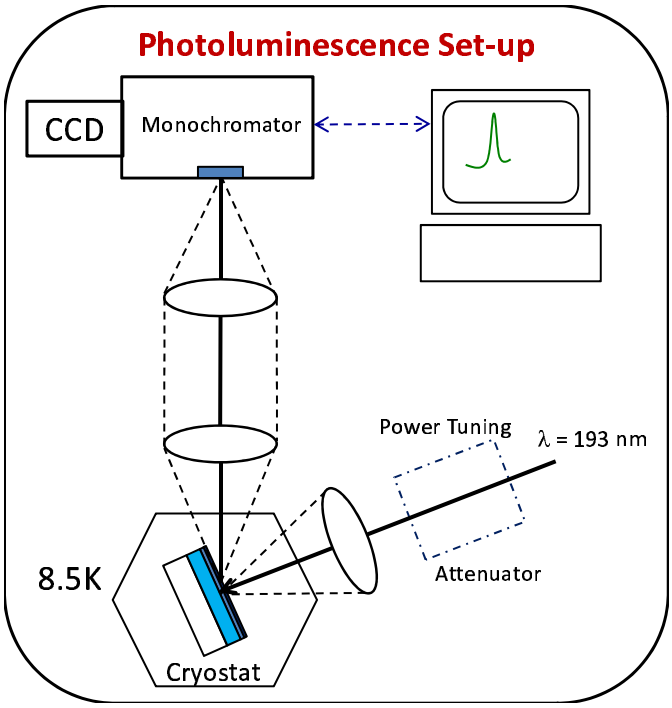

Figure 3.14: Experimental photoluminescence (PL) setup for measuring the radiative properties of AlN.

This spectra is shown in Figure 3.15. A strong near-bane-edge peak (∼6 eV) can be observed on both spectra and the peak position slightly shifted to lower energy with higher temperature. There is no observable prominent peaks at lower energy side which might be related to deep-level emission and pertaining to Al vacancies [14, 15].

A narrow PL region was also evaluated for the highest quality ∼600-nm-thick AlN at 8.5 K with various excitation density. The spectra is shown in Figure 3.16. It can be observed that at low excitation density, only one peak is seen. Upon increasing the excitation density, other peaks start to appear. Considering the spectra excited by laser with a density of 420 kW/cm^2, peak at 6.035 eV and a shoulder peak at 6.0781 eV are observed. These peaks are assigned to the radiative recombination of free excitons ($X_A^{n=1}$) and the radiative recombination of associated with the n=2 excited state of the free excitons ($X_A^{n=2}$) [16–18], respectively. On the basis of the energy separation between the n=1 ground state and n=2 excited state, the binding energy of the free excited is estimated to be 43.2 meV.

Also shown in the figure are two weak peaks at 5.926 eV and 5.8146 eV. These peaks are assigned to longitudinal optical (LO) phonon replicas of the exciton bound to the neutral donors, ($D_o, X_A^{n=1}$-1LO) and ($D_o, X_A^{n=1}$-2LO),

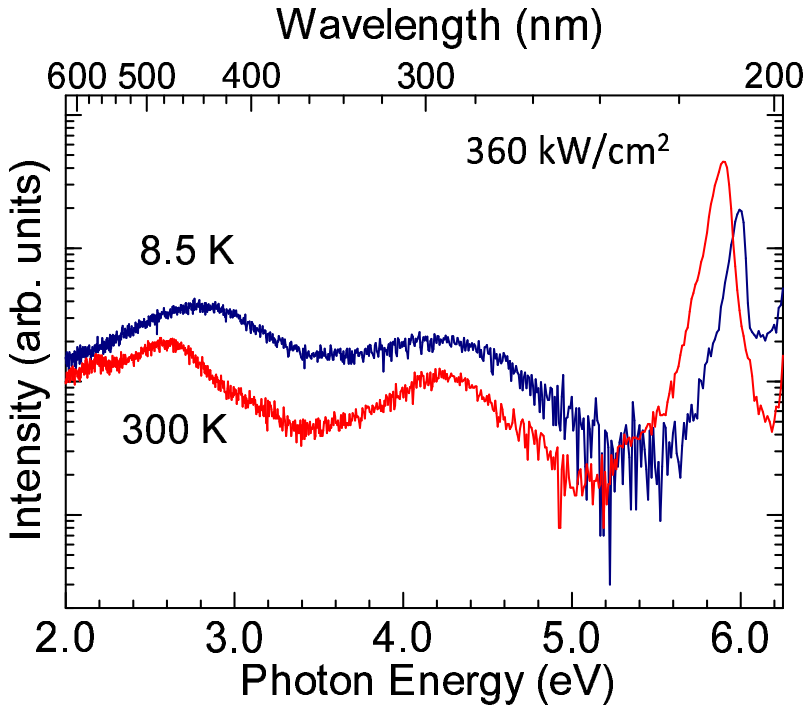

Figure 3.15: The full spectra of AlN taken at 8.5 K and at room-temperature (P_{ex} = 360 kW/cm^2).

respectively. A weak peak is also observed at 5.968 eV which is assigned as the longitudinal phonon replica to $X_A^{n=2}$ ($X_A^{n=2}$-1LO). LO phonon has an energy $\hbar\omega_{ph}$, and the phonon replicas can seen at $E_n = E_o - n\hbar\omega_{ph}$. The energy of the phonon at the Γ point of the Brillouin zone center is 110-111 eV in AlN according to the measurements using infrared and Raman spectroscopy [19, 20]. Deducting from those obtained in this experiment, the LO phonons have energies within the above-mentioned range. Moreover, the linewidth of the prominent near band edge for this sample fabricated by modified MEE is estimated to be around 23 meV obtained from the spectra of the highest excitation density of 420 kW/cm^2, suggesting that the film is uniform and possibly has smaller defect density.

The temperature-dependence PL was also obtained and the activation energy is fitted using this equation:

$$I = \frac{I_o}{1 + A_1 \exp(-E_{a1}/kT) + A_2 \exp(-E_{a2}/kT)}, \tag{3.8}$$

where E_{a1} and E_{a2} are the activation energies of the steep and gentle slope,

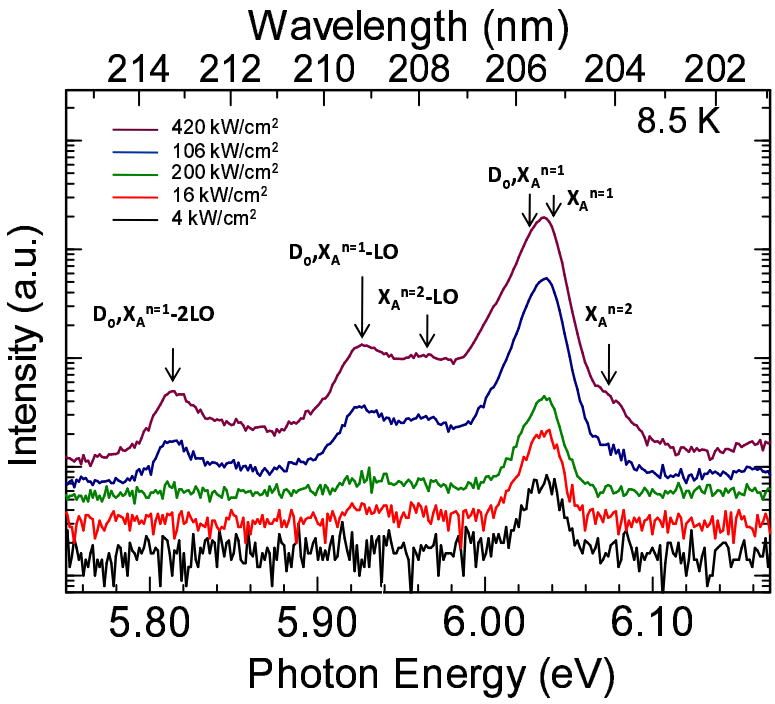

Figure 3.16: Experimental photoluminescence (PL) setup for measuring the radiative properties of AlN.

respectively. E_{a1} corresponds for the activation energy of exciton which was estimated to be about 80 meV while E_{a2} has a value of 2.4 meV.

The ratio of the integrated peak intensity between the room-temperature (290 K) and low-temperature (8.5 K) is 15 %. This is much higher that the result of 0.5% obtained by Jiang et al. [23]. This also suggests the good quality of the epilayer. From the figure, the band gap energy typically decreases with increasing temperature. This is because of the change of electron-phonon interaction and the expansion of the lattice. This temperature dependence can be described with the empirical, three-parameter Varshni formula [24],

$$E_g(T) = E_g(0) - \frac{\alpha T^2}{T + \beta}, \tag{3.9}$$

where $E_g(0)$ is the band gap of AlN at 0 K, α is the volume coefficient of thermal expansion, and β is the volume compressibility. The temperature-dependence of AlN is shown in Figure 3.18 where the α was estimated to be 1.6 meV/K and β to be 1400 K using the Varshni empirical formula marked by the solid line. For the fitting the band gap at 0 K was estimated to be

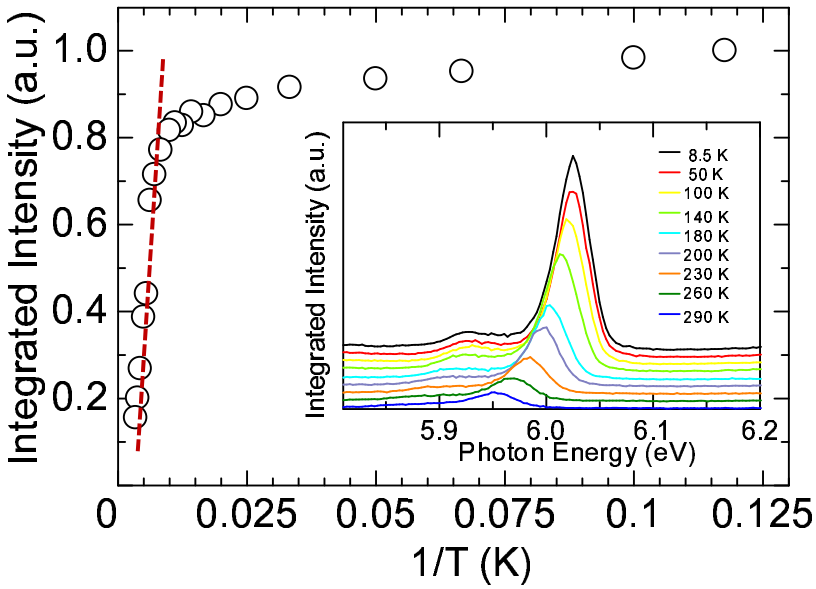

Figure 3.17: Temperature-dependence PL of the dominant peak in AlN. The spectra was fitted and the exciton binding energy was determined. The inset figure shows the temperature-dependence spectra.

6.027 eV. The difference between the experimental value (= 6.024 eV) is 3 meV, which is the binding energy of the donor bound exciton. The estimated values are within the reasonable range from the estimation of other groups.

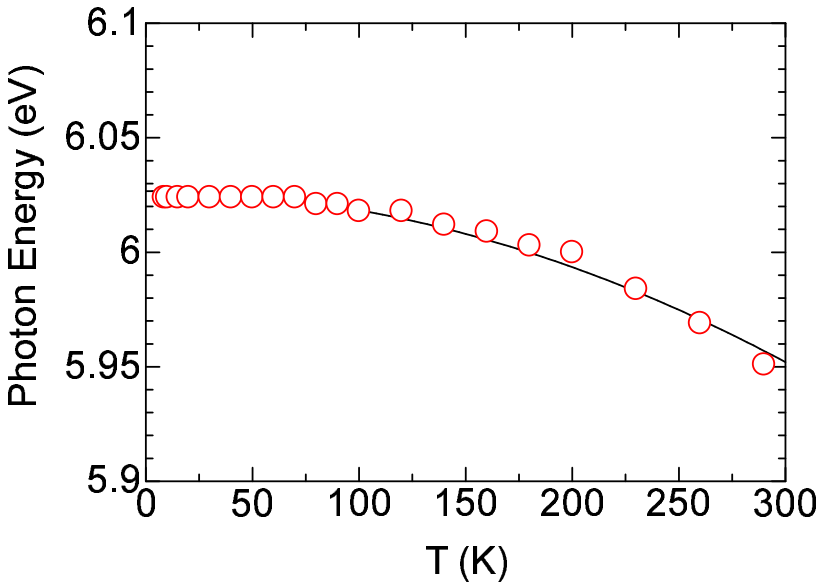

Figure 3.18: Temperature dependence of AlN.

3.5 Perspective

The use of Modified MEE is not only confined to the successful fabrication of AlN epilayer. As will be discussed in Chapter 4, it was also successful in improving the efficiency of the device. In Figure 3.19, it can be seen that Modified MEE also ables to fabricate smooth surfaces of AlN grown under different regimes. In the left figure, the epilayer is grown directly on 6H-SiC without performing any prior treatment. Moreover, clear terraces could be seen if it were grown on the optimized parameter for 6H-SiC. Nevertheless, this is a step closer to achieving smooth and high-quality AlN on SiC. The importance of the use of SiC is due to the fact that it is robust even at high-operating temperatures. Thus is would be a boast for high-power devices.

The middle figure shows the surface morphology of AlGaN grown directly on sapphire substrate. The surface shows a smooth surface as well. This kind of epilayer where a thick AlGaN is growth is desired since the incorporation of Ga in the matrix can be controlled, thus a $Al_xGa_{1-x}N/Al_yGa_{1-y}N$ multiple quantum wells (MQW) can be grown with smaller in-plane lattice mismatch. In return, cracking will be prevented.

The right figure shows that on top of AlGaN, AlGaN/AlN MQWs can also be fabricated. In fact, photoluminescence spectra (not shown) of this sample realized an emission at ∼213 nm. Moreover, the surface also shows

steps - a typical feature of Modified MEE growth method.

All these samples were grown using the optimized growth parameter for sapphire/AlN template. To optimize the radiative property of these distinct materials systems, growth parameters might be suited for each or these systems.

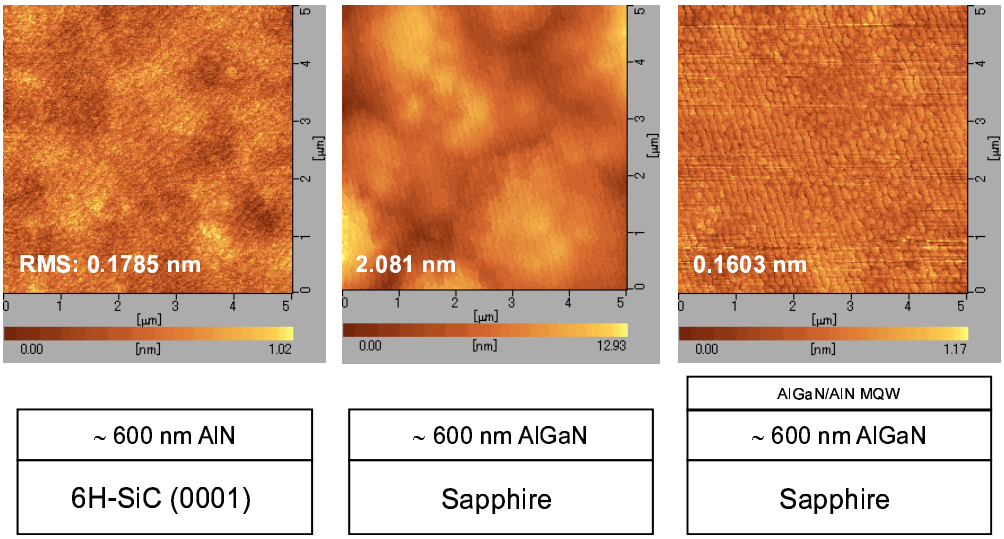

Figure 3.19: The different material systems used to fabricate thick AlN and AlGaN, and AlGaN/AlN MQWs.

3.6 Summary

In this chapter, the optimization of growth parameters namely, growth temperature and flux ratio and the structural and optical properties of modified MEE AlN is discussed. The growth temperature influences the surface and structural quality of AlN. At a growth temperature below the optimum temperature, rough surface morphology and wider FWHM are obtained. On the other hand, surface with pits and wider FWHM are observed when the growth temperature is above the optimum where a defect-free surface and narrow FWHM is obtained. This is summarized in the table below.

Optimization Parameters	Optimized Values
Growth Temperature (T_g)	1200 °C
NH_3/TMA Ratio	715 μmol·min^{-1} / 4.11 μmol·min^{-1}

The quality of AlN was confirmed by Etch-pit density (EPD) test, XRD measurements to estimate the screw and edge dislocation densities, and the

the RT/LT photoluminescence ratio.

Etch-Pit Density (EPD)	Screw Dislocation N_s	Edge Dislocation N_e	PL Ratio (LT/RT)
$\sim 1.0 \times 10^6$ cm^{-2}	$\sim 2.2 \times 10^6$ cm^{-2}	$\sim 7.2 \times 10^8$ cm^{-2}	~ 16 %

References

[1] F. A. Ponce and B. S. Krusor, J. S. Major, Jr., W. E. Plano, and D. F. Welch, "Microstructure of GaN Epitaxy on SiC using AlN Buffer Layers," *Appl. Phys. Lett.,* **67**, 410, (1995).

[2] Y. A. Xi, K. X. Chen, F. Mont, J. K. Kim, C. Wetzel, E. F. Schubert, W. Liu, X. Li, and J. A. Smart, "Very High Quality AlN Grown on (0001) Sapphire by Metal-Organic Vapor Phase Epitaxy," *Appl. Phys. Lett.,* **89**, 103106, (2006).

[3] Y. A. Xi, K. X. Chen, F. Mont, J. K. Kim, E. F. Schubert, C. Wetzel, W. Liu, X. Li, and J. A. Smart, "Optimization of High-Quality AlN Epitaxially Grown on (0001) Sapphire by Metalorganic Vapor-Phase Epitaxy," *J. Elec. Mater.,* **36**, 533, (2007).

[4] Q. Paduano and D. Weyburne, "Two-step Process for the Metalorganic Chemical Vapor Deposition Growth of High Quality AlN Films on Sapphire," *Jpn. J. Appl. Phys.* **42**, 1590, (2003).

[5] T. G. Mihopoulos, V. Gupta, and K. F. Jensen, "A Reaction-Transport Model for AlGaN MOVPE Growth," *J. Cryst. Growth,* **195**, 733, (1998).

[6] V. Lobanova, K. M. Mazaev, R. A. Talalaev, M. Leys, S. Boeykens, K. Cheng, and S. Degroote, "Effect of V/III Ratio in AlN and AlGaN MOVPE," *J. Cryst. Growth,* **287**, 601, (2006).

[7] S. B. Thapa, C. Kirchner, F. Scholz, G. M. Prinz, K. Thonke, R. Sauer, A. Chuvilin, J. Biskupek, U. Kaiser, and D. Hofstetter, "Structural and Spectroscopic Properties of AlN Layers Grown by MOVPE," *J. Cryst. Growth,* **298**, 383, (2007).

[8] T. Metzger, R. Höpler, E. Born, O. Ambacher, M. Stutzmann, R. Stömmer, M. Schuster, H. Göbel, S. Christiansen, M. Albrechit, and H. P. Strunk, "Defect Structure of Epitaxial GaN films Determined by Transmission Electron Microscopy and Triple-axis X-ray Diffractometry," *Philos. Mag. A,* **77**, 1013, (1998).

[9] V. Srikant, J. S. Speck, and D. R. Clarke, "Mosaic Structure in Epitaxial Thin Films Having Large Lattice Mismatch," *J. Appl. Phys.,* **82**, 4286, (1997).

[10] B. N. Pantha, R. Dahal, N. Nepal, J. Li, J. Y. Lin, H. X. Jiang, Q. S. Paduano, and David, Weyburne, "Correlation Between Optoelectronic and Structural Properties and Epilayer thickness of AlN," *Appl. Phys. Lett.,* **90**, 241101, (2007).

[11] S. R. Lee, A. M. West, A. A. Allerman, K. E. Waldrip, D. M. Follstaedt, P.P. Provencio, D. D. Koleske, and C. R. Abernathy, "Effect of Threading Dislocations on the Bragg Peakwidths of GaN, AlGaN and AlN Heterolayers," *Appl. Phys. Lett.,* **86**, 241904, (2005).

[12] D. Zhuang, J. H. Edgar, L. Liu, B. Liu, L. Walker, "Wet Chemical Etching of AlN Single Crystals," *MRS Int. J. Nitride Semicond. Res.,* **7**, 4, (2001).

[13] D. Zhuang, J. H. Edgar, B. Strojek, J. Chaudhuri, Z. Rek, "Defect-Selective Etching of Bulk AlN Single Crystals in Molten KOH/NaOH Eutectic Alloy," *J. Cryst. Growth.,* **262**, 89, (2004).

[14] Y. Shishkin, R. P. Devaty, W. J. Choyke, F. Yun, T. King, and H. Morkoć, "Near Bandedge Cathodoluminescence Studies of AlN Films: Dependence on MBE Growth Conditions," *Phys. Stat. Sol. (a),* **188**, 591, (2001).

[15] T. Koyama, M. Sugawara, T. Hoshi, A. Uedono, J. F. Kaeding, R. Sharma, S. Nakamura, and S. F. Chichibu, "Relation between Al Vacancies and Deep Emission Bands in AlN Epitaxial Films Grown by NH_3-Source Molecular Beam Epitaxy," *Appl. Phys. Lett.,* **90**, 241914, (2007).

[16] E. Silveria, J. A. Frietas, Jr., O. J. Glembocki, G. A. Slack, and L. J. Schowalter, "Excitonic Structure of Bulk AlN from Optical Reflectivity and Cathodoluminescence Measurements," *Phys. Rev. B,* **71**, 041201 (2005).

[17] J. Li, K. B. Nam, M. L. Nakarmi, J. Y. Lin, and H. X. Jiang, "Band-Edge Photoluminescence of AlN Epilayers," *Appl. Phys. Lett.,* **81**, 3365, (2002).

[18] Y. Yamada, K. Choi, S. Shin, and H. Murotani, "Photoluminescence from Highly Excited AlN epilayers," *Appl. Phys. Lett.,* **92**, 131912, (2008).

[19] J. Shi,"Interface Optical-Phonon Modes and Electron Interface-Phonon Interactions in Wurtzite GaN/AlN Quantum Wells," *Phys. Rev. B,* **68**, 165335, (2003).

[20] M. F. MacMillan, R. P. Devaty, and W. J. Choyke, "Infrared Reflectance of Thin Aluminum Nitride Films on Various Substrates," *Appl. Phys. Lett.,* **62**, 750, (1993).

[21] J. Li, K. B. Nam, M. L. Nakarmi, J. Y. Lin, and H.X. Jiang, "Band Structure and Fundamental Optical Transitions in Wurtzite AlN," *Appl. Phys. Lett.,* **83**, 5163, (2003).

[22] K. B. Nam, J. Li, M. L. Nakarmi, J. Y. Lin, and H. X. Jiang, "Unique Optical Properties of AlGaN Alloys and Related Ultraviolet Emitters," *Appl. Phys. Lett.,* **84**, 5264, (2004).

[23] B. N. Pantha, N. Nepal, T. M. Al Tahtamouni, M. L. Nakarmi, J. Li, J. Y. Lin, and H. X. Jiang, "Correlation Between Biaxial Stress and Free Exciton Transition in AlN Epilayers," *Appl. Phys. Lett.,* **91**, 121117, (2007).

[24] Y. Varshni, "Temperature Dependence of the Energy Gap in Semiconductors," *Physica,* **34**, 149, (1967).

Chapter 4

Modified MEE and Characterization of AlGaN/AlN QWs

In this chapter, AlGaN/AlN QWs structure will be fabricated by modified MEE and its structural and optical properties will be discussed in detail. The main application of quantum well structure at present is in electroluminescent devices. It is because QWs allow for obtaining greater range of emission wavelengths, and also enhances the efficiency of devices.

The optical properties in quantum will be probed by photoluminescence spectroscopy and the dependence of peak position and linewidth with temperature and power density will be evaluated.

4.1 Introduction to Quantum Wells

A quantum well is a heterostructure where there is a confinement in only one dimension. This concept was developed by Esaki and Tsu [1]. The QW also forms as the active layer of a device structure therefore its growth has to be controlled to monolayer (ML) precision. A dimensional fluctuation in the active well layer is found to affect the emission efficiency of the device drastically.

Interesting optical phenomenon happens when the effect of quantum confinement is experienced in a crystal. This quantum confinement can be experienced when a heterostructure has a dimension comparable to the mean free path of carriers. Thus a QW layer, which has a thickness of $\sim$200$-$400 Å exhibit quantum size effects. Figure 4.1a shows the device structure having

AlGaN/AlN QW as the active layer. Figure 4.1b shows the three-dimensional schematic of a single QW showing the different bandgaps of AlN and AlGaN creating a discontinuity at the junction.

In the figure, it can be seen that the band gap of AlN is larger than AlGaN. This means that electrons in AlGaN layer are trapped by a potential barriers at each side due to the discontinuity in the conduction band. Similarly, holes are trapped by the discontinuity in the valence band. These barriers allows the states to be quantized in one direction and free to move in the other two directions.

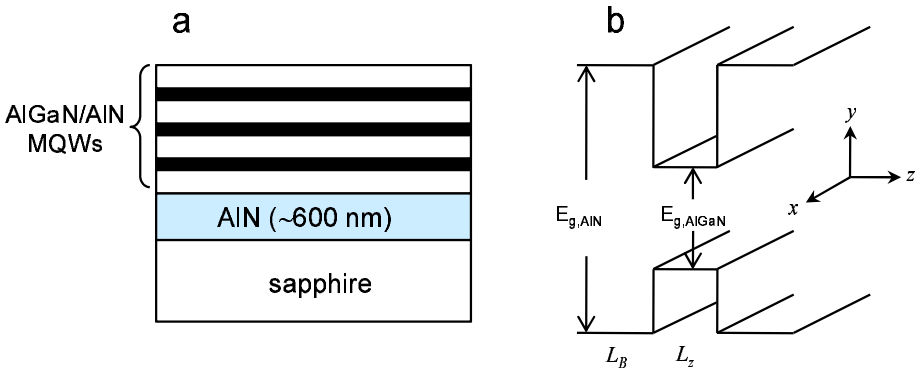

Figure 4.1: (a) Structure AlGaN/AlN QWs grown on AlN/sapphire by Modified MEE. (b) Simples schematic representation of a single QW in three dimension formed by AlN and AlGaN with band gaps $E_{g,AlN}$ and $E_{g,AlGaN}$, respectively. In the x-y plane, the material dimensions have no limits. L_B and L_z represent well and barrier widths, respectively.

Thanks to epitaxial techniques such as MOVPE, it allows for the growth quantum structure down to nanometer scale. Here multiple quantum wells be fabricated using the modified MEE.

4.2 Growth of AlGaN/AlN QWs by Modified MEE

The foremost challenge in AlGaN/AlN QW growth is how to achieve a high-quality layers. The QW layer is normally grown by simultaneous supply of TMA, TMG and NH_3 precursors. Though this method has been used for the growth of AlN (where TMA and NH_3 are supplied simultaneously), this might not be ideal for QW layers. This is because, as discussed in the preceding chapter, the lower migration of Al adatoms may promote island growth instead of layer-by-layer growth. This layer-by-layer growth is neces-

sary because in QW, a flat layer is of utmost importance. Though a number of research groups have focused on the improvement of AlN template, little attention has been given to the improvement of the structural quality of this active layer.

Thus in this study, the growth of the QW structure is fabricated based on modified MEE that was first developed for AlN epilayer growth. The temperature profile and the schematic of fabricating the QW is shown in Figure 4.2. This fabrication technique deviates from the conventional method where a continuous supply of TMA, TMG and NH_3 is employed. For the growth AlGaN by Modified MEE , the additional TMG is supplied together with TMA. For the barrier growth (AlN), only the NH_3 and TMA are supplied - same for growing AlN template layer. Thus, the ∼10-nm-thick AlN barrier layer can be achieved after several cycles of modified MEE. For example, at an optimized growth temperature of AlN where the growth rate is ∼0.70 nm/cycle, the ∼13-nm-thick epilayer requires 21 cycles. For the AlGaN, depending on the desired thickness, the layer can be varied by 1 cycle basis. Thus one advantage of adopting this modified MEE for QW growth is the ability of fabricating the active layer in a per cycle basis.

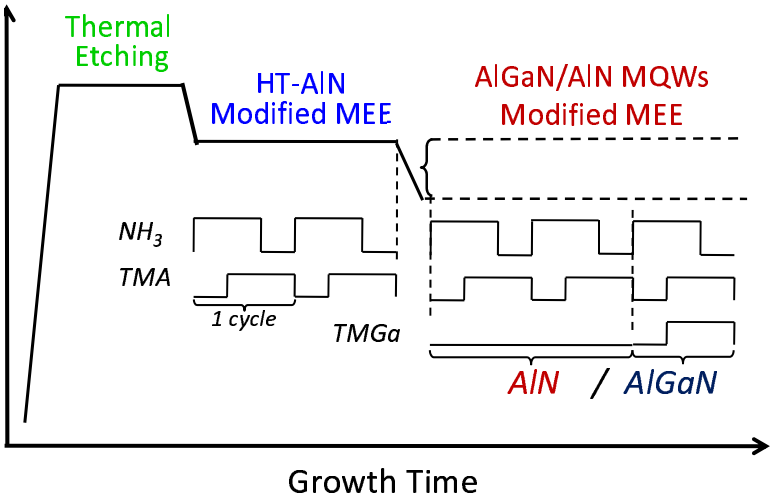

Figure 4.2: The temperature profile used for fabricating AlN epilyer and AlGaN/AlN QWs. Modified MEE growth method is also used for fabricating the QW structure.

The growth conditions used to fabricate ∼600 nm AlN template and the AlGaN/AlN are listed in the Table below (Table 4.1). First, AlN is grown on sapphire substrates. The growth of ∼600 nm AlN template layer was always done at the optimized temperature (for this case, at 1225 °C according to

the thermocouple reading) - the same as growing AlN epilayer (Chapter 3). Afterwards, growth of the QW followed. For $Al_xGa_{1-x}N$/AlN QWs, the growth temperature is either maintained or decreased to up to 1080 °C to increase the Ga incorporation in the matrix. A total of 10 periods of MQW structure was maintained for this study. The well widths were also varied and its optical properties were evaluated.

Table 4.1: Optimization of growth conditions for Modified MEE of AlN epilayer and $Al_xGa_{1-x}N$/AlN QWs. The ∼600 nm AlN epilayer was always grown at the optimized growth temperature while for $Al_xGa_{1-x}N$/AlN QWs, the temperature was varied.

Optimization Parameters	
Growth Temperature (T_g)	
AlN	1225 °C
$Al_xGa_{1-x}N$	1080 – 1225 °C
NH_3	490 – 1161 μmol/min
Sources	
NH_3	893 μmol/min
TMA	4.11 μmol/min
TMG	4.09 - 8.18 μmol/min
Reactor Pressure	76 Torr

4.2.1 Estimation of QW Thickness and Al Composition

Figure 4.3a shows the the XRD pattern of the fabricated device structure shown in Figure 4.1a. The AlN peak can be observed along with the satellite peaks of AlGaN QWs, confirming the successful fabrication of the AlGaN/AlN QW layer. From the XRD pattern, the well and barrier thicknesses were estimated as well as the aluminum composition (x).

In heteroepitaxy, biaxial strain situation arises. For the case of AlGaN/AlN QW growth, since the thickness of AlGaN is small, it is assumed a pseudomorphic growth along the c-axis occurred, then the strain along the c-axis is given by

$$\frac{\Delta a}{a_{GaN}}\left(-2\frac{C_{13}}{C_{33}}\right) = \frac{\Delta c}{c_{GaN}}, \tag{4.1}$$

where C_{33} is the elastic constants of GaN which is equal to 398 (10^{10} Pa), $C_{13} = 106$ (10^{10} Pa), $\Delta c = c_{measured} - c_{AlN}$, and $\Delta a = a_{unknown} - a_{AlN}$. The

$c_{measured}$ is obtained from the (0002) peak of AlN, while c_{AlN} is the bulk which is 4.9792 Å, a_{AlN} is 3.1114 Å. Thus the $a_{unknown}$ can be calculated from the equation above (Equation 4.1).

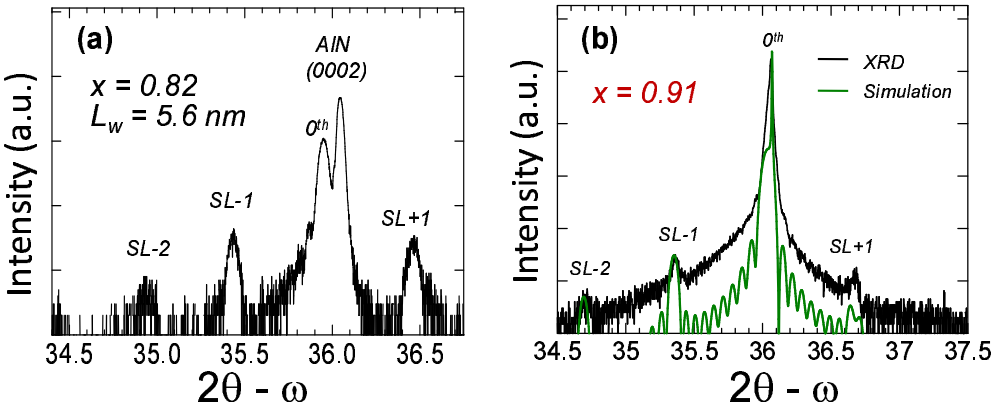

Figure 4.3: (a) The growth of MQWs is confirmed by the satellite peaks of x-ray diffraction (XRD) measurements. From those peaks, well barrier, well widths and Al composition x were estimated. (b) The estimated values fit to that obtained from rocking curve simulation. An example of simulation is seen in this figure for $Al_xGa_{1-x}N$/AlN QWs with $x = 0.91$

After obtaining the a lattice parameter for AlGaN, the lattice spacing is calculated by [2]:

$$d_{hkil} = \frac{a_{unknown}}{\sqrt{\frac{4}{3}(h^2 + hk + k^2) + (\frac{a_{unknown}}{c_{measured}})^2 l^2}}. \tag{4.2}$$

For the case of c-plane (0002) AlGaN, the d_{0002} is easily determined using Equation 4.2. Using this expression

$$L^{total} d^{0th} = L^{AlN} d^{AlN} + L^{AlGaN} d^{AlGaN}, \tag{4.3}$$

the thickness of AlN barrier and AlGaN well can be determined. In order to do that, the d^{0th} has to be estimated from:

$$2d^{0th} \sin\theta^{0th} = \lambda, \tag{4.4}$$

where λ is 1.5406 Å. The θ^{0th} is the fundamental peak of AlGaN QW and can be estimated from the XRD pattern (refer to Figure 4.3a). Then the L^{total} is determined by plotting the satellite peaks with θ where the slope m is equal to $1/(2L^{total})$. Mathematically,

$$\sin\theta_{satellitepeaks} = m(n_{satellitepeaks}). \tag{4.5}$$

Since m (slope) is equal to $1/(2L^{total})$, L^{total} can be easily derived. Moreover, the d^{AlGaN} can be estimated from

$$d^{AlGaN} = x \cdot d^{AlGaN} + (1-x)d^{GaN}, \tag{4.6}$$

where x is the unknown Al composition, d^{AlN} is the lattice spacing of AlN ($=\lambda/2sin\theta$), d^{GaN} is from the coherently-grown GaN on AlN and is given by Eqn. 4.1. Finally, using Eqns. 4.3 and 4.6, the Al (x) composition can be estimated. At a certain Al composition or growth temperature and by varying the well width, the thickness of AlGaN QW can be determined.

Alternatively, the compositional dependence in $Al_xGa_{1-x}N$ can be calculated from the empirical Vegard's law:

$$E_g(x) = xE_g(AlN) + (1-x)E_g(GaN) - bx(1-x), \tag{4.7}$$

where b is the bowing parameter, x is the AlN molar fraction, E_g(GaN) = 3.4 eV, E_g(AlN) = 6.1 eV. The bowing parameter has been estimated by several groups and it showed widely-scattered values [3, 4]. Therefore, instead of estimating the molar composition by using the equation above (Equation 4.7), it was estimated by using the linear relationship of the growth rate and growth temperature for estimating the thickness of AlN and AlGaN barrier and well, respectively, then used the rocking curve simulation software to confirm the estimated values. The result of the calculation agreed very well with the simulation. Figure 4.4 shows the series of $Al_xGa_{1-x}N$/AlN QWs with different molar fraction (x = 0.69 - 0.91) and well widths (up to ∼16 nm) fabricated for this study. On the other hand, the barrier layer has as thickness of ∼14 nm.

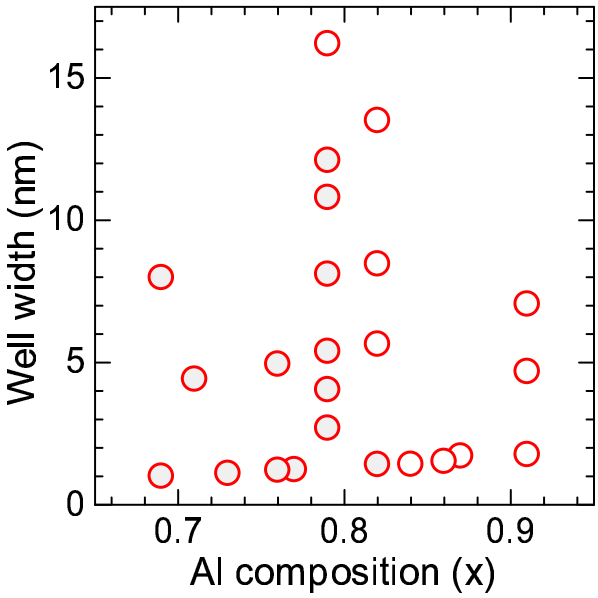

Figure 4.4: $Al_xGa_{1-x}N$/AlN QWs grown at different Al molar fractions and well widths (L_w).

4.3 Structural Qualities of Al-rich $Al_xGa_{1-x}N$/AlN QWs

4.3.1 Reciprocal Space Mapping

Since thick QWs were fabricated, it is necessary to determine whether AlGaN is grown coherently on AlN. Thus, the reciprocal space mapping (RSM) by x-ray diffraction (XRD) was performed using the samples with the thickest well widths. When these thick QWs exhibit coherent growth, then all the thinner QWs also follows as well. Figure 4.5 shows the RSM of $Al_xGa_{1-x}N$/AlN with molar fraction of 0.82 (L_w = 13 nm) and 0.79 L_w=16 nm. Because the $Al_xGa_{1-x}N$ satellites peaks are vertically aligned with the AlN peak, both heterostructures are coherent. Therefore all the $Al_xGa_{1-x}N$ QWs with thickness below these two are also coherent.

4.3.2 Surface Morphology

The surface morphology of the QWs was also studied and the representative AFM images are shown in Figure 4.6 for QWs with different Al molar fraction. As explained in Section 4.2, the incorporation of Ga was by decreasing the growth temperature while all the other growth parameters were the same.

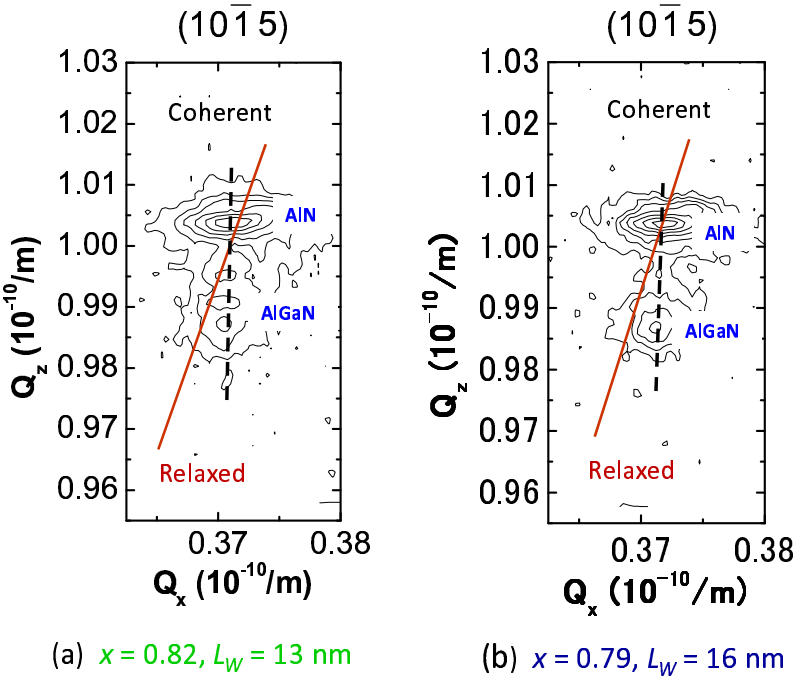

Figure 4.5: Reciprocal space mapping (RSM) of L_w ∼13 and ∼16 nm $Al_xGa_{1-x}N$/AlN QWs.

Since the QW with $x = 0.91$ is grown at the optimized growth temperature of AlN (Figure 4.6), it follows that the atomically-smooth surface of ∼600 nm AlN template is replicated, as clearly seen by the terrace widths.

On the other hand, with decreasing growth temperature, the surface morphology seemed to deteriorate as well. This could be due to the fact that the growth temperature used is clearly not the optimized growth temperature of AlN anymore. This leaves a room for optimization of the growth condition when a low growth temperature is desired.

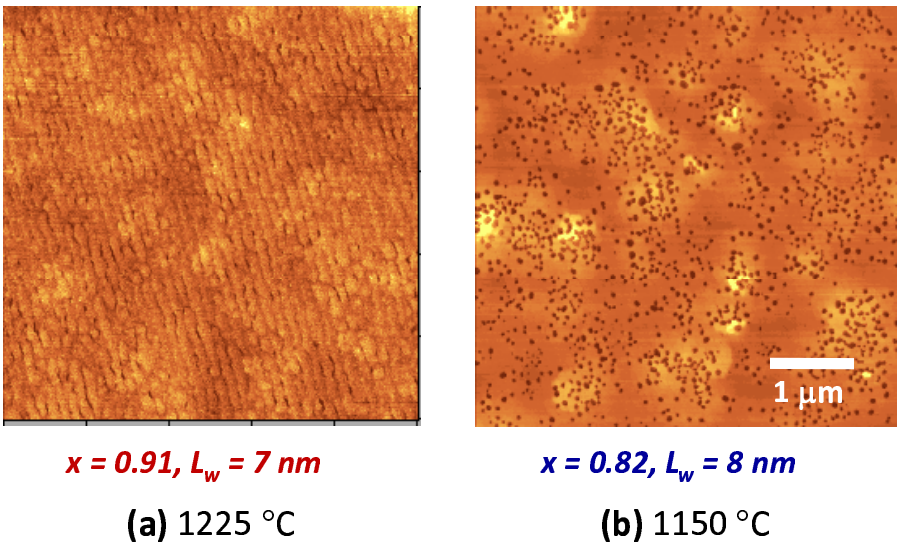

Figure 4.6: Atomic force microscopy surface images of $Al_xGa_{1-x}N$/AlN QWs with (a) $x = 0.91$ and, (b) $x = 0.79$. While a smooth surface is on obtained when using the optimized growth temperature of AlN, the QW grown at lower temperature deteriorates the quality.

4.4 Theoretical Consideration on Optical Properties in $Al_xGa_{1-x}N$/AlN QWs

After the structural characterization of $Al_xGa_{1-x}N$/AlN QWs discussed in Section 4.3, here we will discuss the optical properties in $Al_xGa_{1-x}N$/AlN QWs.

4.4.1 Energy Levels in AlGaN

For group-III nitrides (AlN, GaN and InN), the band energies with strain effects are estimated near the Γ in the Brillouin zone taking into consideration the splitting of the valence band maximum both by spin-orbit interaction (Δ_{so}) and crystal field (Δ_{cr}). Using the $k{\cdot}p$ method with the cubic approximation [5,6], the valence band energies evaluated at $\mathbf{k} = 0$ are given by:

$$E_1^o = \Delta_1 + \Delta_2 + \theta_\varepsilon + \Delta_\varepsilon, \tag{4.8}$$

$$E_2^o = E_v^o + \frac{\Delta_1 - \Delta_2 + \theta_\varepsilon}{2} + \Delta_\varepsilon + \sqrt{\left(\frac{\Delta_1 - \Delta_2 + \theta_\varepsilon}{2}\right)^2 + 2{\Delta_3}^2}, \tag{4.9}$$

$$E_3^o = E_v^o + \frac{\Delta_1 - \Delta_2 + \theta_\varepsilon}{2} + \Delta_\varepsilon - \sqrt{\left(\frac{\Delta_1 - \Delta_2 + \theta_\varepsilon}{2}\right)^2 + 2{\Delta_3}^2}, \tag{4.10}$$

The strain effects Δ_ε are defined as

$$\Delta_\varepsilon = D_1\varepsilon_{zz} + D_2(\varepsilon_{xx} + \varepsilon_{yy}), \tag{4.11}$$

$$\theta_\varepsilon = D_3\varepsilon_{zz} + D_4(\varepsilon_{xx} + \varepsilon_{yy}). \tag{4.12}$$

Since the AlGaN layers are fully-strained and grown along (0001) (c-axis) direction, the strain tensor has this relation:

$$\varepsilon_{xx} = \varepsilon_{yy} = \frac{a_0 - a}{a}, \tag{4.13}$$

$$\varepsilon_{zz} = -2\frac{C_{13}}{C_{33}}\varepsilon_{xx}, \tag{4.14}$$

where a_o and a are the lattice constants of the substrates and the epitaxial layer. The Δ_{so} is the spin-orbit splitting energy, Δ_{cr} is the crystal-field splitting energy, D_i is the deformation potential, C_{ij} is the elastic stiffness constant, and ε_{xx} and ε_{zz} are the strain tensor elements along the x, y and z (c-axis) direction, respectively [5, 6]. The conduction-band edge is taken as

$$E_c^o = E_v^o + \Delta_1 + \Delta_2 + E_g, \tag{4.15}$$

while for AlN, because Δ_1 is negative, the top valence band E_2^o, therefore

$$E_c^o = E_2^o + E_g. \tag{4.16}$$

4.4.2 Internal Electric Field

In the QW, electric field can ionize the excitons by pushing the electrons and holes in opposite direction. The magnitude of the internal electric fields in the well (F_w) and barrier (F_b), can be estimated respectively [7, 8],

$$F_w = \frac{P_b^{SP} + P_w^{PZ} - P_b^{SP} - P_w^{PZ}}{\epsilon_w + \epsilon_b(L_w/L_b)}, \tag{4.17}$$

$$F_b = -\frac{L_w}{L_b}F_w, \tag{4.18}$$

where ϵ is the static dielectric constant, L is the layer thickness and the subscripts b and w represent the barrier and the well, while the superscripts SP and PZ represent the spontaneous and piezolectric polarization, respectively. As seen from Eq. 4.17, the magnitude of the internal field depends on the relative thicknesses of the well and the barrier layers. The strain-induced

piezoelectric polarization can be calculated as

$$P^{PZ} = 2\left(e_{31} - \frac{C_{13}}{C_{33}}e_{33}\right)\epsilon_{\parallel}, \tag{4.19}$$

where e_{ij} is the piezoelectric coefficients and $\epsilon_{\parallel}$ is the in-plane strain equal to ϵ_{xx}. Since the QWs were grown on thick AlN template, the AlN barrier layer is assumed to be relaxed while the AlGaN QWs experience in-plane compressive strain. Hence, the piezoelectric polarization charge in the barrier (P_b^{SP}) is zero while the values of the piezoelectric constants for $Al_xGa_{1-x}N$ used for the calculation is by linear interpolation between the reported values in literature for GaN and AlN [9].

4.4.3 Energy Levels in QW

The energies of the quantized states both in the conduction and valence bands of a QW can be calculated by using Schrödinger equation. The energy level in the QW of thickness L_z (that is, QW with finite thickness for example, along the z direction) can be performed using one-dimensional Schrödinger equation:

$$-\frac{\hbar^2}{2m^*}\frac{\partial^2\psi(z)}{\partial z^2} + V(z)\psi(z) = E\psi(z), \tag{4.20}$$

where m^* denotes the effective mass.

Therefore, the effective transition energy in QWs under the influence of a piezoelectric field is given by [10]

$$E = E_g + \Delta E_e + \Delta E_h - eFL_w. \tag{4.21}$$

where E_g is the band gap of the well material, ΔE_e and ΔE_h are the quantized level for electrons and holes, respectively, and eFL_w is due to the polarization field effect. The shift of $Al_xGa_{1-x}N$/AlN transition energy with well towards higher energy is caused by the internal electric field which spatially separates the electron and hole wave functions with L_w [11]. Figure 4.7 shows the calculated transition energy of $Al_xGa_{1-x}N$/AlN QWs with $x = 0.79$ and 0.91 with L_w, considering the CH transition energy.

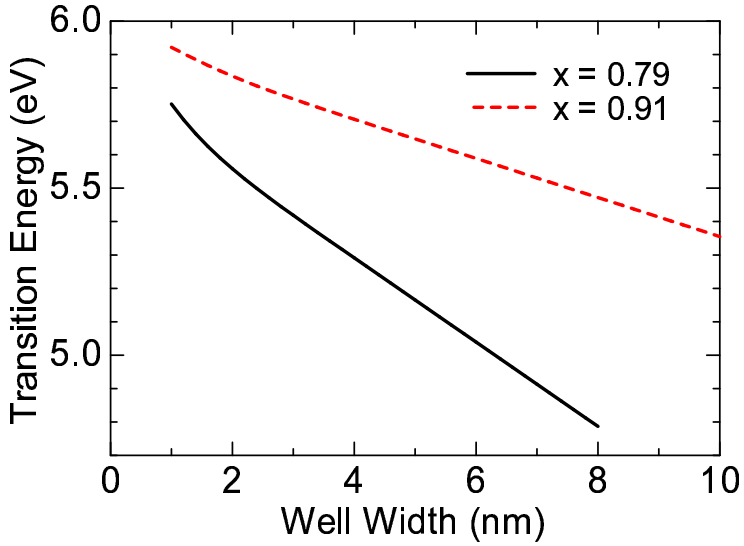

Figure 4.7: The transition energy of CH band in $Al_xGa_{1-x}N$/AlN QWs with $x = 0.79$ and 0.91 showing the effect of internal electric field with the shift of transition energy. The transition energy shifts toward lower energy with L_w.

4.4.4 Derivation of Bohr Radius and Exciton Binding Energy

Semiconductors, like insulators have fundamental absorption edge. This is caused by the onset of optical transition across the fundamental band gap of the material. This naturally leads us to investigate the physical processes that occur when electrons are excited between the bands in the solid by making optical transitions. On the other hand, interband luminescence is the process in which the electrons drop from the excited state bands by emitting photons. The objective in this section is to understand how the luminescence spectrum of AlGaN/AlN QWs is related to its band structure.

When a QW is irradiated by light, the photons are absorbed by exciting electrons from an initial state in the valence band to the final state in the conduction band. However, when an active layer is irradiated by strong light source, excitons are created. Excitons are bound electron-hole pairs held by their mutual Coulomb interaction. Since optical transition can be considered as the creation of an electron-hole pair, the Coulomb attraction increases the optical processes (e.g., absorption rate) because it enhances the probability of forming the electron-hole pair. Therefore the excitonic binding energy in QWs is higher than in the bulk material. The enhancement of excitonic binding energy in the QW is a consequence of the quantum confinement of

the electrons and the holes. This forces them to be closer together than they would be in a bulk semiconductor, ans hence increases the attractive potential.

The state of the exciton binding energy is often calculated using the variational method because of its simplicity. For wurtzite crystal, the variational wave function and the Hamiltonian are anisotropic. Let us then use the variational method in calculating the exciton binding energy Bohr radius [13,14]. The Hamiltonian for an electron-hole pair is given by

$$H = -\frac{\hbar^2}{2m_{r\perp}}\left(\frac{\partial^2}{\partial x^2}+\frac{\partial^2}{\partial y^2}\right)-\frac{\hbar^2}{2m_{r\|}}\frac{\partial^2}{\partial z^2}-\frac{e^2}{\{\varepsilon_\perp\varepsilon_\|(x^2+y^2)+\varepsilon_\perp^2 z^2\}^{1/2}}, \quad (4.22)$$

where $m_{r\perp}$ and $m_{r\|}$ are the reduced mass ($m_r = (m_e^{-1}+m_h^{-1})^{-1}$) respectively perpendicular and parallel to the c direction, m_e and m_h are the effective masses of the electrons and holes, ε is the dielectric constant, and e is the electron energy. The Hamiltonian can be simplified by normalizing the energy and length by

$$E_0 \equiv -13.6(\mathrm{eV}) \times \frac{m_{r\perp}}{m_0}\frac{1}{\varepsilon_{r\perp}\varepsilon_{r\|}}, \quad (4.23)$$

$$a_0 \equiv 0.053(\mathrm{nm}) \times \frac{m_0}{m_{r\perp}}\sqrt{\varepsilon_{r\perp}\varepsilon_{r\|}}, \quad (4.24)$$

which yields,

$$H = -\frac{1}{2}\left[\frac{\partial^2}{\partial x^2}+\frac{\partial^2}{\partial y^2}+\frac{m_{r\perp}}{m_{r\|}}\frac{\partial^2}{\partial z^2}\right]+\frac{2}{\{x^2+y^2+(\varepsilon_{r\perp}/\varepsilon_{r\|})z^2\}^{1/2}}. \quad (4.25)$$

The variational function for the ground state is assumed to be of the form

$$\psi(\mathbf{r}) = \frac{1}{\sqrt{\pi a_\perp^2 a_\|}}\exp\left[-\left(\frac{x^2+y^2}{a_\perp^2}+\frac{z^2}{a_\|^2}\right)^{\frac{1}{2}}\right], \quad (4.26)$$

where $a_\perp$ and $a_\|$ are the variational Bohr radius in the direction perpendicular and parallel to the c-axis, respectively. Introducing this parameter

$$a_\| = a_\perp\sqrt{\left(\frac{\varepsilon_{r\perp}}{\varepsilon_{r\|}}\right)(1+\alpha^2)}. \quad (4.27)$$

$$\omega \equiv \frac{m_{r\perp}\varepsilon_{r\perp}}{m_{r\|}\varepsilon_{r\|}}, \quad (4.28)$$

the exciton binding energy is

$$E_{ex} = \frac{1}{3a_{\perp}^2}\left(2 + \frac{\omega}{1+\alpha^2}\right) - \frac{2}{a_{\perp}a_{\parallel}}\sinh^{-1}\alpha. \tag{4.29}$$

and the corresponding transverse direction exciton Bohr radius is

$$a_{\perp} = \frac{1}{3}\left(2 + \frac{\omega}{1+\alpha^2}\right)\left(\frac{\alpha}{\sinh^{-1}\alpha}\right), \tag{4.30}$$

where

$$\omega = 2\left[\sinh^{-1}\alpha - \frac{\alpha}{(1+\alpha^2)^{1/2}}\right]\left[\frac{\alpha}{(1+\alpha^2)^{3/2}} - \frac{\sinh^{-1}\alpha}{(1+\alpha^2)^2}\right]^{-1}. \tag{4.31}$$

When $\omega \geq 1$, $\sinh^{-1}\alpha$ and $1+\alpha^2$ must be used. On the other hand, when $\omega < 1$, $\sinh^{-1}\alpha$ and $1+\alpha^2$ should be replaced by $\sin^{-1}\alpha$ and $1-\alpha^2$. The strain-dependent effective masses of the heavy hole (HH) and light hole (LH) derived by $k{\cdot}p$ approximation is used [5].

The calculated Bohr radius of the exciton is shown in Figure 4.8 where the radius decreases with increasing Al composition.

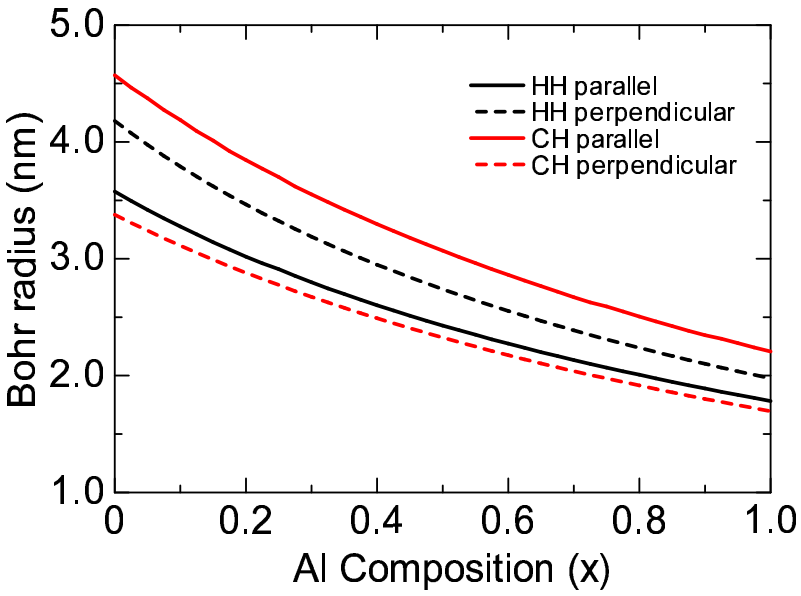

Figure 4.8: The estimated Bohr radius of exciton in $Al_xGa_{1-x}N$ QWs with Al composition (x) where it decreases with increasing x.

Accordingly, the reduction of Bohr radius with Al composition increases

the exciton binding energy (Equation 4.29). Figure 4.9 shows the plot of exciton binding energy with Al composition.

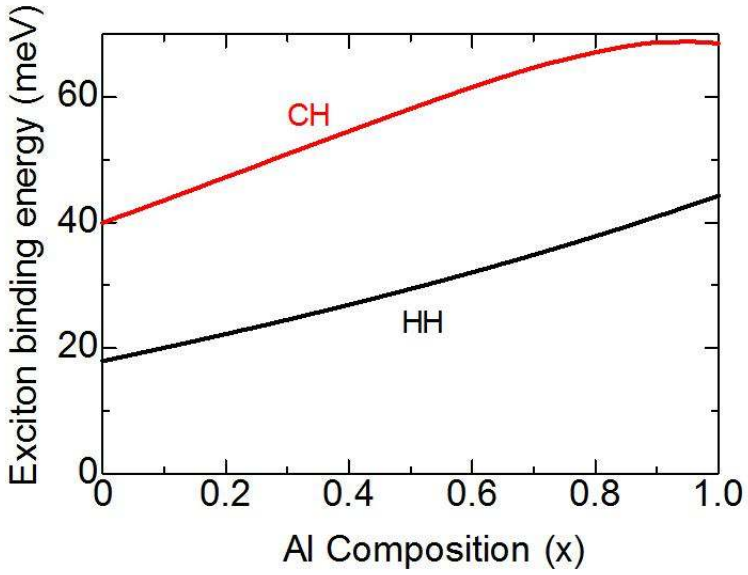

Figure 4.9: The estimated binding energy of the exciton with Al composition in $Al_xGa_{1-x}N$.

4.5 Fundamental PL Properties of $Al_xGa_{1-x}N$/AlN QWs

Let us analyze the optical properties by considering the series of QWs with different Al composition ($x = 0.69 - 0.91$) and with well widths L_z ~1.5 nm. Their normalized PL spectra is shown in Figure 4.10. The PL was obtained using the same PL set-up used for AlN (Chapter 3.14), with an ArF (λ = 193 nm) laser pulse energy density is 5 mJ/cm^2. The result shows that the transition energy changes with Al composition, confirming the successful fabrication of $Al_xGa_{1-x}N$/AlN QW by modified MEE method.

Thus let us then study the dependence of PL intensity with well width using the series of QWs with an Al composition of $x = 0.79$. The plot of the well width with with their corresponding intensities is shown in Figure 4.11a. The intensity depends strongly on L_w. The reason for the rapid reduction of the emission intensity with the increase of L_w can be attributed to the reduction of radiative recombination or quantum efficiency [12] due to the polarization fields in the well and spatial reparation of the holes and electrons

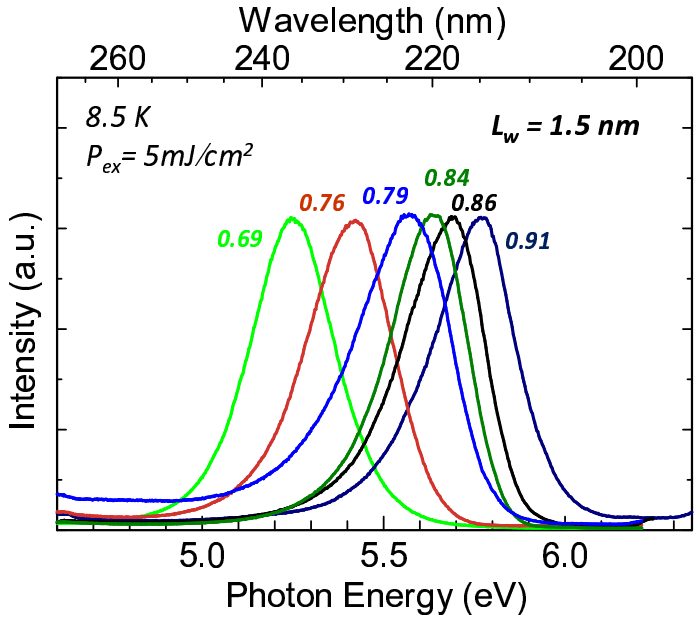

Figure 4.10: PL of $Al_xGa_{1-x}N$/AlN QWs with various Al composition (x = 0.69 - 0.91). The well width (L_w) is ∼1.5 nm.

[7,11]. Figure 4.11b shows the transition energy from PL measurement (circle points) and the theoretical internal electric field at the same Al composition. When the well is small, there is only a slight reduction of transition energy. On the other hand, as the well becomes thicker, the transition energy reduces rapidly. However, the theoretical result of the internal electric field (0.13 MV/cm) shows an underestimation of the actual internal electric field in the QW.

4.5.1 Linewidth Broadening in $Al_xGa_{1-x}N$/AlN QWs

Alloy Broadening

The experimentally-determined full-width at half-maximum of QWs with thicknesses of ∼1.5 nm and ∼5 nm at varying Al composition is shown in Figure 4.12. One notes that the luminescence is very broad where the trend of the linewidth decreases with increasing Al content. This is expected since binary alloys exhibit fairly sharp spectra unlike the case of ternary alloys. In ternary alloy, the random distribution of atoms having different atomic order number (Z) causes significant broadening effect of the luminescence and absorption line. This alloy broadening was first studied in $Al_xGa_{1-x}As$ [15]. This assumes that Al and Ga atoms are distributed randomly on the group-

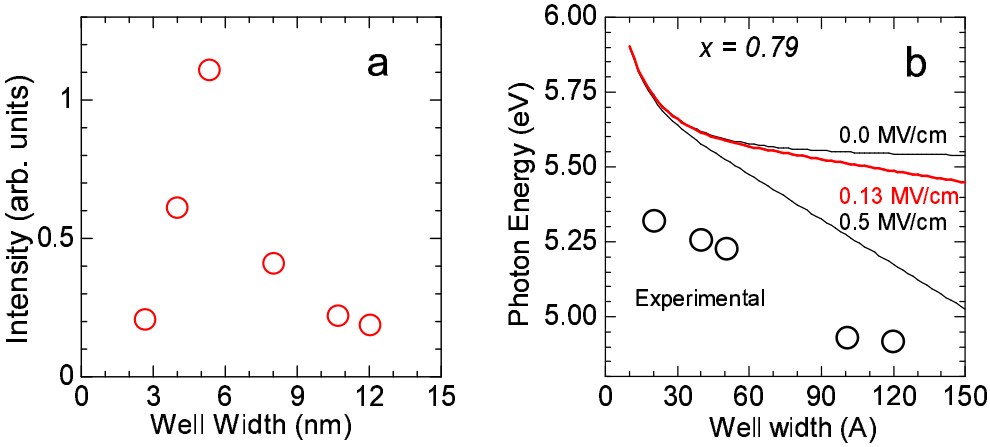

Figure 4.11: (a) Variation of photoluminescence peak intensity with well widths for $Al_{0.79}Ga_{0.21}N$/AlN QWs measured at 8.5 K. (b) The experimental transition energies (cicles) obtained from the same samples compared with the theoretical estimate considering the internal electric field (0.13 MV/cm). The theoretical value is an underestimation of the experimental result.

III sites in an ideal crystal. The probability of finding an Al atom on an any group-III site is given by the alloy composition x. If the experiment averages these random distributions, an inhomogeneously-broadened line is observed.

For the case of $Al_xGa_{1-x}N$, the broadening is caused by a statistical occupation of the cation places Ga by Al and the disorder of the alloy is seen by the exciton. Or conversely, the sampling volume for a luminescence event is the exciton volume that is given by the free-exciton as $V_{exc} = \frac{4}{3}\pi a_{\perp}^2 a_{\parallel}$, where $a_{\perp}$ and $a_{\parallel}$ are the Bohr radius of the exciton Section 4.4.4. In an $Al_xGa_{1-x}N$ alloy, there are on average xc_cV_{exc} Al atoms in the exciton volume. The fluctuation is given by the standard deviation of the binomial distribution

$$\sigma_x^2 = \frac{x(1-x)}{c_cV_{exc}}. \tag{4.32}$$

The corresponding alloy energetic broadening (FWHM) of a spectral line ΔE_{exc} is

$$\Delta E_{exc} = 2.36\frac{\partial E_g}{\partial x}\left[\frac{x(1-x)}{c_cV_{exc}}\right]^{1/2}, \tag{4.33}$$

where $\frac{\partial E_g}{\partial x}$ is the variation of the energy gap with Al composition (x), and c_c is the density of the cations [16]. The theoretical dependence is also seen in Figure 4.12 for heavy-hole (HH) and crystal-field split-off hole (CH) valence sub-bands. The maximum broadening is reached at 80% Al which was considered to be related to the increase of the electron effective mass

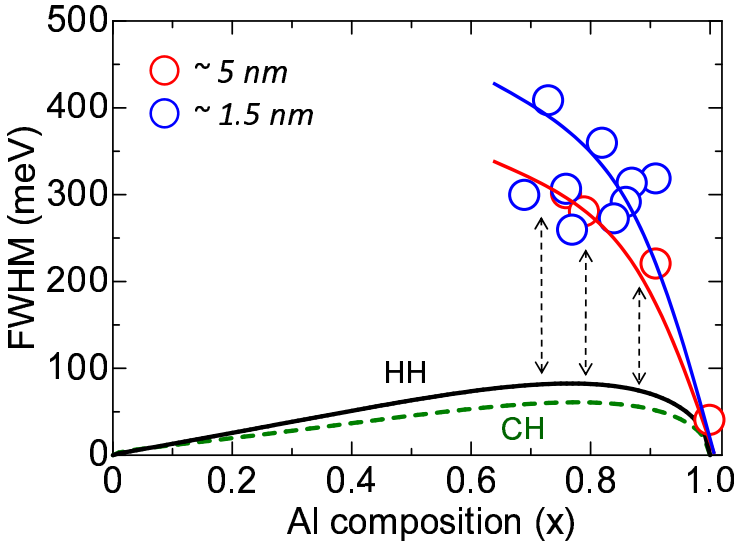

Figure 4.12: The line width of $Al_xGa_{1-x}N$/AlN QWs with varying Al composition (x). The thicknesses of the QWs are ∼1.5 and ∼5 nm.

towards AlN and the decrease of the dielectric constant [16]. This trend has also been reported and the experimental results fitted very well with the calculation [17, 19].

The effect of alloy broadening is felt stronger for thinner QW compared with thick wells as fluctuation becomes drastic when the well thickness is thin. On the other hand, the fluctuation becomes less drastic thus lesser broadening, when the well becomes thick. This can be seen in the figure (Figure 4.12) by comparing the QWs with ∼1.5 and ∼5 nm thickness. However, comparing the theoretical alloy broadening with the experimental results, once sees a large discrepancy which can not be accounted alone by this unavoidable alloy broadening.

Well-width Fluctuations

Another factor that causes linewidth broadening is caused by fluctuations of the well width. As the well width becomes smaller, the effect of well-width fluctuations becomes stronger. Figure 4.13 shows the effect of 1 monolayer fluctuation of the well width with and without considering the electric field [18]. When the well thickness is thin, the effect of 1 ML fluctuation is greater than in thick wells. Moreover, with the presence of internal electric field, the effect increases further.

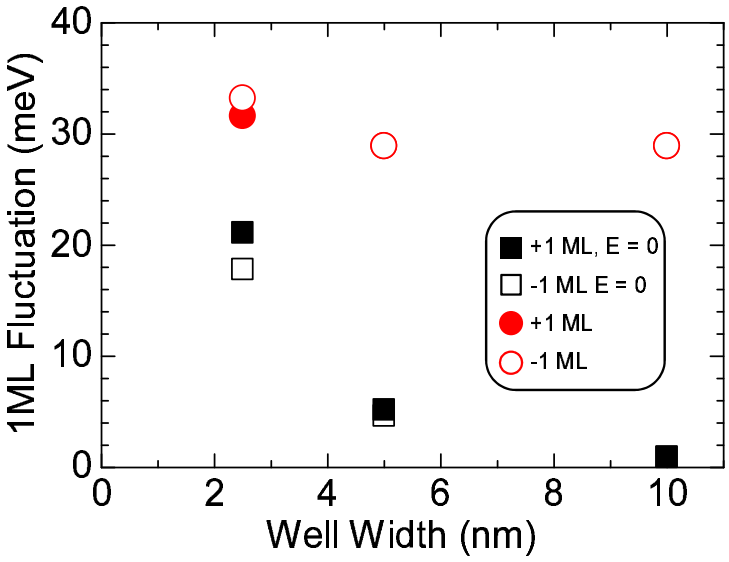

Figure 4.13: The effect of one monolayer (1 ML) fluctuation of well width where it is higher in thin wells. Furthermore, the effect increases with internal electric field.

Figure 4.14 shows the linewidths of $Al_{0.79}Ga_{0.21}N$/Al QWs with different well widths. The linewidth has a decreasing trend with the increasing well thickness. This result is in contrast with that reported [20] in which a linear correlation of the linewidth with well thickness (linewidth increases with well thickness) was observed. This observation was explained by the effects of alloy fluctuation and polarization fields.

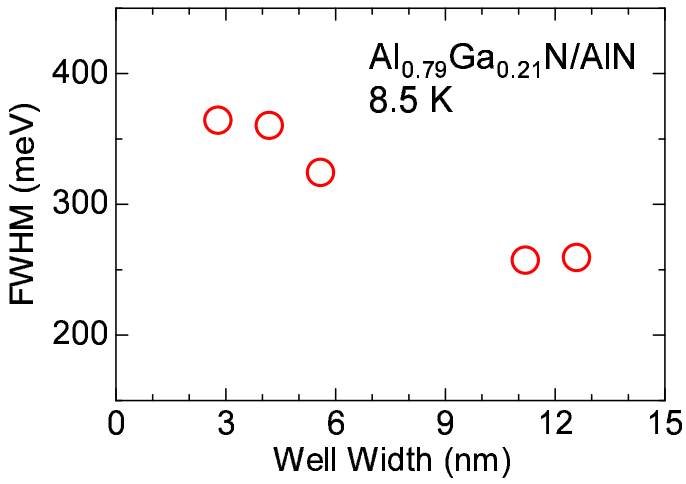

Figure 4.14: The linewidth of $Al_{0.79}Ga_{0.21}N$ QWs with well width. With increasing well width, the linewidth decreases.

4.5.2 Stokes Shift

The luminescence spectra of excitons in QWs are often rather broad and partly Stokes-shifted with respect to the absorption. The reasons for this will be discussed. The theoretical fundamental band gap energy (neglecting the excitonic effect) of the QW with $x = 0.79$, $L_w = 5.2$ nm and $x = 0.91$, $L_w = 6.8$ nm were determined and shown in Table 4.2.

Table 4.2: Comparison between calculated band gap energy without excitonic effect with experimental result of $Al_xGa_{1-x}N$/AlN QWs.

QW (QW)	Calculated band gap (eV)	Experimental (eV)	Δ (meV)
$Al_{0.91}Ga_{0.09}N$/AlN ($L_w = 6.8$ nm)	5.70	5.49	210
$Al_{0.79}Ga_{0.21}N$/AlN ($L_w = 5.2$ nm)	5.31	5.23	90

Figure 4.15 shows the PL spectra of samples tabulated in Table 4.2. The peak of the spectra is the peak energy obtained experimentally. Using the same QW composition and thickness, the calculated band gap without considering the excitonic effect is also shown and the experimental result has lower peak energy position than the calculated result (Stoke's shift).

Exciton Binding Energy

The activation energy of the binding exciton is calculated for QWs samples with different Al compositions and well widths, as tabulated in Table 4.2. The activation energy is estimated from the fitting in Figure 4.16. The activation energy of $x = 0.79$, $L_w \sim 5.2$ nm has higher activation energy than that of $x = 0.91$, $L_w \sim 6.8$ nm. Because of the wider spatial separation of wavefunction in $x = 0.91$, $L_w \sim 6.8$ nm, the activation energy of the exciton is smaller in contrast to that of QW with $x = 0.79$, $L_w \sim 5.2$ nm.

Well-width Fluctuation/Alloy Disorder

Referring to the photoluminescence spectra shown in Figure 4.10 and Figure 4.15, an asymmetric line shape of the PL spectra in the low energy side can be observed, reflecting the low tail of the of localized exciton states. Excitons are also localized in tail states due also to well-width fluctuations/alloy disorder.

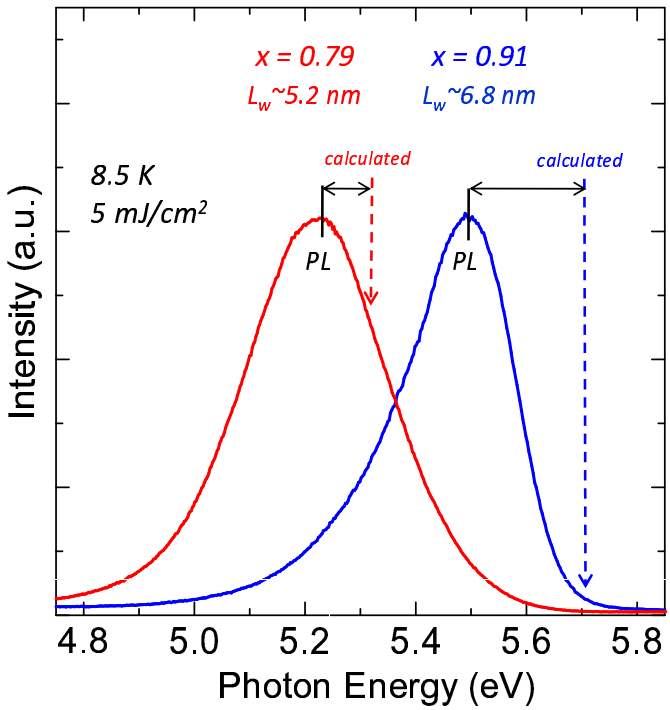

Figure 4.15: Comparison of the theoretical band gap energy with experimentally determined peak energy where a large difference was observed. The $Al_xGa_{1-x}N$ QWs has Al = 0.79 (∼5.2 nm) and 0.91 (∼6.8 nm).

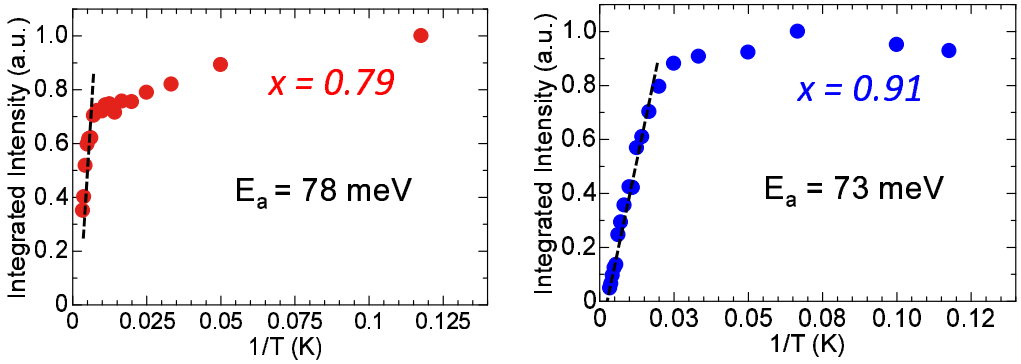

Figure 4.16: The estimated exciton activation energy for $Al_xGa_{1-x}N$ QWs with Al = 0.79 (∼5.2 nm) and 0.91 (∼6.8 nm).

4.6 Temperature-Dependence PL of AlGaN/AlN MQWs

In this section, we wish to study the effects of temperature with respect to the position shift of the transition energy of a QW. From the ratio of the integrated emission intensity between room-temperature and low-temperature, the internal quantum efficiency can also be estimated. The activation energy of the exciton can also be determined from the plot of integrated intensity with temperature.

The samples to be measured are $Al_xGa_{1-x}N$/AlN QWs with various Al compositions and well widths:

1. $x = 0.91$, $L_w = 1.7$ nm, 6.8 nm

2. $x = 0.82$, $L_w = 1.4$ nm

3. $x = 0.79$, $L_w = 2.6$ nm, 5.2 nm, 10.4 nm.

4.6.1 Emission Efficiency of AlGaN/AlN QWs

Figure 4.17 shows the PL spectra of the sample with the most intense emission - a QW with an Al composition of $x = 0.79$ and $L_w \sim 5$ nm.

The ratio of the integrated PL intensity at room-temperature (I_{RT}) and low-temperature (I_{LT}), $\eta = I_{RT}/I_{LT}$ was obtained for those samples listed above, and the result is shown in Figure 4.18 below. The highest η of 36% was obtained for samples with $x = 0.79$, and $L_w = 5.2$ nm. On the other hand, η seems to decrease with increasing Al composition.

The ratio of the integrated peak intensities between low-temperature and high-temperature is related to the internal quantum efficiency η_{int}. This can be expressed as

$$\eta_{int} = \frac{\tau_r^{-1}}{\tau_r^{-1} + \tau_{nr}^{-1}} = \frac{1}{1 + \tau_r/\tau_{nr}}. \tag{4.34}$$

where τ_r^{-1} is the radiative lifetime of the transition and τ_{nr}^{-1} is the non-radiative lifetime. The τ_r^{-1} is related to the overlap wavefunctions of the electrons and holes, $\tau_r^{-1} \propto |< \psi_e \mid \psi_h >|^2$. The overlap function is highest when radiative lifetime is smallest, and is achieved in QW with $x = 0.79$ and $L_z = 5.2$ nm.

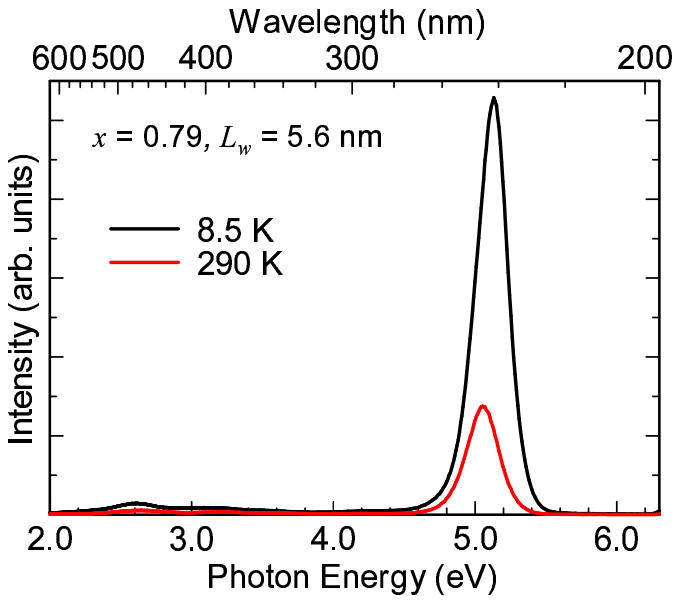

Figure 4.17: Wide-range Photoluminescence spectra of $Al_{0.79}Ga_{0.21}N$/AlN QW with well width of ∼5 nm. The spectra were taken at 8.5 K and 290 K.

4.6.2 Excitation Power Dependence of PL

The dependence of PL intensity with temperature was performed using $Al_{0.79}Ga_{0.21}N$/AlN with (a) L_z = 2.6 nm, (b) 5.2 nm and (c) 10.4 nm. The result is shown in Figure 4.19. From these results, η was estimated accordingly (Section 4.6.1) and the highest η was achieved from QW with L_z = 2.6 nm. The inset figures show that photon energy shifts to lower energy with increasing temperature.

Figure 4.20 shows the temperature dependence of PL linewidth for QWs with x = 0.79 and 0.91. One observes that both samples have broad linewidths even at low temperature. The temperature-dependent broadening phenomena of the exciton linewidth is generally due to exciton-acoustic phonon and exciton-optical phonon interactions expressed as [21]

$$\Gamma(T) = \Gamma_0 + \gamma_A T + \frac{\Gamma_{LO}}{\exp\left[\hbar\omega_{LO}/k_B T\right] - 1}, \tag{4.35}$$

where Γ_0 is the temperature-independent inhomogeneous linewidth. The second and the third terms are the contribution of the exciton-acoustic phonon and the exciton-longitudinal optical (LO) phonon interactions, respectively. γ_A is the exciton-acoustic phonon coupling constant while Γ_{LO} represent the

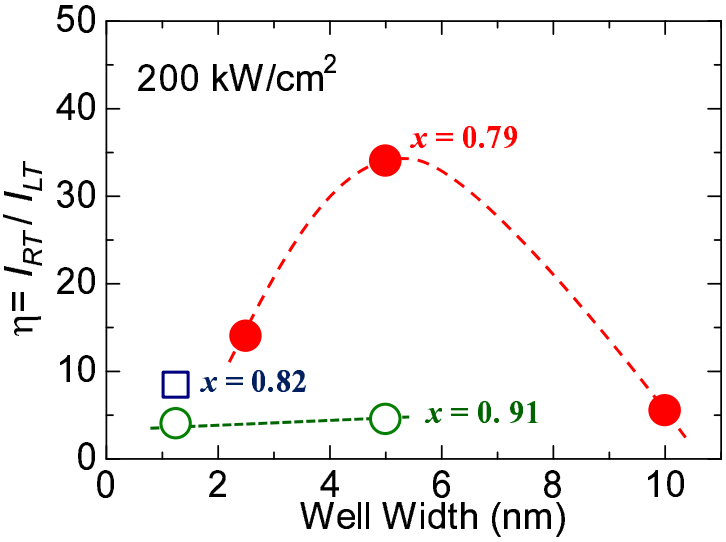

Figure 4.18: Plot of the ratio of room-temperature and low-temperature PL for $Al_xGa_{1-x}N$/AlN QWs with various Al compositions and well widths.

strength of exciton-LO phonon coupling. This temperature-dependent broadening phenomena almost not depicted in the experimental data especially for $x = 0.79$ QW. As explained in Section 4.5.2. As such, the broad linewidth is the effect of excitons being localized in tail states due to well-width fluctuations and/or alloy disorder.

Figure 4.21 shows the dependence of the photon energy with temperature of the $Al_xGa_{1-x}N$ alloys. To evaluate the temperature dependence of the exciton transition energy, least-squares fitting was performed using the Varshni equation (Equation 4.36).

$$E_g(T) = E_g(0) - \frac{\alpha T^2}{T + \beta}, \tag{4.36}$$

where $E(0)$ is the transition energy of the exciton at 0 K while α and β are the Varshni coefficients. The solid line is result of the fitting for $Al_xGa_{1-x}N$ with $x = 0.79$ and 0.91 Al. The result of the fitting is shown in the table below (Table 4.3). It can be observed that the exciton localization energy increases with Al composition.

Looking at Figure 4.21, the estimated exciton localization binding energy is small which signifies the existence of weaker localization in the QW. On the other hand, it was reported that larger localization binding energy makes the film to have low conductivity which is a fact well-known for Al-rich AlGaN

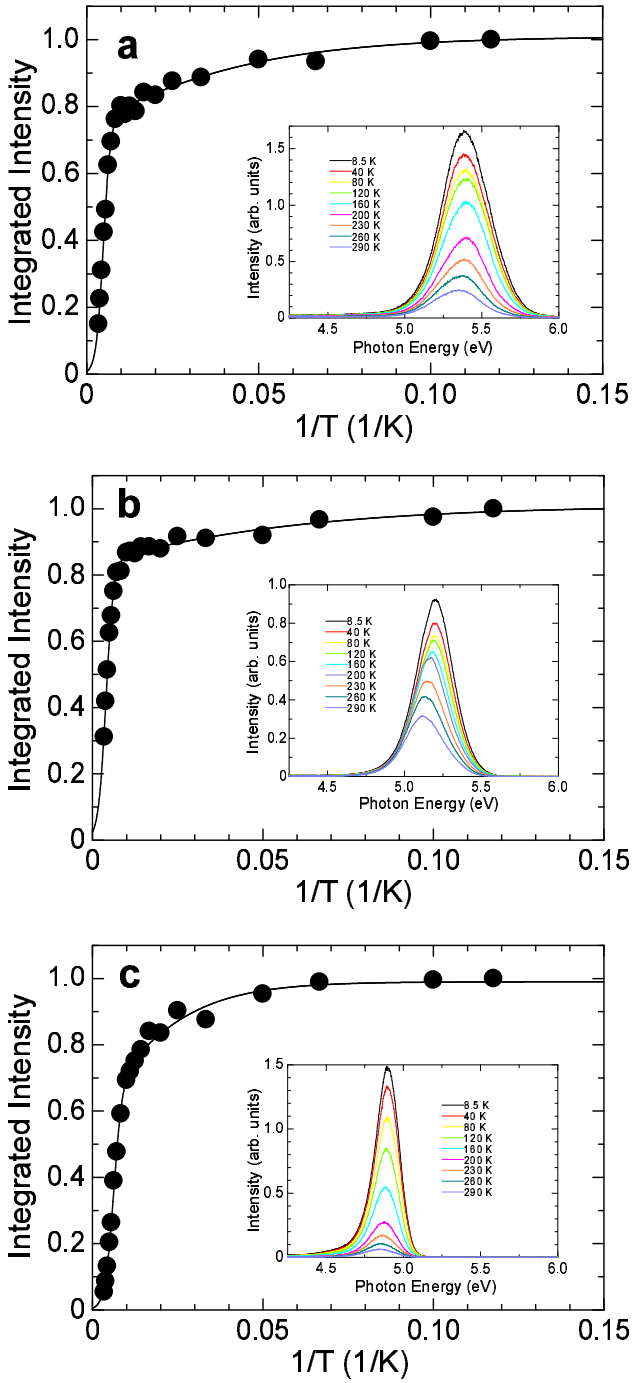

Figure 4.19: Arrhenius plot of integrated PL of $Al_{0.79}Ga_{0.21}N$/AlN QWs with L_z of (a) 2.6 nm, (b) 5.2 nm and (c) 10.4 nm. Inset figure shows their corresponding PL spectra.

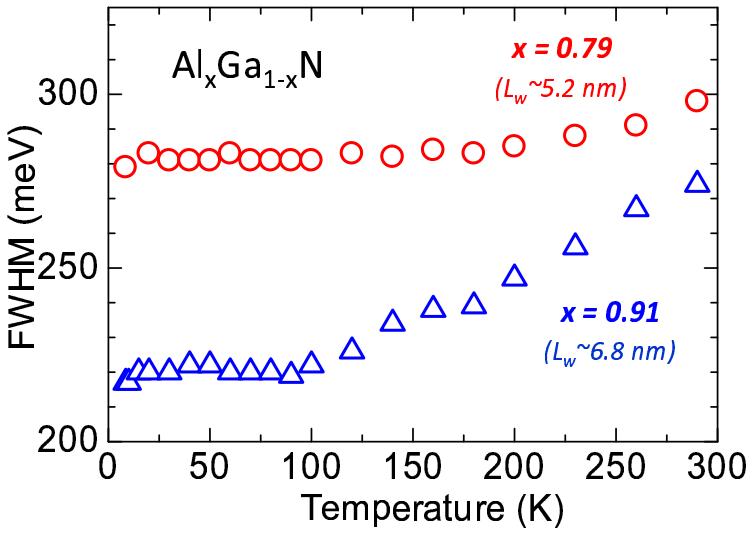

Figure 4.20: Temperature-dependence PL linewidths of $Al_xGa_{1-x}N$ with x = 0.79 and 0.91.

Table 4.3: The estimated binding energy of exciton for $Al_xGa_{1-x}N$ with x = 0.79 and 0.91 Al.

$Al_xGa_{1-x}N$/AlN	α (meV/K)	β (K)	Δ E
0.91	1.8	1400	20 meV
0.79	1.4	1000	10 meV

alloys [22].

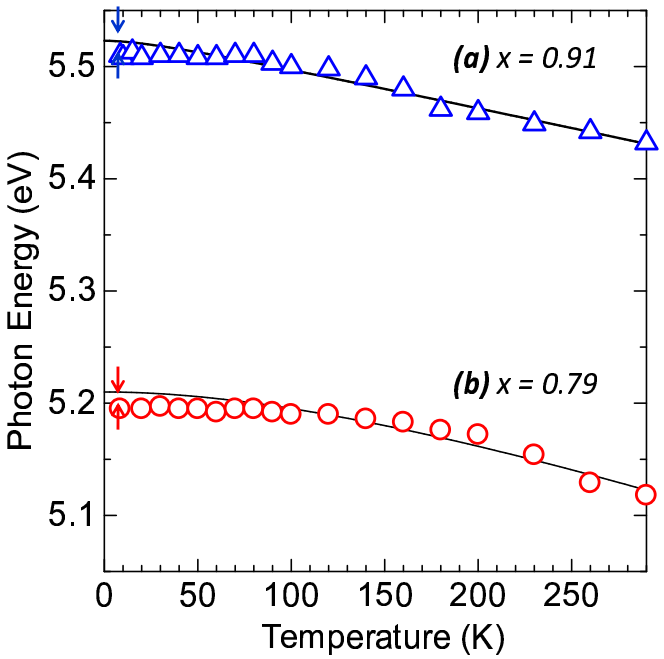

Figure 4.21: Weak energy separation between the PL peak energy measured and the energy predicted using Varshni equation. The dashed line is the least-square fit from the experiment data.

4.7 Power Dependence of PL

In this section, let us study the effect of highly exciting the AlGaN QWs by photoluminescence. The QW samples are kept inside to 8.5 K inside the cryostat. The frequency of the ArF excimer laser was maintained at 25 Hz. The excitation power was varied between 0.01 - 10 mW (laser spot size: 1 mm x 2.5 mm). The samples measured are: $x = 0.79$, $L_w = 2.5$ nm, 5 nm and, 10 nm. Another sample has $x = 0.91$, $L_w = 1.7$ nm and 6.8 nm.

In the previous discussions, it has been assumed the all the states in the conduction band are empty. But in the presence of free carriers, the absorption is modified by the change in the distribution function and many-body effects (band gap renormalization).

4.7.1 Burstein-Moss Shift

This phenomenon explains the shift of the absorption edge to higher energies (blue shift). With presence of free electrons that occupy the bottom of the conduction band, the transition from those band are blocked. A more detailed discussion will now focus on the band gap widening and narrow-

ing. In the pure and undoped crystal the band gap is defined as the energy separation between the valance and conduction band edge. Since the Pauli principle prevents states from being doubly occupied and the optical transitions only occur vertically (where the Fermi momentum is the same), the energy gap is given at these points. The blocking of the low energy states in the conduction band is known as the Burstein-Moss effect and enhances the optical gap by

$$\Delta E_{\mathrm{BM}} = \frac{\hbar^2 k_F^2}{2m_r} = \frac{\hbar^2}{2m_r}(3\pi^2 N)^{2/3} \tag{4.37}$$

where k_F is the Fermi wavevector ($k_F = (3\pi^2 N)^{1/3}$) and m_r is the reduced mass.

4.7.2 Band gap Renormalization

Figure 4.22 shows the schematic of the state of excitons at different excitation densities. Let us consider an experiment in which we take a powerful laser and tune in to one of the exciton absorption lines. The laser creates excitons in the sample with a density proportional to the laser power. At low laser power (Figure 4.22a), the density of the exciton is small and the separation between the excitons is large. Since low density, the exciton-exciton interaction is negligible. As the power is increased (Figure 4.22b), the density of the excitons increases and increasing the power high enough, the density will be high enough that the exciton wave functions overlap. At this point, it is expected that the exciton-exciton interaction will be significant. It can be observed from Fig. 4.22b that the exciton wave function overlap occurs when the exciton-exciton distance equals the exciton diameter. The density at which this occurs is called the Mott density N_{Mott}, and can be expressed as (Debye-Hückel model) [23]

$$N_{Mott} = \frac{(1.19)^2 k_B T_c}{4E_{ex} a_\perp^2 a_\parallel}, \tag{4.38}$$

where E_{ex} is the exciton binding energy, $a_\perp$ and $a_\parallel$ are the Bohr radius, T_c is the carrier temperature. For the case of AlGaN experiment at 8.5 K, the Mott density is calculated to be $N_{Mott} \sim 3.5 \times 10^{17}$ cm^{-3}. When the exciton density approaches N_{Mott}, a number of effects can occur. For one, the collisions between the excitons cause the exciton gas to dissociate into an electron-hole plasma (EHP). This causes exciton broadening (or broadening of excitonic resonance) with a reduction in the absorption strength thus the

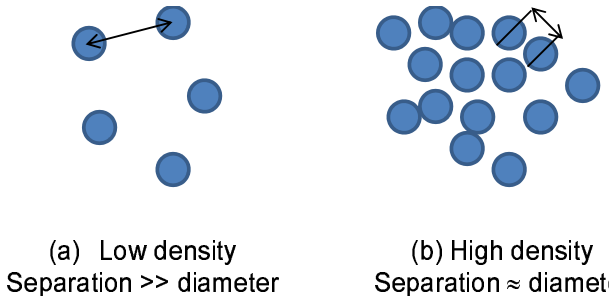

Figure 4.22: Distribution of the free excitons in the crystal. (a) At low densities, the excitons are randomly distributed throughout the excitation volume thus inter-exciton separation is large. (b) At high densities, the wave functions overlap when the exciton-exciton separation becomes comparable to the exciton diameter.

absorption edge shifts to smaller energies (red shift).

The peak position (E_p) for spontaneous emission of the EHP is [24]

$$E_p = \tilde{E}_g(T_c, N) + k_B T_c/2, \tag{4.39}$$

where T_c is the carrier temperature and $\tilde{E}_g$ is the band gap renormalization energy, which in renormalization theory [25] is connected with the screening length λ as

$$\tilde{E}_g = E_g - \frac{\pi e^2}{96\varepsilon}\lambda^{-1}. \tag{4.40}$$

The screening is described by the Debye length $\lambda = \sqrt{\frac{2e^2 n}{\varepsilon k_B T_c}}$. From the band gap renormalization equation shown above, the redshift ΔE_{EHP} can be obtained as

$$\Delta E_{EHP} = \frac{\pi e^2}{96\varepsilon}\lambda^{-1} = \frac{\pi e^2}{96\varepsilon}\sqrt{\frac{2e^2 n}{\varepsilon k_B T_c}}. \tag{4.41}$$

4.7.3 Derivation of the Carrier Density

In order to study the free carriers, the carrier density introduced by the laser into the sample must be estimated. The generation of carriers is proportional to the energy of the laser. The energy (J) of the laser is

$$E_{ex} = \frac{P}{f}\frac{f^{-1}}{p}, \tag{4.42}$$

and the total number of carriers N_c,

$$N_c = \frac{E_{ex}\tau}{eE_{\mathrm{ArF}}}(1 - \exp(-\alpha d)), \tag{4.43}$$

where α is the absorption coefficient (cm^{-1}) of AlGaN and AlN, τ is the radiative lifetime (s). For simple calculation, $\alpha = 10^5$ cm^{-1}, $\tau = 1$ ns. E_{ArF} is the photon energy of the excimer laser and while e is the charge of the electron. The carrier density in 1 QW $n_{c,1QW}$ [cm^{-3}],

$$n_{c,1\mathrm{QW}} = \frac{N_c}{c_{\mathrm{QW}} S L_w}, \tag{4.44}$$

where S is the spot area, c_{QW} is the number of QW layer. In this experiment, $f = 100$ Hz, $S = 2.5 \times 10^{-2}$ cm^2, $p = 4$ nm, $d = (750 + L_w c_{QW}) \times 10^{-7}$ cm, $c_{QW} = 10$, P is the laser excitation power. The plot of carrier density for 2.5 nm, 5.0 nm, and 10 nm $Al_{0.79}Ga_{0.21}N$/AlGaN is shown in Figure 4.23 [18].

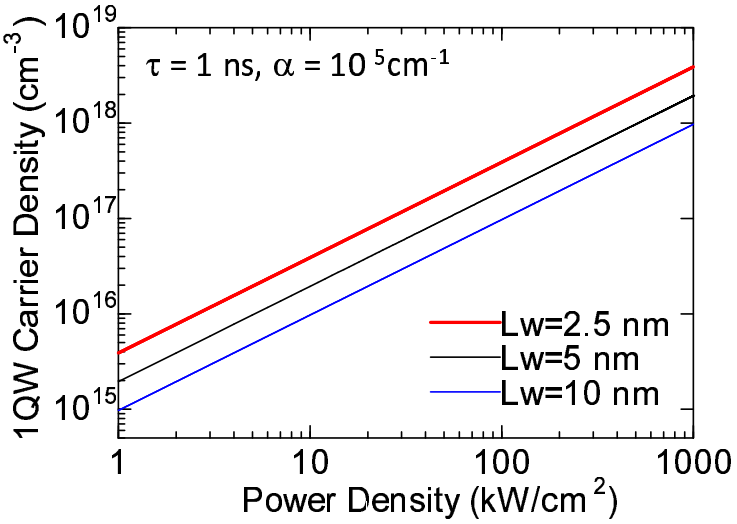

Figure 4.23: The relationship between the estimated carrier density in one QW layer with the excitation power density.

4.7.4 Experimental Results and Discussion

The spectra of excitation power density with the peak position is shown in Figure 4.24 for $Al_{0.79}Ga_{0.21}N$/AlGaN samples with (a) 2.5 nm and (b) 5 nm well widths. The broken vertical line is the calculated transition energy of the QW. For 2.5 nm QW, the peak position moves to the calculated transition energy. The same is true also for 5 nm QW however, the position shift seems to level off.

Figure 4.25 summarizes the effect of excitation power density with peak position and PL intensity for $L_w = 2.5$ nm $Al_{0.79}Ga_{0.21}N$/AlN QWs. It can

be seen in the figure the Mott density, the transition between the many body effect and electron- hole plasma. Above the Mott density is the electron-hole plasma characterized by a slope of near unity. On the other hand, the many body effect region has a slope higher than that in EHP.

Moreover, the plot of the excitation power density dependence of $L_w = 5$ nm $Al_{0.79}Ga_{0.21}N$/AlN QWs is shown in Figure 4.26. This is the same sample that obtained the highest PL intensity ratio (∼36 %) between RT and LT. The same trend can be seen as with $L_w = 2.5$ nm. Excitons are already observed in the low excitation power density side, as characterized by the slope (m) equal to unity. Pushing the excitation power density toward much lower regime would be able us to identify the fine features of the QW layer. Moreover, an interesting phenomenon is observed regarding the behavior of peak position with increasing power density. It can be observed that there is no shift of peak position toward higher energy for this sample which is worthy of further analysis.

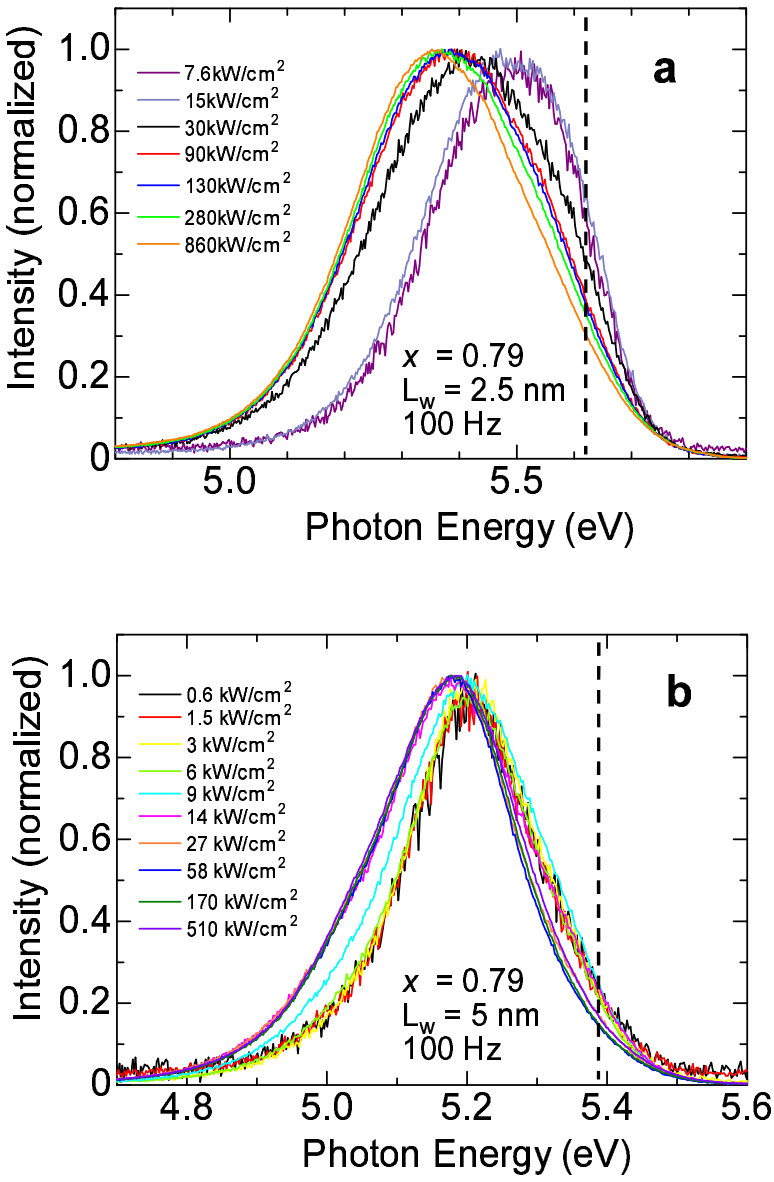

Figure 4.24: PL spectra of $Al_{0.79}Ga_{0.21}N$/AlN QWs with well width of (a) 2.5 nm and (b) 5 nm well width. The position peaks moves closer to the calculated transition energy with decreasing power density.

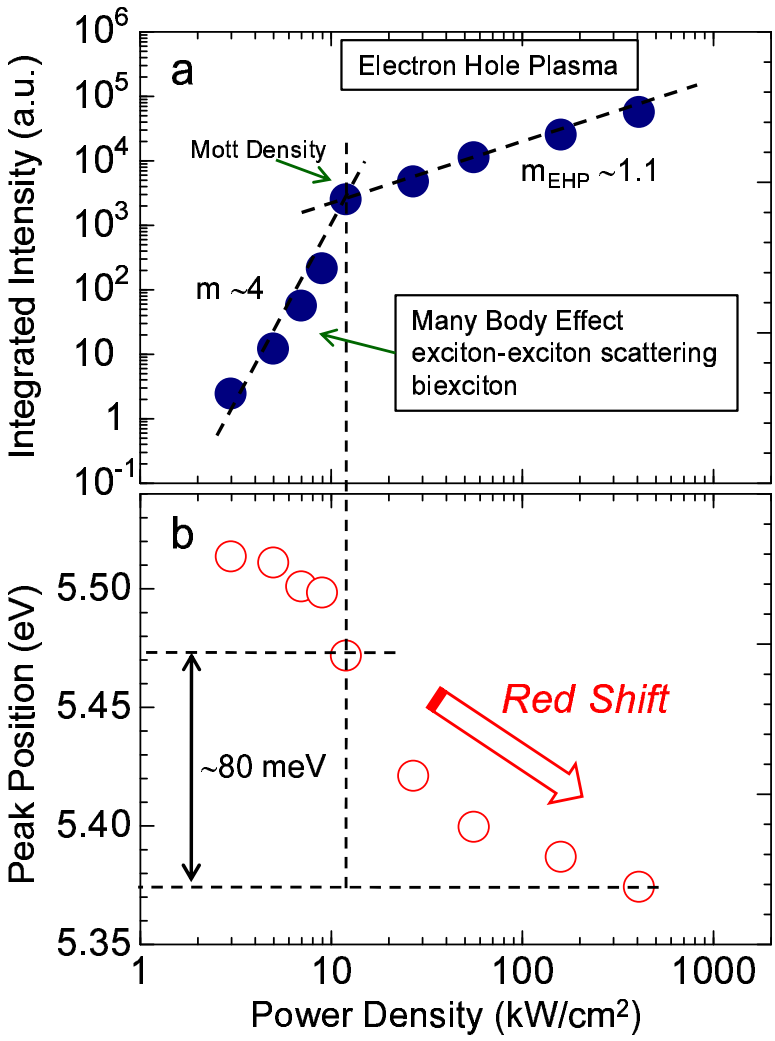

Figure 4.25: Result of power density PL for $L_w = 2.5$ nm $Al_{0.79}Ga_{0.21}N$/AlN QWs. (a) Plot of integrated intensity with power density. Below the Mott density (N_{Mott}), many body effect dominates while above N_{Mott}, electron hole plasma (EHP) transition dominates. (b) The peak position with power density. Peaks shift to higher energy during EHP.

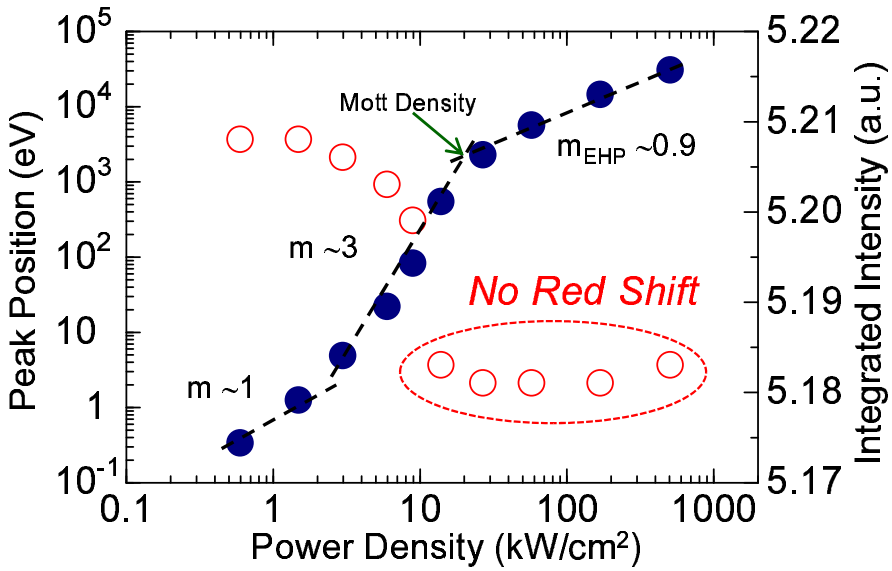

Figure 4.26: The plot of the excitation power density with peak position and PL intensity for the sample with the highest η ($Al_{0.79}Ga_{0.21}N$/AlN QWs, L_w = 2.5 nm). No red-shift was observed with increasing excitation density - an anomalous behavior worthy of further analysis.

4.8 Summary

In summary, a successful fabrication of Al-rich ($x > 0.69$) $Al_xGa_{1-x}N$/AlN quantum by Modified MEE was achieved. The Al incorporation was controlled by the growth temperature and using the same flow rates of TMA, TMG and NH_3. The successful fabrication of the $Al_xGa_{1-x}N$/AlN QWs was confirmed by the satellite peaks observed from x-ray diffraction measurements. From this measurement, the well width thickness and Al composition were also estimated and further confirmed by x-ray rocking curve simulations. Well layers as thick as ∼16 nm still showed coherent growth as confirmed by reciprocal-space mapping measurements.

Photoluminescence measurements were performed to assess the optical quality of the QW device. First, the successful fabrication of quantum with different band gaps or emission wavelengths were confirmed. Then linewidths of the grown QW were compared with theoretical calculation where the experimentally-observed linewidths were broader. Such broad linewidths were correlated with alloy broadening, carrier localization and potential fluctuations. Alloy broadening was estimated theoretically but the could not account for the linewidth broadening of the samples. Therefore, the effect of well with-width fluctuations were accounted. This fluctuation was severe when the well-width is smaller. Exciton localization due to alloy well-width fluctuation and alloy disorder must also be considered.

The broad line width obtained from the QW samples can not be correlated with exciton localization, well-width fluctuation, or alloy broadening only. The high carriers injection in the QW must also be considered. The effect of these were broadening of the line width (many body effect) and peak position shift (Burstein-Moss Shift).

References

[1] L. Esaki and R. Tsu, "Superlattice and Negative Differential Conductivity in Semiconductors," *IBM J. Res. Develop.,* **14**, 61, (1970).

[2] B. D. Cullity, *Elements of X-ray Diffraction,* 2nd ed., Addison-Wesley, (1978).

[3] S. Yoshida, S. Misawa, and S. Gonda,"Epitaxial Growth of GaN/AlN Heterostructures," *Journal of Vacuum Science & Technology B,* **1**, 250, (1983).

[4] F. Yun, M. A. Reshchikov, L. Hei, T. King, H. Morkoć, S. W. Novak, and L Wei, "Energy Band Bowing Parameter in $Al_xGa_{1-x}N$ Alloys," *J. Appl. Phys.,* **92**, 4837, (2002).

[5] S. L. Chuang and C. S. Chang, "**k**·**p** Method for Strained Wurtzite Semiconductors," *Phys. Rev. B,* **54**, 2491, (1996).

[6] S. L. Chuang and C. S. Chang "A Band-Structure Model for Strained Quantum-Well Wurtzite Semiconductors," *Semicond. Sci. Tech.,* **12**, 252, (1997).

[7] F. Bernardini, V. Fiorentini, and D. Vanderbilt, "Spontaneous Polarization and Piezoelectric Constants in III-V Nitrides," *Phys. Rev. B,* **56**, R10024, (1997).

[8] S. H. Park and , S. L. Chuang, "Spontaneous Polarization Effects in Wurtzite GaN/AlGaN Quantum Wells and Comparison with Experiment," *Appl. Phys. Lett.,* **76**, 1981, (2000).

[9] I. Vurgaftman and J. R. Meyer, "Band Parameters for Nitrogen-Containing Semiconductors," *J. Appl. Phys.* **94**, 3675, (2003).

[10] C. Bodin, R. Andre, J. Cibert, L. S. Dang, D. Bellet, G. Feuillet, and P. H. Jouneau, "Optical Linewidth and Field Fluctuations in Piezoelectric Quantum Wells," *Phys. Rev. B,* **51**, 13181, (1995).

[11] A. Bonfiglio, M. Lomascolo, G. Traetta, R. Cingolani, A. Di Carlo, F. Della Sala, P. Lugli, A. Botchkarev and H. Morkoć, "Well-Width Dependence of the Ground Level Emission of GaN/AlGaN Quantum Well," *J. Appl. Phys.,* **87**, 2899, (1999).

[12] K. C. Zeng, J. Li, J. Y. Lin, and H. X. Jiang, "Well-Width Dependence of the Quantum Efficiencies of GaN/$Al_xGa_{1-x}N$ Multiple Quantum Wells," *Appl. Phys. Lett.,* **76**, 3040, (2000).

[13] R. W. Keyes, "Hydrogen-like Impurity States in Axially Symmetric Crystals," *IBM J. Res. Dev.* **5**, 65, (1961).

[14] M. Kumagai, S. L. Chuang, and H. Ando, "Analytical Solutions of the Block-Diagonalized Hamiltonian for Strained Wurtzite Semiconductors," *Phys. Rev. B* **57**, 15304, (1998).

[15] E. F. Schubert, E. O. Gobel, Y. Horikoshi, K. Ploog, and H. J. Queisser, "Alloy Broadening in Photoluminescence Spectra of $Al_xGa_{1-x}As$," *Phys. Rev. B,* **30**, 813, (1984).

[16] G. Steude, B. K. Meyer, A. Goldner, A. Hoffman, F. Bertram, J. Christen, H. Amano, and I. Akasaki, "Optical Investigations of AlGaN on GaN Epitaxial Films," *Appl. Phys. Lett.,* **74**, 2456, (1999).

[17] S. M. Lee and K. K. Bajaj, "A Quantum Statistical Theory of Linewidths of Radiative Transitions due to Compositional Disordering in Semiconductor Alloys," *J. Appl. Phys.,* **73**, 1788, (1993).

[18] T. Oto, "Deep-Ultraviolet Emission Mechanisms in Al-rich AlGaN/AlN Quantum Wells," Bachelor's thesis, Kyoto University, (2009).

[19] G. Coli, K. K. Bajaj, J. Li, J. Y. Lin, and H. X. Jiang, "Excitonic Luminescence Linewidths in AlGaN Alloys with High Aluminum Contents," *Appl. Phys. Lett.,* **80**, 2907, (2002).

[20] T. M. Al Tahtamouni, N. Nepal, J. Y. Lin, H. X. Jiang, and W. W. Chow, "Growth and Photoluminescence Studies of Al-rich AlN/$Al_xGa_{1-x}N$ Quantum Wells," *Appl. Phys. Lett.,* **89**, 131922, (2006).

[21] Johnson Lee, Emil S. Koteles, and M. O. Vassell, "Luminescence Linewidths of Excitons in GaAs Quantum Wells Below 150 K," *Phys. Rev. B,* **33**, 5512, (1986).

[22] M. D. Bremser, *Gallium Nitride and Related Semiconductors,* edited by J. H. Edgar, S. Strite, I. Akasaki, H. Amano, and C. Wetzel, Institute of Electrical Engineers, London, p. 147, (1999).

[23] F. Binet and J. Y. Duboz, J. Off and F. Scholz, "High-excitation Photoluminescence in GaN: Hot-carrier Effects and the Mott Transition," *Phys. Rev. B,* **60**, 4715, (1999).

[24] A. Žukauskas, S. Juršėnas, G. Kureilčik, G. Tamulaitis, M. S. Shur, R. Gaska, J. W. Yang, and M. A. Khan, "Finite-Temperature Band Gap Renormalization in Highly Photoexcited GaN Epilayers," *Phys. Stat. Sol. (B),* **216**, 501, (1999).

[25] L. Banyai and S. W. Koch, "A Simple Theory for the Effects of Plasma Screening on the Optical Spectra of Highly Excited Semiconductors," *Journal of Physics B: Condensed Matter,* **63**, 283, (1986).

Chapter 5

Optical Polarization Anisotropy in AlN and Al-rich AlGaN/AlN QWs

5.1 Introduction

In previous chapters, the inferior quality of AlN was addressed by developing a new growth method which is called Modified MEE. The quality of the grown AlN epilayer was the assessed through studying its various structural and optical properties. After confirming the superior quality of AlN epilayer, the fabrication of $Al_xGa_{1-x}N$/AlN QWs (QWs) was performed. For the fabrication of QWs, a new growth technique was employed and was based on Modified MEE method. Various structural and optical properties of the QWs was performed to confirm its robust quality.

In this chapter, as a continuation of the study of various optical properties of Al-rich AlGaN/AlN QWs, the optical polarization property of $Al_xGa_{1-x}N$/AlN QW is discussed in detail. The importance of this study originates from the differences in the valence bands (heavy hole: HH, light hole: LH and spin-orbit: SO) lineup between AlN and GaN that make up the AlGaN alloy. Because of this, it is important to determine the optical polarization behavior with regard to the occurrence of the polarization switch at a certain Al composition (x). Particularly, the optical polarization anisotropy in Al-rich $Al_xGa_{1-x}N$/AlN (x>0.69) multiple QWs (MQWs) grown on sapphire (0001) substrates will be investigated by photoluminescence (PL) spectroscopy. Moreover, the effect of quantum confinement on the optical polarization switch will be discussed and collated with other ma-

terial systems such as the case of bulk AlGaN and thin AlGaN layer grown on AlN.

5.2 Unique Optical Properties in AlGaN/AlN QWs

5.2.1 AlN and GaN Band Structure

In wurzite semiconductors, the valence band maximum is split both by the spin-orbit interaction ($\triangle_{so}$) and by the non-cubic crystal-field (Δ_{cr}) splitting energy near the Γ point in the Brillouin zone. This energy splitting gives rise to the three states in the Brillouin zone center, namely, Γ_9, Γ_7, and Γ_7. It was predicted by theoretical calculation that the order of these bands is fundamentally different between AlN and GaN due to the difference in the crystal-field splitting energy of AlN and GaN [1, 2]. Because of this, the transition between the lowest conduction band and top-most valence band is different between AlN and GaN. This optical selection rule influences the optical properties of AlGaN alloy. While AlN was found to have a negative crystal-field splitting energy of $\Delta_{cr} = -217$ meV [1–5], GaN was found to have a positive Δ_{cr} of 11 meV [6].

The three interband transitions in AlN and GaN that result from the splitting of crystal field and spin-orbital splitting energy are shown in Figure 5.1. This splitting leads to valence band arrangements in the order of Γ_7, Γ_9, and Γ_7 from the top for AlN and in the oder of Γ_9, Γ_7, and Γ_7 for the case of GaN. Conversely, the interband transition between the lowest conduction band to the topmost valence band occur determine the bandgap energy.

The spin-orbital splitting energy of AlN was experimetally determined to be +36 meV [4]. For GaN, this spin-orbital splitting energy was also experimentally determined to be +11 meV [7]. However, the opposite signs of crystal-field energy in AlN and GaN led to their differences in interband transition. This crystal-field splitting energy is strongly dependent on the structural parameters that constitute a material, in terms of its cell-internal structural parameter u and the ratio c- and a-lattice constant (c/a) [1, 2]. Because of the strong ionicity of AlN, the lattice is strongly distorted from that of its ideal wurzite structure, giving rise to its negative crystal-field splitting energy. Owing to this, the valence band line up is different from that in GaN, as depicted in Figure 5.1, showing the three transitions from the valence bands to the lowest Γ_{7c} conduction band depicted as A, B and C

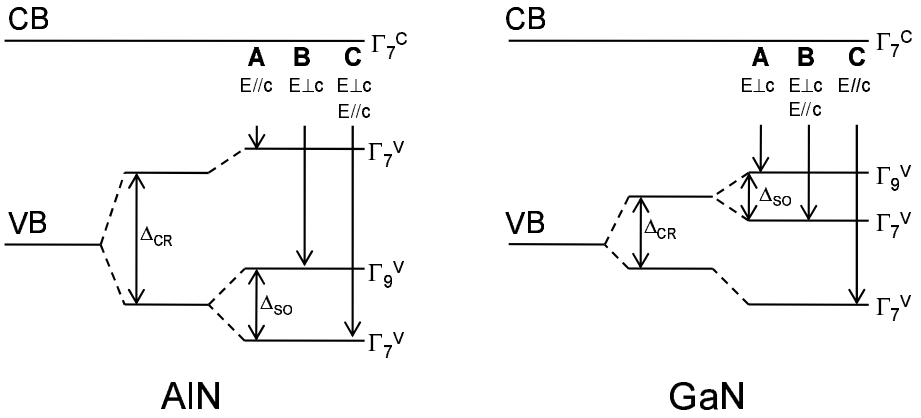

Figure 5.1: Optical transitions between the conduction band the valence band at the Γ point in AlN and GaN. A, B and C band transitions are shown in the order of increasing transition energy as well as the corresponding allowable light polarization.

transition in the order of increasing transition energy.

As a consequence of the negative crystal-field splitting energy in AlN, the A-excitonic transition has Γ_7 character. This A transition is allowed for the electric field light polarization $\boldsymbol{E}$ parallel to the c-axis ($\boldsymbol{E} \parallel$ c). On the other hand, the B and C transitions are allowed for $\boldsymbol{E}$ perpendicular to the c-axis ($\boldsymbol{E} \perp$ c). Conversely, the A transition is almost prohibited for $\boldsymbol{E}$ perpendicular to the c-axis ($\boldsymbol{E} \perp$ c) and vice versa for B and C transitions for ($\boldsymbol{E} \parallel$ c). For AlN grown on c-plane, it exhibits a weaker surface emission ($\boldsymbol{E} \perp$ c) while an intense emission is expected from from a- or m-planes, in accordance to the optical selection rule. An opposite case is true for GaN grown on c-plane where the intense emission is observed from the surface while the weak emission is observed from m- or a-plane. Along with the hexagonal crystal structure, the optical polarization property of AlN and GaN is schematically drawn in Figure 5.2.

5.2.2 Optical Transition in Ternary AlGaN

When Ga(Al) is incorporated into AlN(GaN) to form an AlGaN ternary alloy, an interesting optical polarization phenomenon occurs. This is because of their differences in valence bands lineup as explained above. For the III-V semiconductors such as AlN and GaN, the conduction states transform like s-functions (S-symmetry) while the valence states transform like p-functions (symmetry P_x, P_y, P_z). Considering the case of AlN, in the absence of spin-orbit interaction, the top of the valence at the Γ point (valence band maxi-

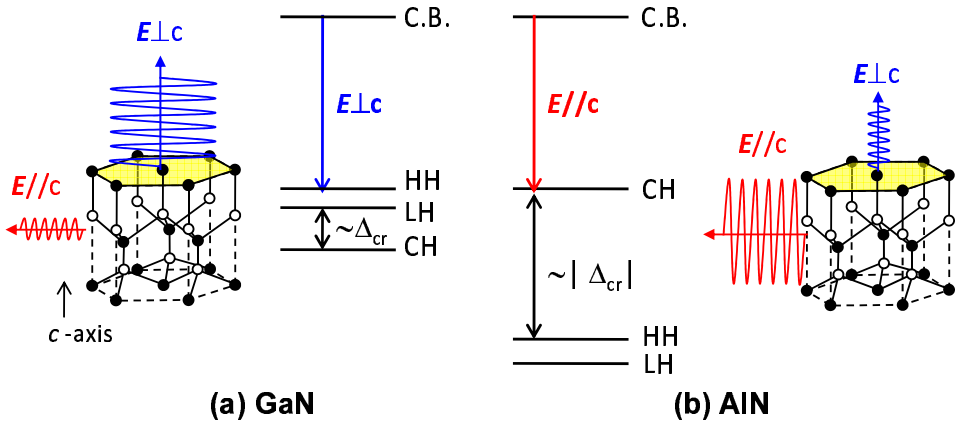

Figure 5.2: The difference in crystal-field splitting energy of (a) GaN and (b) leads to the unique optical polarization properties in AlGaN. While an intense emission from the c-plane is expected from GaN, weaker surface emission is expected for AlN due to their differences in crystal-field energy ($\triangle_{cr}$).

mum) is split into single- and twofold-degenerate states. Using the irreducible representations of group theory, the single-degenerate state is labeled as Γ_1 whose wave functions transform like Z. For the twofold-degenerate state, it is labeled as Γ_6 and the wavefunction transforms like X and Y. With the presence of spin-orbit interaction, which splits the valence states, the spin component (spin up or down) must be considered and the valence p-states have mixed-spin character. Thus, the twofold-degenerate Γ_6 is split into Γ_9 and Γ_7 levels while the single-degenerate Γ_1 is labeled as Γ_7 [1, 8].

Because the topmost Γ_7 in AlN is the $|Z>$-like CH state and Γ_9 in GaN is the $|X \pm \mathrm{i}\, Y>$-like HH state, the emission from high (low) Al-content AlGaN is expected to be polarized along the $\boldsymbol{E} \parallel$ c ($\boldsymbol{E} \perp$ c) direction. This means that a high-Al content AlGaN behaves like AlN while low Al-content AlGaN behaves like GaN, as depicted in Figure 5.3. This change in the optical emission property with Al incorporation occurs at a certain Al composition (x), which is dependent on the material system. This system, whether a bulk AlGaN, strained AlGaN or quantum confined AlGaN on AlN, could affect the polarization anisotropy or the Al composition with which polarization switch occurs. This characteristic has been reported for AlGaN thick layers in which the polarization switched from $\boldsymbol{E} \perp$ c to $\boldsymbol{E} \parallel$ c at $x = 0.25$ as the Al composition is increased [9]. This result also implies that the characteristic weak surface emission of AlN is already observable in AlGaN layer with Al composition as low as 0.25. This has prompted the idea to use non-polar planes where the expected strong surface emission can be achieved.

One of the main reasons for still unverified polarization switch is the compromising quality of AlGaN layer, which still remains a challenge compared to the more mature growth technology in InGaN systems. Thanks to the modified MEE method, the fabrication of high-quality AlGaN/AlN QWs having different Al composition is already realized.

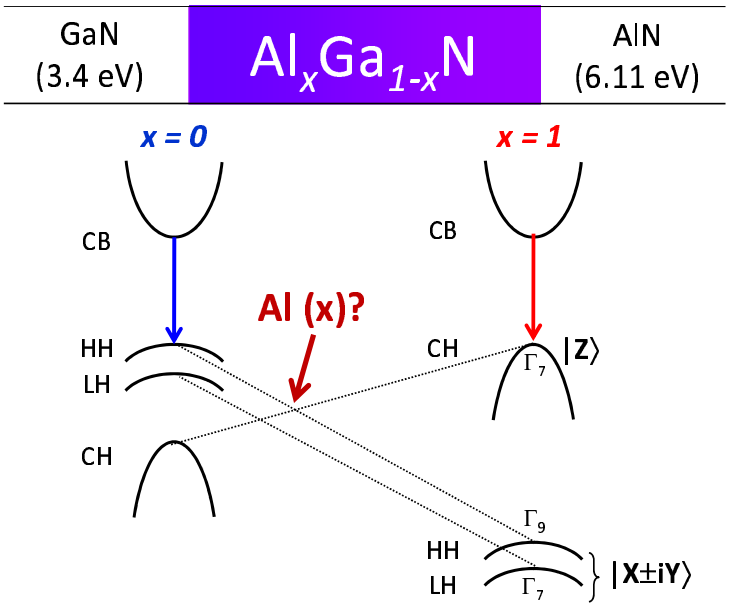

Figure 5.3: The valence bands lineup between GaN and AlN. The switch of optical polarization occurs at a certain Al composition (x) in $Al_xGa_{1-x}N$/AlN. This Al composition at which the polarization switch occurs is dependent on the material system AlGaN is fabricated onto.

5.2.3 Theoretical Study on Intense Surface Emission from *c*-plane

The result of the polarization property on thick AlGaN layers presented above further supported the idea that non-polar planes are the answer ($\boldsymbol{E} \perp$ c) to achieve intense surface emission from Al-rich AlGaN [9]. But one great challenge that must be overcome is to optimize the growth technology along these planes, which still remains at early development stages up to this writing. On the other hand, it was demonstrated by a theoretical investigation that, by engineering the valence band through decreasing the well width (L_w) and/or introducing in-plane compressive strain in c-oriented AlGaN QWs, (with an infinite barrier height) remarkable enhancement in surface emission ($\boldsymbol{E} \perp$ c)

can be achieved [10]. This is clearly advantageous for conventional surface emitters relying on better-established c-oriented AlGaN QWs. This theoretical prediction has not experimentally been demonstrated yet; rather, luminescence from c-oriented $Al_{0.66}Ga_{0.34}N/Al_{0.76}Ga_{0.24}N$ QWs on $Al_{0.86}Ga_{0.14}N$ (0.6 μm)/AlN (1.5 μm) [3,4] and $Al_{0.11}In_{0.03}Ga_{0.86}N/Al_{0.2}In_{0.03}Ga_{0.77}N$ QWs on $Al_{0.2}Ga_{0.8}N$ (2μm)/AlN (1μm) [11] have been reported to exhibit emission with $\boldsymbol{E} \parallel$ c.

5.2.4 Purpose of Study

The main purpose of this chapter is to analyze the polarization property of Al-rich $Al_xGa_{1-x}N$/AlN ($x > 0.69$) multiple QWs (MQWs) grown by modified MEE on sapphire (0001) substrates. The experimental result will be correlated with the theoretical investigation and a simple model will be presented.

5.3 Experimental Procedure

5.3.1 Sample

The samples are the same as those used in Chapter 4. The $Al_xGa_{1-x}N$/AlN MQWs were fabricated on ∼600-nm-thick AlN/sapphire (0001) templates. The 10-period MQWs have barrier (AlN) thickness of ∼12.5 nm (21 growth cycles) while the AlGaN well layer has a thickness varied per AlGaN growth cycle (1 cycle as the minimum to 10 cycles). The $Al_xGa_{1-x}N$ layers were grown coherently on AlN, as demonstrated by reciprocal space mapping measurements discussed in Chapter 4. To investigate the optical polarization properties, the $\boldsymbol{E} \perp$ c and $\boldsymbol{E} \parallel$ c components were resolved by cleaving the samples in order to collect the photoluminescence signal from the samples' edge. Cleaving was performed by a laser scriber machine, exposing the m-plane of the AlN. The schematic of the sample is shown in Figure 5.4.

5.3.2 Optical Polarization PL Setup

Figure 5.5 shows the DUV PL setup used for the optical polarization study. The optical measurements were carried out at 8.5 K under cryogen-free cryostat. An ArF (λ = 193 nm) pulsed laser with an average laser power of 2.5 mW was used . The excitation laser was incident at the surface normal and the PL was collected from the edge by one lens and focused at the entrance

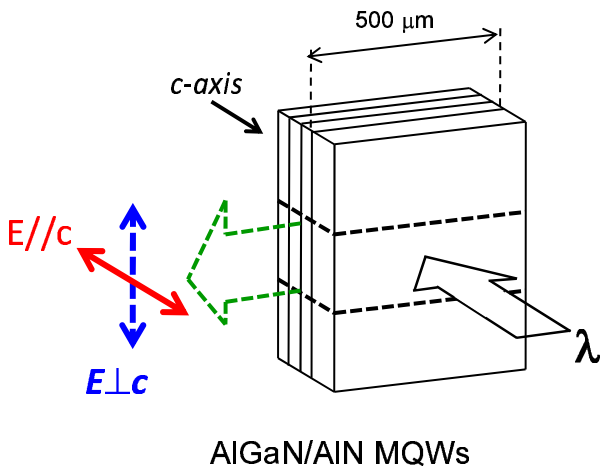

Figure 5.4: Schematic AlGaN/AlN MQWs samples cleaved along the m-plane with respect to AlN used for optical polarization experiments. Using this this set-up, the $\boldsymbol{E} \perp$ c and $\boldsymbol{E} \parallel$ c components are clearly resolved.

of a 30-cm monochromator by another lens, as shown in the inset of Figure 5.5. This configuration allowed the polarization PL properties of $\boldsymbol{E} \perp$ c and $\boldsymbol{E} \parallel$ c to be directly assessed using a polarizer inserted between these lenses. All the spectra of AlGaN/AlN MQWs were treated by the PL system polarization. The system polarization spectra is seen from the inset in Figure 5.5.

5.3.3 Al Composition Dependence Polarization PL from $Al_xGa_{1-x}N$/AlN QWs

The polarization dependence of Al composition (x) in $Al_xGa_{1-x}N$/AlN QWs is discussed first. Figure 5.6 shows the polarization PL spectra of a series of ∼1.5-nm-thick $Al_xGa_{1-x}N$/AlN QWs with various Al compositions, using the experimental set-up described in Figure 5.5. Also shown in the inset is the polarization PL of AlN used as the template epilayer. The solid line indicates the emission perpendicular to the growth c-axis and the broken line is the polarization parallel to the c-axis. The polarization degree (ρ) can be expressed mathematically as:

$$\rho = \frac{I_{\perp} - I_{//}}{I_{\perp} + I_{//}}, \tag{5.1}$$

where I is the PL intensity perpendicular ($\perp$) and parallel ($//$) to the c-axis. First, the polarization degree of AlN was evaluated and it showed that the

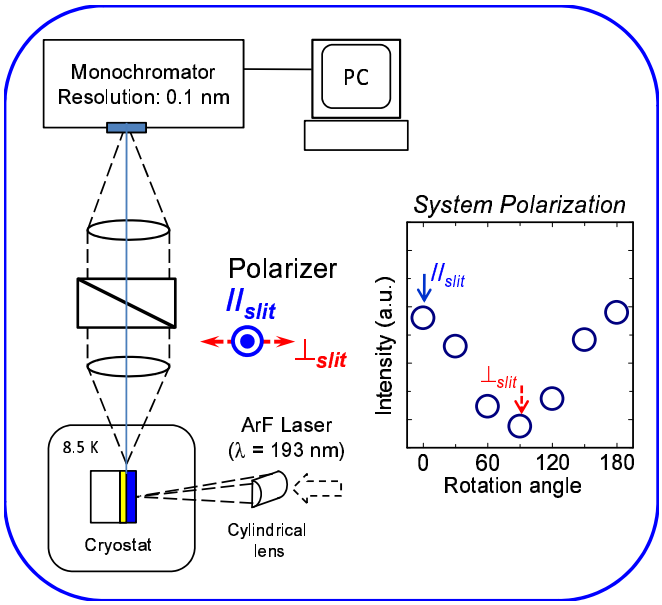

Figure 5.5: Photoluminescence (PL) experimental set-up for observing the optical polarization property of $Al_xGa_{1-x}N$/AlN QWs (QWs). Inset figure shows the configuration of the sample in detecting the PL from the edge.

degree of polarization was −0.82. This quantity signifies strong polarization along the $\boldsymbol{E}$ ∥c direction. This result is consistent with earlier reports [2–4], and verifies the experimental setup used.

For AlGaN/AlN QWs, as Al composition is decreased from 0.91 to 0.69, the predominant polarization switched from $\boldsymbol{E}$ ∥ c to $\boldsymbol{E}$ ⊥ c at Al composition $x \sim 0.82$. The polarization degrees, ρ, were evaluated and tabulated in the table below.

Table 5.1: The degree of polarization of AlN and the dependence of polarization with Al form $Al_xGa_{1-x}N$/AlN QWs. AlN shows polarization with $\boldsymbol{E}$ ∥ c while the QWs showed a polarization switch with Al composition.

Al composition (x)	0.69	0.82	0.91	1.0
ρ	0.07	0.03	-0.24	-0.82
Well Thickness (nm)	1.04	1.41	1.76	-

It is strongly emphasized that the $Al_xGa_{1-x}N$/AlN QWs with Al composition of $x = 0.82$ shows a strong surface emission. This means that even at the emission wavelength (λ) of ∼225 nm, intense surface emission can be observed. These findings indicate that the topmost valence bands of the MQWs change from Γ_7 similar to that in AlN to Γ_9 like that in GaN at x as high as 0.82. The switch in optical polarization occurs at a much higher

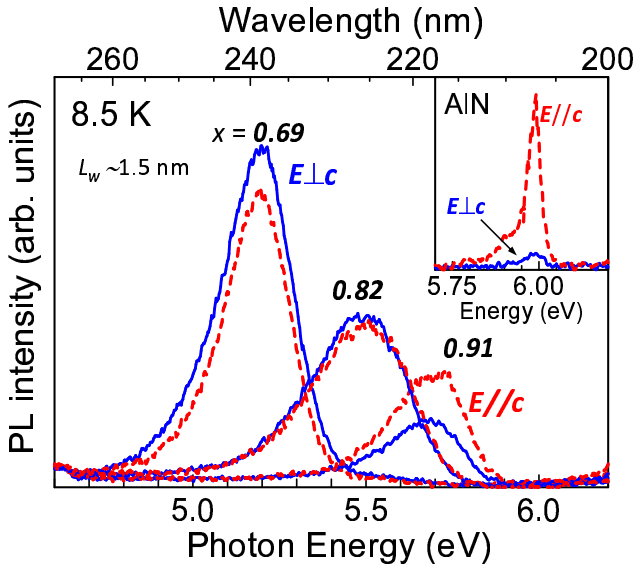

Figure 5.6: Polarization PL spectra of c-oriented $Al_xGa_{1-x}N$ (∼1.5 nm)/AlN MQWs with different Al compositions of 0.91, 0.82, and 0.69. Inset shows polarization PL spectra of c-oriented AlN.

Al composition compared to previous reports [11–13] where the mechanism is going to be discussed in the next sections.

5.3.4 Well width Dependence Polarization PL from AlGaN/AlN MQWs

The well width dependence polarization PL is then assessed by considering MQWs with Al composition of $x = 0.82$ with various well widths. The PL spectra are shown in Figure 5.7. The broken lines are those with $\boldsymbol{E} \parallel$ c polarization while those spectra with solid lines have $\boldsymbol{E} \perp$ c polarization. The calculated polarization degrees which were calculated from their peak intensities and using the equation 5.1 is tabulated in the table below.

Table 5.2: Well width dependence polarization PL from $Al_{0.82}Ga_{0.18}N$/AlN MQWs. The polarization degree changed from $\boldsymbol{E} \parallel$ c to $\boldsymbol{E} \perp$ c as the well width (L_w) is decreased.

Well width (L_w)	13 nm	8.0 nm	1.3 nm
Polarization degree (ρ)	-0.17	-0.12	0.013

The emissions from QWs thicker than 8.0 nm showed ($\boldsymbol{E} \parallel$ c) polarization while the 1.3-nm-thick QW was predominantly polarized along the ($\boldsymbol{E} \perp$

c) direction. This clearly indicates that quantum confinement affects the valence band order and, consequently, promotes ($\boldsymbol{E} \perp$ c) polarization.

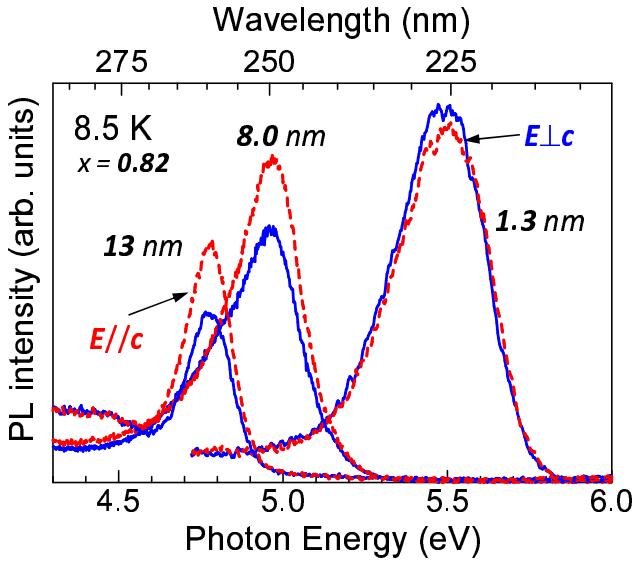

Figure 5.7: Polarization PL spectra of c-oriented $Al_{0.82}Ga_{0.18}N$/AlN MQWs with different well widths (L_w) of 1.3, 8.0, and 13 nm. The polarization changed from ($\boldsymbol{E} \parallel$ c) to ($\boldsymbol{E} \perp$ c) as the well width (L_w) is decreased.

5.4 Discussion: Polarization Anisotropy in AlGaN/AlN QWs

5.4.1 Valence Band Energies

To complete the general picture of the polarization properties in AlGaN/AlN QWs, several QWs with various Al compositions and well widths were fabricated and the result of the polarization studies is summarized in Figure 5.9. The closed circles depicts polarization perpendicular to the c-axis while open circles shows polarization parallel to the c-axis. As expected, higher Al composition results in ($\boldsymbol{E} \parallel$ c). Conversely, lower Al composition results in ($\boldsymbol{E} \perp$ c) polarization.

The broken line in the figure shows the onset of polarization switch. For QWs with well width thicker than ~3 nm, the critical Al composition for polarization switch was ~0.8 and independent of the well width (polarization switch does not change with well width). The reason for such independence on well width will be discussed in succeeding paragraphs. On the other hand,

for QWs thinner than ∼3 nm, the critical composition shifted toward a higher Al composition, which can be attributed to the quantum confinement effect.

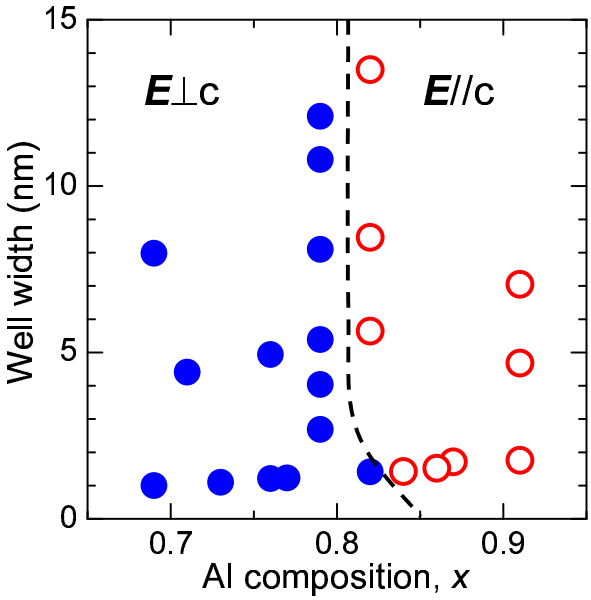

Figure 5.8: Plot of polarization direction of the emission from AlGaN/AlN QWs as functions of Al composition and well width.

As discussed in Section 5.2.2, the results from the polarization studies are closely related to the ordering of the valence bands (HH, LH and CH) as the nature of each band determines the polarization property in AlGaN. Using the $k{\cdot}p$ method with the cubic approximation [14], HH, LH and CH band-edge energies evaluated at $k = 0$, respectively are:

$$E(\Gamma_9) = \Delta_{cr} + \frac{\Delta_{so}}{3} + \theta_\varepsilon + \Delta_\varepsilon, \tag{5.2}$$

$$E(\Gamma_7) = \frac{\Delta_{cr} - \frac{1}{3}\Delta_{so} + \theta_\varepsilon}{2} + \Delta_\varepsilon + \sqrt{\left(\frac{\Delta_{cr} - \frac{1}{3}\Delta_{so} + \theta_\varepsilon}{2}\right)^2 + 2\left(\frac{1}{3}\Delta_{so}\right)^2}, \tag{5.3}$$

$$E(\Gamma_7) = \frac{\Delta_{cr} - \frac{1}{3}\Delta_{so} + \theta_\varepsilon}{2} + \Delta_\varepsilon - \sqrt{\left(\frac{\Delta_{cr} + \frac{1}{3}\Delta_{so} + \theta_\varepsilon}{2}\right)^2 - 2\left(\frac{1}{3}\Delta_{so}\right)^2}. \tag{5.4}$$

The strain effects are defined as

$$\Delta_\varepsilon = D_1\varepsilon_{zz} + D_2(\varepsilon_{xx} + \varepsilon_{yy}), \tag{5.5}$$

$$\theta_\varepsilon = D_3\varepsilon_{zz} + D_4(\varepsilon_{xx} + \varepsilon_{yy}). \tag{5.6}$$

Since the AlGaN layers are fully-strained and grown along (0001) (c-axis) direction, the strain tensor has following relation:

$$\varepsilon_{xx} = \varepsilon_{yy} = \frac{a_0 - a}{a}, \tag{5.7}$$

$$\varepsilon_{zz} = -2\frac{C_{13}}{C_{33}}\varepsilon_{xx}, \tag{5.8}$$

where a_o and a are the lattice constants of the substrates and the epitaxial layer. The Δ_{so} is the spin-orbit splitting energy, Δ_{cr} is the crystal-field splitting energy, D_i is the deformation potential, C_{ij} is the elastic stiffness constant, and ε_{xx} and ε_{zz} are the strain tensor elements along the x, y and z (c-axis) direction, respectively [14].

5.4.2 Theoretical Prediction on Polarization Switching Phenomena

For the determination of polarization switching phenomenon in AlGaN alloy, the upper Γ_7 and Γ_9 must be considered since their ordering is different from between AlN and GaN, as discussed in Section 5.2.1. Taking the difference of these two bands, the onset of polarization switch at certain alloy composition can be determined. In this study, the material systems being considered are: (1) unstrained AlGaN, (2) strained AlGaN on unstrained AlN, and (3) quantum confined AlGaN/AlN.

Thus, using the $k{\cdot}p$ approach with the cubic approximation, the energy separation between the upper Γ_7 [Equation (5.3)] and Γ_9 [Equation (5.2)] can be deduced as:

$$\begin{aligned} &E(\Gamma_7) - E(\Gamma_9) \\ &\quad = -\frac{1}{2}\left[\Delta_{cr} + \Delta_{so} + \theta_\varepsilon - \sqrt{(\Delta_{cr} + \Delta_{so} + \theta_\varepsilon)^2 - \frac{8}{3}\Delta_{so}(\Delta_{cr} + \theta_\varepsilon)}\right], \end{aligned} \tag{5.9}$$

where θ_ε has been defined in Equation 5.6.

5.4.3 Effects of Δ_{cr} and θ_ε on the Polarization switch

A simple model will be presented to explain the polarization anisotropy in AlGaN. Equation (5.9) is used to extract the critical Al composition at which polarization switch occurs in AlGaN alloy. To understand the effect of strain and quantum confinement, three material systems will be presented and these

are: (a) unstrained AlGaN, (b) strained AlGaN on unstrained AlN and, (c) AlGaN/AlN QWs. and their corresponding band structures are summarized in Figure 5.9.

AlGaN alloys fabricated under different material systems are clearly under different strain states therefore the strain component (θ_ε) affects the composition at which the polarization switch occurs. Moreover, the crystal-field parameter Δ_{cr} is defined as proportional to the deviation of the structural parameters u and the ratio c/a of their lattice constants from their corresponding unrelaxed values [17]. Thus the crystal-field parameter also affects the composition at which the polarization switch occurs. Theoretical calculations [2, 3] and a recent experiment [4] both indicate that Δ_{cr} in AlN is around -220 meV. Therefore, -217 meV [2] was used in this study, while the remaining parameters were from Reference [6].

For $Al_xGa_{1-x}N$, $E(\Gamma_7) - E(\Gamma_9)$ using Equation (5.9) can be zero at the critical Al composition ($x_{critical}$), that is, the onset of polarization switch. From the equation, the condition where the difference between $(\Gamma_7) - E(\Gamma_9)$ becomes zero ($E(\Gamma_7) - E(\Gamma_9) = 0$) corresponds to $\Delta_{cr} + \theta_\varepsilon = 0$, and thus, the critical Al composition can easily be extracted assuming a linear relationship between AlN and GaN parameters.

The case of bulk AlGaN is depicted in Figure5.9a. For this case, taking the condition of $\Delta_{cr} = 0$, the critical Al composition can be estimated to be $x = 0.044$. This means that above $x = 0.044$, ($\boldsymbol{E} \parallel$ c) becomes the dominant emission. For the case of strained AlGaN on unstrained AlN (Figure 5.9b), considering the sum of $\Delta_{cr} + \theta_\varepsilon = 0$, this moves the polarization switch to occur at $x = 0.60$. This occurrence of polarization switch from ($\boldsymbol{E} \perp$ c) to ($\boldsymbol{E} \parallel$ c) at much higher critical Al composition can be qualitatively understood by considering the effect of strain on each valence band. The in-plane compressive strain in AlGaN pushes the $|X \pm \mathrm{i}\, Y>$-related bands (Γ_9 and lower Γ_7) upwards. But the tensile strain along the growth direction pushes the |Z>-related band (upper Γ_7) downward, as schematically illustrated in Figures 5.9(a) and 5.9(b). Consequently, the energy separation between the topmost Γ_7 and Γ_9 decreased, and then a larger Al composition is necessary for the polarization switch. It should be noted that 1-μm-thick AlGaN on sapphire (0001) experimentally showed the polarization switch at $x = 0.25$ [9], implying the presence of residual strain.

An additional factor that can affect the valence band structure is the quantum confinement. Because the hole effective mass at the topmost Γ_7 in AlN is much lighter than that at Γ_9 (0.26 m_0 vs. 3.57m_0) [6], the energy of this

Γ_7 is drastically lowered by quantum confinement. As drawn in Figures 5.9(b) and 5.9(c), stronger confinement eventually causes the crossover between Γ_7 and Γ_9.

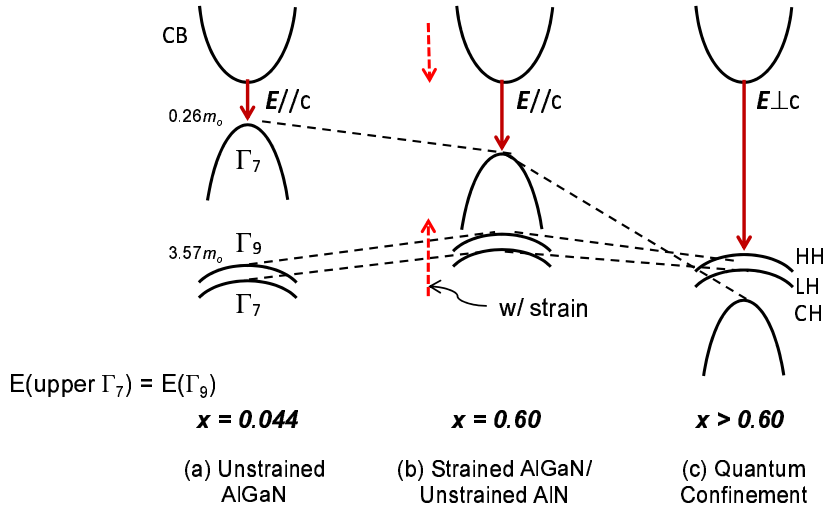

Figure 5.9: Schematic of band structures for (a) unstrained AlGaN, (b) strained AlGaN/AlN, and (c) AlGaN/AlN QWs near the Γ point. CB stands for conduction band.

To quantify the quantum confinement effect on the valence band order, the quantized levels for the upper $E(\Gamma_7)$ and $E(\Gamma_9)$ in AlGaN/AlN single QWs were evaluated numerically solving a simple one-dimensional Schrödinger equation:

$$-\frac{\hbar^2}{2m^*}\frac{\partial^2\psi(z)}{\partial z^2} = E\psi(z), \tag{5.10}$$

where strain-dependent effective mass m^* was assumed at Γ_7 [14]. Then the energy difference between $E(\Gamma_7)$ and $E(\Gamma_9)$ in the QW (that is, $E(\Gamma_7^{QW})$ - $E(\Gamma_9^{QW})$) was calculated. Figure 5.10 depicts the contour plot of the calculated energy difference between $E(\Gamma_7^{QW})$ and $E(\Gamma_9^{QW})$. As mentioned earlier, $E(\Gamma_7^{QW}) - E(\Gamma_9^{QW}) = 0$ corresponds to the occurrence of polarization switch.

When the flat-band condition was assumed by neglecting the internal electric field, the critical Al composition for $E(\Gamma_7^{QW}) - E(\Gamma_9^{QW}) = 0$ in thicker QWs approached x ~0.60, as demonstrated by the (red) thick dotted line in Figure 5.10. This is reasonable because thicker QWs resemble strained

thick AlGaN layers where the critical Al composition was determined to be 0.60 using Equation (5.9). However, this is not the case for thinner QWs as it moves the valence bands through quantum confinement as explained in Figure 5.9, which promotes the $E(\Gamma_9^{QW})$-related emission with ($\boldsymbol{E} \perp$ c). Although this tendency qualitatively fits the experimental data shown in Figure 5.8, it quantitatively does not. Hence, the effect of the internal electric field caused by the spontaneous and piezoelectric polarizations was included.

The magnitude of the internal electric field can be estimated from [15,16]

$$F_w = \frac{P_b^{SP} + P_w^{PZ} - P_b^{SP} - P_w^{PZ}}{\epsilon_w + \epsilon_b(L_w/L_b)}, \tag{5.11}$$

$$F_b = -\frac{L_w}{L_b} F_w, \tag{5.12}$$

where ϵ is the static dielectric constant, L is the layer thickness and the subscripts b and w represent the barrier and the well, while the superscripts SP and PZ represent the spontaneous and piezolectric polarization, respectively. As seen from Equation (5.11), the magnitude of the internal field depends on the relative thicknesses of the well and the barrier layers. The strain-induced piezoelectric polarization can be calculated as

$$P^{PZ} = 2\left(e_{31} - \frac{C_{13}}{C_{33}} e_{33}\right)\epsilon_{\parallel}, \tag{5.13}$$

where e_{ij} is the piezoelectric coefficients and $\epsilon_{\parallel}$ is the in-plane strain equal to ϵ_{xx}. Since the QWs were grown on thick AlN template, the AlN barrier layer is assumed to be relaxed while the AlGaN QWs experience in-plane compressive strain. Hence, the piezoelectric polarization charge in the barrier (P_{SP}^b) is zero while the values of the piezoelectric constants for $Al_xGa_{1-x}N$ used for the calculation is by linear interpolation between the reported values in literature for GaN and AlN [6].

On the other hand, because the reported spontaneous polarization in AlN spans a fairly broad range from -0.12 to -0.036 C/m^2, this was treated as a fitting parameter. Consequently, a value of -0.040 C/m^2 for spontaneous polarization provided a good agreement between the experiment (Figure 5.8) and calculation, as indicated by (black) thick and thin lines in Figure 5.10. Further decreasing the spontaneous polarization to the well-accepted -0.090 C/m^2 [6] pushed the zero line to $x \sim 0.85$. Therefore, as has been occasionally reported [16,18,19], the spontaneous polarization in AlN is considered to be -0.040 C/m^2.

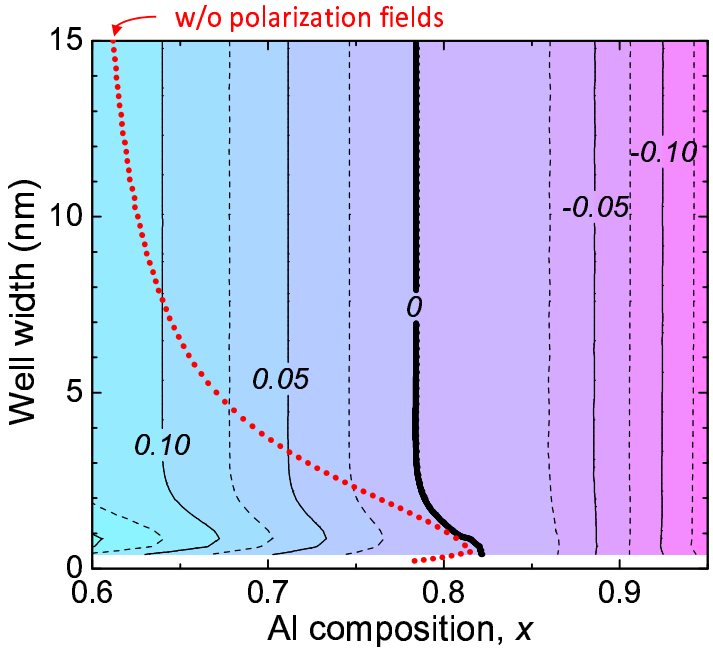

Figure 5.10: Contour plot of the calculated energy difference of $E(\Gamma_7^{QW}) - E(\Gamma_9^{QW})$. The numbers in italics are the energy difference in the unit of eV. The (red) dotted thick line is the $E(\Gamma_7) - E(\Gamma_9) = 0$ line for flat-band QWs without a polarization field, while (black) thick and thin lines are for QWs assuming the spontaneous polarization of -0.040 C/m^2

The internal electric field shifted the critical Al composition that satisfies $(E\Gamma_7^{QW}) - (E\Gamma_9^{QW}) = 0$ toward higher Al compositions, and the switch was more remarkable for thicker QWs. These are due to a triangular potential profile induced by the internal electric field as depicted in Figure 5.11. Such a profile still creates the quantum confinement effect even in thick QWs, and consequently, promotes the mechanism shown in Figure 5.9(c). Thus, the switch of the critical Al composition is governed by the quantum confinement due to the well width for thinner QWs, but is governed by that due to the internal electric field for thicker QWs.

For AlGaN-based DUV emitters reported so far, the occurrence of polarization switch varies due to the several factors which include the state of strain in the QWs. For example, the c-oriented $Al_{0.66}Ga_{0.34}N/Al_{0.76}Ga_{0.24}N$ QWs on $Al_{0.86}Ga_{0.14}N$ (0.6 μm)/AlN (1.5 μm) templates showed ($\boldsymbol{E} \parallel$ c) polarization [12, 13]. The well thickness was 5 or 10 nm. Although at first glance, the result seems to disagree with Figure 5.10, the discrepancy can

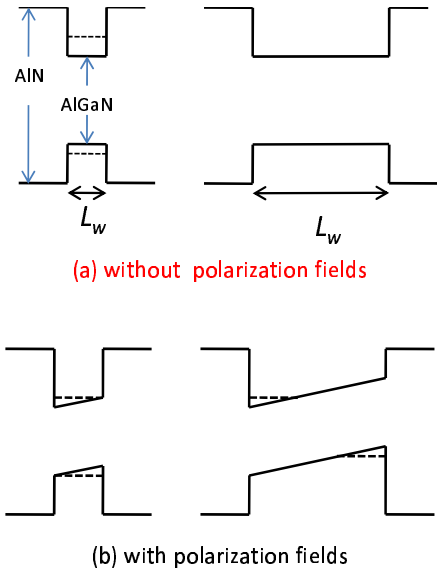

Figure 5.11: The effect of triangular profiles induced by electric fields on the critical Al composition (x) for polarization switch. When internal electric is neglected (a), the critical x approaches to 0.60 which does not fit the experimental result. When internal electric field is considered, the polarization shifts at $x \sim 0.85$, which fits the data.

be explained by (a) weak quantum confinement due to the relatively thick well width, (b) weak quantum confinement due to the $Al_{0.76}Ga_{0.24}N$ barrier layer, and (c) the weak internal electric field in the well due to the compensation with that in the $Al_{0.76}Ga_{0.24}N$ barrier layer; all of which may contribute to the promotion of ($\boldsymbol{E} \parallel$ c) polarization. Although the strain state seems complicated due to the presence of the 0.6-μm-thick $Al_{0.86}Ga_{0.14}N$ layer, the simple model presented above predicts $(\Gamma_7) - E(\Gamma_9) \sim 0$ for an $Al_{0.66}Ga_{0.34}N/Al_{0.76}Ga_{0.24}N$ QW coherently grown on AlN. This is the most extreme condition, and if the underlying $Al_{0.86}Ga_{0.14}N$ layer is relaxed to some extent, ($\boldsymbol{E} \parallel$ c) polarization is promoted, thus, there is a tolerable agreement between the model presented and the reported polarization.

5.4.4 Confirmation of Intense Surface Emission

To confirm that a strong surface emission is actually observed in $Al_xGa_{1-x}N$/AlN QWs up to 0.82, surface emission PL measurements were performed on the same samples shown in Figure 5.6. In this measurement, the laser was incident about 60 ° from the surface normal and the PL signal was collected from the surface of the sample by collimating and focusing lens going into the monochromator. The experimental set-up is shown as inset in

Figure 5.12 where it shows the relative intensities obtained from the QWs. Expectedly, an intense surface emission is observed for $Al_xGa_{1-x}N$/AlN QWs with $x \sim 0.82$ while on the other hand, weak surface emission was observed for QWs with $x \sim 0.91$.

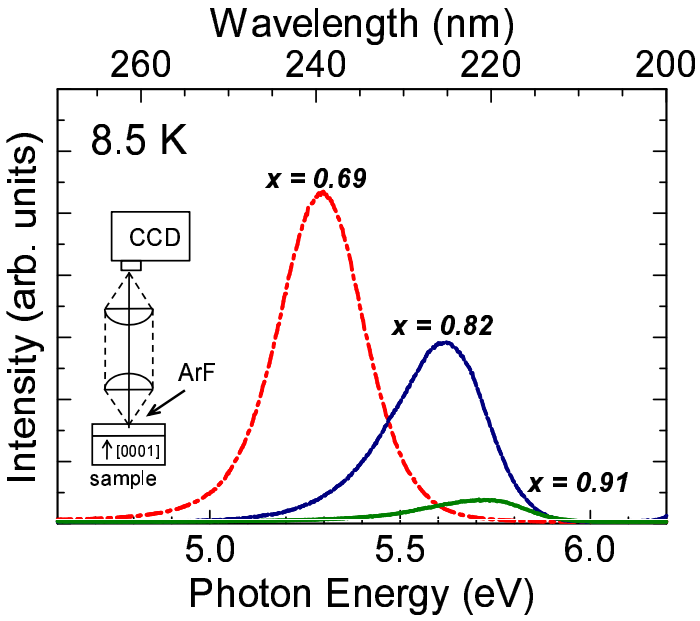

Figure 5.12: Confirmation of intense surface emission from samples measured from the edge as shown in Figure 5.6. As expected intense surface emission is observed up to $x \sim 0.82$ while on the other hand, the surface emission from $x \sim 0.91$ QWs shows weak surface emission. Inset shows the PL set-up used in this experiment.

5.5 Future Application

One of the most important consequences of this finding is that conventionally-grown AlGaN QW on c-plane can be used to fabricate surface-emitting lasers even at wavelengths as small as $\lambda \sim 225$ nm. This is in contrast to the conventional idea that for such short emission wavelength, the device must be fabricated on non-polar planes to achieve intense surface emission.

But with this new finding, UV emitters can be fabricated on the conventional c-plane and yet achieve an an intense surface emission down to $\lambda \sim$ 220 nm (see Table 5.3).

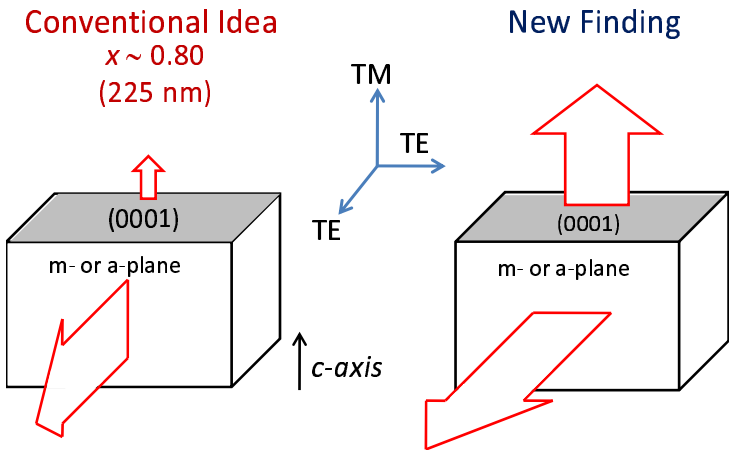

Figure 5.13: The consequence of intense surface emission at $x \sim 0.25$ ($\lambda \sim$ 220 nm). With such intense emission at short wavelength, surface emission is possible for c-plane-based UV emitters.

Table 5.3: Comparison of the surface emission between conventional idea with the new idea. Strong Surface emission is found possible for AlGaN up to $x \sim 0.80$. This opens for a new application for c-plane grown devices.

	Conventional Idea	New Finding
Conventional Edge-emitting laser structure	TM Mode	TE Mode
Surface Emitters (LED, VECSEL)	Weak Surface Emission	Strong Surface Emission

5.6 Summary

In summary, a unique optical polarization properties was observed in Al-rich ($x > 0.69$) $Al_xGa_{1-x}N$/AlN QWs. The emission with the polarization along ($\boldsymbol{E} \perp$ c) is observed up to x$\sim$0.82, particularly for thinner QWs. This large Al composition for the polarization switch from ($\boldsymbol{E} \parallel$ c) to ($\boldsymbol{E} \perp$ c) is attributed to the in-plane compressive strain and the quantum confinement due to narrow wells and/or internal electric fields. The results presented indicate that the appropriately designed c-oriented AlGaN QWs can produce a intense surface emission even in the DUV spectral range which is the key in reconciling good crystalline qualities and emission properties.

References

[1] M. Suzuki and T. Uenoyama, "First-Principles Calculations of Effective-Mass Parameters of AlN and GaN," *Phys. Rev. B,* **52**, 8132, (1995).

[2] S. H. Wei and A. Zunger, "Valence Band Splittings and Band Offsets of AlN, GaN, and InN," *Appl. Phys. Lett.,* **69**, 2719, (1996).

[3] J. Li, K. B. Nam, M. L. Nakarmi, J. Y. Lin, H. X. Jiang, P. Carrier, and S. H. Wei, "Band Structure and Fundamental Optical Transitions in Wurtize AlN," *Appl. Phys. Lett.,* **83**, 5163, (2003).

[4] E. Silveira, J. A. Freitas Jr., O. J. Glembocki, G. A. Slack, and L. J. Schowalter, "Excitonic Structure of Bulk AlN from Optical Reflectivity and Cathodoluminescence Measurements," *Phys. Rev. B,* **71**, 041201, (2005).

[5] Y. Taniyasu, M. Kasu, and T. Makimoto, "Radiation and Polarization Properties of Free-Exciton Emission from AlN (0001) Surface," *Appl. Phys. Lett.,* **90**, 261911, (2007).

[6] I. Vurgaftman and J. R. Meyer, "Band Parameters for Nitrogen-Containing Semiconductors," *J. Appl. Phys.,* **94**, 3675, (2003).

[7] R. Dingle, D. D. Sell, S. E. Stokowski, and M. Ilegems, "Absorption, Reflectance, and Luminescence of GaN Epitaxial Layers," *Phys. Rev. B,* **4**, 1211, (1971).

[8] M. Suzuki and T. Uenoyama, "Strain Effect on Electronic and Optical Properties of GaN/AlGaN Quantum-Well Lasers," *J. Appl. Phys.,* **80**, 6868, (1996).

[9] K. B. Nam, J. Li, L. Nakarmi, J. Y. Lin, and H. X. Jiang, "Unique Optical Properties of AlGaN Alloys and Related Ultraviolet Emitters," *Appl. Phys. Lett.,* **84**, 5264, (2004).

[10] A. A. Yamaguchi, "Valence Band Engineering for Remarkable Enhancement of Surface Emission in AlGaN Deep-Ultraviolet Light Emitting Diodes," *Phys. Stat. Sol. (c),* **6**, 2364, (2008).

[11] J. Shakya, K. Knabe, K. H. Kim, J. Li, J. Y. Lin, J. Y. and H. X. Jiang, "Polarization of III-Nitride Blue and Ultraviolet Light-Emitting Diodes," *Appl. Phys. Lett.,* **86**, 091107, (2005).

[12] H. Kawanishi, M. Senuma, and T. Nukui, "Anisotropic Polarization Characteristics of Lasing and Spontaneous Surface and Edge Emissions from Deep-Ultraviolet (λ $\sim$240 nm) AlGaN Multiple-Quantum-Well Lasers," *Appl. Phys. Lett.,* **89**, 041126, (2006).

[13] H. Kawanishi, M. Senuma, M. Yamamoto, E. Niikura, and T. Nukui, "Extremely Weak Surface Emission from (0001) c-plane AlGaN Multiple Quantum Well Structure in Deep-Ultraviolet Spectral Region," *Appl. Phys. Lett.,* **89**, 081121, (2006).

[14] S. L. Chuang and C. S. Chang, "$\mathbf{k}\cdot\mathbf{p}$ Method for Strained Wurtzite Semiconductors," *Phys. Rev. B,* **54**, 2491, (1996).

[15] F. Bernardini, V. Fiorentini, and D. Vanderbilt, "Spontaneous Polarization and Piezoelectric Constants in III-V Nitrides," *Phys. Rev. B,* **56**, R10024, (1997).

[16] S. H. Park and S. L. Chuang, "Spontaneous Polarization Effects in Wurtzite GaN/AlGaN Quantum Wells and Comparison With Experiment," *Appl. Phys. Lett.,* **76**, 1981, (2000).

[17] C. Y. Yeh, Z. W. Lu, S. Froyen, and A. Zunger, "Zinc-blende Wurtzite Polytypism in Semiconductors," *Phys. Rev. B,* **46**, 10086, (1992).

[18] M. Leroux, N. Grandjean, J. Massies, B. Gil, P. Lefebvre, and P. Bigenwald, "Barrier-width Dependence of Group-III Nitrides Quantum-Well Transition Energies," *Phys. Rev. B,* **60**, 1496, (1999).

[19] S. P. Lepkowski, H. Teisseyre, T. Suski, P. Perlin, N. Grandjean, and J. Massies, "Piezoelectric Field and its Influence on the Pressure Behavior of the Light Emission from GaN/AlGaN Strained Quantum Wells," *Appl. Phys. Lett.,* **79**, 1483, (2001).

Chapter 6

Conclusion

In this thesis, the growth and characterization of high-quality AlN and Al-rich ($x > 0.69$) $Al_xGa_{1-x}N$/AlN QWs fabricated by modified MEE were presented. The conclusion for each chapter is presented accordingly.

In chapter 1, the research history of III-V nitride semiconductors, its current status, and future trend were presented. Specifically, since the future research trend is moving toward smaller spectral emission range, the current status of AlN and AlGaN was discussed. AlN ans AlGaN are found interesting because of its unique optical properties.

Chapter 2 explained the growth and characterization of AlN epilayer grown by simultaneous source-supply, MEE, and modified MEE. The structural quality of ∼600-nm-thick AlN was compared among these three methods. To understand their differences in structural quality, the initial nucleation stage (AlN < 100 nm) was investigated. AFM images clearly demonstrated that the degree of Al-adatom migration between each method is different where the lowest migration degree happened for simultaneous source-supply while MEE has the most enhanced migration, and modified MEE has a migration degree in-between them. This degree of migration is characterized by the preferred or random nucleation and ridge height of nuclei. On the other hand, for thick (> 400 nm) AlN, the Al-adatom surface migration was lowest in simultaneous source-supply method and comparable between MEE and modified MEE. The growth rates were also determined for each method where simultaneous supply had 0.50 nm/s (= 2 ML) while MEE had 0.25 nm/cycle (1 ML). On the other hand, the growth rate of modified MEE was found to be the sum of other two methods (= 3 ML), which clearly demonstrated that no gas-phase pre-reaction occurred even for simultaneous supply. It was found out that the modified MEE was able to achieved the best-quality AlN epilayer as confirmed AFM and XRD measurements.

As a high-quality AlN was achieved by modified MEE, chapter 3 discussed the growth characteristics of this method. Particularly, the growth temperature and V/III ratio weighted heavily on the structural quality of the epilayer as measured by the XRD linewidths of both symmetric (0002) and asymmetric ($10\bar{1}2$) planes. Th structural quality was sensitive to growth temperature as a slight change (5 °C) degraded the epilayer quality. The V/III ratio also affected the epilayer where a decrease of V/III obtained a rough surface morphology while a V/III ratio beyond the optimum obtained an epilayer with nano-pits. Temperature-dependence PL was performed and the room-temperature to low-temperature PL ratio achieved as high as ∼15 %, suggesting the high-quality of the epilayer.

In chapter 4, the fabrication of Al-rich $Al_xGa_{1-x}N$/AlN MQWs was performed using the modified MEE method. The incorporation of Al (x = 0.69 - 1.0) in the well was controlled by decreasing the growth temperature from 1225 °C to 1080 °C. On the other hand, the well widths were also varied by increasing the number of cycles of (TMA + TMG)/NH_3 supply. The successful fabrication of QWs with different thicknesses and compositions were confirmed by XRD measurements and supported by x-ray rocking curve simulation. The optical characterization on QWs were performed and an intense emissions as low as 215 nm ($x \sim 0.91$) was achieved.

In chapter 5, the optical polarization anisotropy probed by PL measurements both in AlN and Al-rich $Al_xGa_{1-x}N$/AlN were performed. For AlN, the polarization degree, ρ, was ∼0.82 confirming the strong polarization with $\boldsymbol{E} \parallel$ c. On the other hand, since AlN has negative crystal splitting energy ($\Delta_{cr} = -217$ meV) in contrast to the positive value of GaN ($\Delta_{cr} = 11$ meV), polarization switch from $\boldsymbol{E} \parallel$ c to $\boldsymbol{E} \perp$ c at an Al composition of x ∼0.83. This is a first experimental evidence that surface emission is possible at this high Al content. This was possible due to quantum confinement coupled by strain and internal electric field effect caused by spontaneous and piezoelectric polarizations. Moreover, the well width dependence of the polarization properties was assessed using $Al_{0.82}Ga_{0.18}N$ QWs and it showed that thicker QW (> 3 nm) promotes $\boldsymbol{E} \parallel$ c polarization as a consequence of quantum confinement. This observation was interpreted using a simple model and the experimental result agreed very well with the calculation after considering the in-plane compressive strain and quantum confinement due to narrow wells and/or internal electric fields.

Acknowledgments

My interest in the study of optoelectronic materials started during my Master's course at Tohoku University. During this time, my research was into the deposition of thick Y_2O_3 and α-Al_2O_3 film as thermal barrier coatings using Laser Chemical Vapor Deposition (LCVD). My experiment involved YAG laser used to generate the emission to excite and generate a chemical reaction on the substrate, thus achieving a fast-deposition rate and superior quality films. One day, curiosity came to my mind about how the laser is generated. As I was reading a book and some journals regarding the benefit of employing a laser to the growth rate and quality of the film, I became more and more interested with how the laser is produced itself. Without going into the details, I decided to study the materials that generate the "lasers".

Thus, I came to study the optoelectronic properties of AlN mainly for ultraviolet applications. For my three years of study, I was able to learn a lot of new things with the help of my brilliant Professors, researchers, and my fellow students.

As I am nearing the end of this work, I am indebted to the following who have directly influenced me in so many ways, and their names are worth mentioning.

First, I would like to personally thank my Professor (Prof. Yoichi Kawakami) for giving me the chance to study in his laboratory. This has been a fulfillment of my dream and I am forever grateful for this. The assuring smile of my Professor has given me the courage to do my best. His competence in the optical processes has also encouraged me to study this topic more.

I would also like to thank my Associate Professor Mitsuru Funato for sharing his knowledge and being able to have valuable discussions regarding the direction of my research. Being directly under Professor Funato, I was able to learn a lot. His understanding and patience has always assured me to strive harder.

I would also like to thank our secretary, Miki Terai - for always being

there and cheering us up during the challenging times of our research.

I would also like to thank Research Associate Professor Koichi Okamoto for taking interest in AlN, hope we could do some collaborative work in the near future.

To Akio Kaneta, thank you also for the teaching me a lot about spectroscopy measurements. Truly, it made my research life easier. The fun moments, for lending hand, giving advices, thank you very much.

I would also like to thank my Labmates, past and present for creating an environment conducive for learning. To Su Lan and Keita Hayashi, for the friendship and camaraderie. To Hiroaki Kamon, for playing a pivotal role in doing DUV experiments in AlN. I have learned a lot from it and from there, I was able to do experiments on my own. For Kazunobu Kojima, for the friendship as well.

To the present bachelor students namely, Kyosuke Ito, Takao Oto, Akira Hashiya, Li Chen and Junichi Nishinaka, for sharing the laughter and fun. I would like to mention my AlN buddy - Takao Oto for exerting great efforts for our work on AlN. May you continue to find happiness in doing research with AlN. Truly, doing research with someone is more fun that doing it alone. And I was happy when you chose to be doing AlN.

To the 2nd year Master students namely, Daisuke Inoue for being my onsen and beach buddy - from the deepest of my heart thank you very much and I hope we could do it again someday somewhere. Too bad I will have no beach/onsen buddy anymore after you leave the Laboratory. Hope that we still continue the friendship. And to Katsuhito Nishimura for being always there when I needed your help. May you find happiness in your chosen career.

To the 1st year master students namely, Ryota Ishii, for valuable discussions regarding optical properties of AlN, to Tsuneaki Hashimoto for helping without hesitation, Takeshi Fujimoto for finding interest in the study of AlN, Keiji Watanabe for being approachable, and Mitsuru Watanabe for the being approachable and for the various help.

To fellow graduating Ph. D. student, Masaya Ueda, I thank you for so many things (this space is not actually enough). It was really my pleasure to have known you as a friend. Thank you for the help in everything - it made my life more easier. To Yoon Seok Kim and Eun Jeong Kang - I thank you for the friendship and I wish you all the best in your endeavors.

To Richard Bardoux for being always ready when I need you expertise and your friendship as well - I thank you very much.

To all the people who have made an impact in my life, in one way or

another, I also thank you.

To my family back in the Philippines, who serves as my inspiration and for being there always.

To my friends in Kyoto - truly you have filled the longings of my heart.

Lastly, to the Almighty God, for always giving me the courage to face the uncertainties in life.

List of Publications

List of Publications

1. Ryan G. Banal, Mitsuru Funato, and Yoichi Kawakami
"Optical Anisotropy in [0001]-oriented $Al_xGa_{1-x}N$/AlN quantum wells (x>0.69)," *Physical Review B, in press.*

2. Ryan G. Banal, Mitsuru Funato, and Yoichi Kawakami
"Growth Characteristics of AlN on Sapphire Substrates by Modified Migration Enhanced Epitaxy,"
Journal of Crystal Growth, (*available online 14 January 2009*).

3. Ryan G. Banal, Mitsuru Funato, and Yoichi Kawakami
"Surface Diffusion during Metalorganic Vapor Phase Epitaxy of AlN,"
Physica Status Solidi (C), **6** 599 (2009).

4. Ryan G. Banal, Mitsuru Funato, and Yoichi Kawakami
"Initial Nucleation of AlN Grown Directly on Sapphire Substrates by Metalorganic Vapor Phase Epitaxy,"
Applied Physics Letters, **92**, 241905 (2008).

Conferences Attended

International Conference

1. Ryan G. Banal, Mitsuru Funato and Yoichi Kawakami, "A New Growth Method of High-Quality AlN on Sapphire Substrates," International Symposium on Semiconductor Light Emitting Devices, April 27 - May 2, 2008, Phoenix, Arizona, USA (oral).

2. Ryan G. Banal, Mitsuru Funato and Yoichi Kawakami, "Structural Evolution of Directly-grown AlN on Sapphire Substrates by Regulated

Source-Supply Epitaxy," Second International Symposium on Growth of III-Nitrides, July 6 - 9, 2008, Izu, Japan (oral and poster).

Local Conference

1. Ryan G. Banal, Mitsuru Funato, and Yoichi Kawakami, "A New Growth Method of High-Quality AlN on Sapphire Substrates," 55^{th} Spring Meeting: Applied Physics Conference, March 27 - 30, 2008, Nihon Daigaku, Japan (oral).

2. Ryan G. Banal, Mitsuru Funato, and Yoichi Kawakami, "Deep-Ultraviolet Emission of AlGaN/AlN MQWs grown by Modified Migration Enhanced Epitaxy," 69^{th} Autumn Meeting: Applied Physics Conference, September 2 - 5, 2008, Chubu Daigaku, Japan (oral).

3. Ryan G. Banal, Mitsuru Funato, and Yoichi Kawakami, "Structural Evolution of AlN Grown Directly on Sapphire Substrates by Metalorganic Vapor Phase Epitaxy," 27^{th} Electronic Materials Symposium, July 7 - 9, 2008, LaForet Shujenzi, Izu, Japan.

4. Ryan G. Banal, Mitsuru Funato, and Yoichi Kawakami, "Intense Surface Emission at 222 nm from (0001) $Al_{0.82}Ga_{0.18}N$/AlN Quantum Wells," 56^{th} Spring Meeting: Applied Physics Conference, March 27 - April 2, 2009, Tsukuba Daigaku, Japan (oral and poster).

Related Conference

1. Ryan G. Banal, Mitsuru Funato, and Yoichi Kawakami, "High Quality AlN Grown on Sapphire Substrates by Regulated Source Supply Epitaxy," The Society of Materials Science, Semiconductor Electronics Research Symposium, March 6, 2008, Kyoto University, Katsura Campus, Kyoto, Japan (oral).

List of Figures

List of Tables